

7-13-2009

Magmatic Evolution of the Eocene Volcanic Rocks of the Bijgerd Kuh E Kharchin Area, Uromieh-Dokhtar Zone, Iran

Armita Davarpanah

Follow this and additional works at: https://scholarworks.gsu.edu/geosciences_theses

 Part of the [Geography Commons](#), and the [Geology Commons](#)

Recommended Citation

Davarpanah, Armita, "Magmatic Evolution of the Eocene Volcanic Rocks of the Bijgerd Kuh E Kharchin Area, Uromieh-Dokhtar Zone, Iran." Thesis, Georgia State University, 2009.
https://scholarworks.gsu.edu/geosciences_theses/19

This Thesis is brought to you for free and open access by the Department of Geosciences at ScholarWorks @ Georgia State University. It has been accepted for inclusion in Geosciences Theses by an authorized administrator of ScholarWorks @ Georgia State University. For more information, please contact scholarworks@gsu.edu.

MAGMATIC EVOLUTION OF THE EOCENE VOLCANIC ROCKS OF THE BIJGERD
KUH E KHARCHIN AREA, UROMIEH-DOKHTAR ZONE, IRAN

by

ARMITA DAVARPANA

Under the Direction of Hassan A. Babaie

ABSTRACT

Composition and texture of the Middle and Late Eocene volcanic, volcanoclastic, and volcanic-sedimentary rocks in the Bijgerd-Kuh e Kharchin area, in the Uromieh-Dokhtar zone northwest of Saveh, Iran, suggest the complexity of the magmatic system that involved multiple eruptions from one or more sources. Hydrated volcanic fragments in hyaloclastic rocks, and the presence of a sequence of shallow and intermediate-depth marine microfossils, suggest that the Middle Eocene units were erupted in a marine basin. The bimodal volcanism of the Late Eocene is distinguished by the presence of four alternating sequences of hyaloclastite lava and ignimbrite. The REE patterns show spatial homogeneity and temporal heterogeneity in the composition of all the Late Eocene sequences, suggesting origination of magma from varying sources that erupted at different times. The trace element distributions of the hyaloclastites and

ignimbrites are compatible with those evolved through fractional crystallization of the lower and upper continental crust, respectively.

INDEX WORDS: Bijgerd-Kuh e Kharchin area, Saveh, Iran, Uromieh-Dokhtar volcanic-plutonic zone, Eocene volcanism, Magma mixing/mingling, Partial melting, Fractional crystallization

MAGMATIC EVOLUTION OF THE EOCENE VOLCANIC ROCKS OF THE BIJGERD
KUH E KHARCHIN AREA, UROMIEH-DOKHTAR ZONE, IRAN

by

ARMITA DAVARPANA

A Thesis Submitted in Partial Fulfillment of the Requirements for the Degree of

Master of Science

in the College of Arts and Sciences

Georgia State University

2009

Copyright by
Armita Davarpanah
2009

MAGMATIC EVOLUTION OF THE EOCENE VOLCANIC ROCKS OF THE BIJGERD
KUH E KHARCHIN AREA, UROMIEH-DOKHTAR ZONE, IRAN

by

ARMITA DAVARPANA

Committee Chair: Hassan A. Babaie

Committee: Eirik J. Krogstad
Timothy E. La Tour
Morteza Khalatbari-Jafari

Electronic Version Approved:

Office of Graduate Studies
College of Arts and Sciences
Georgia State University
August 2009

ACKNOWLEDGEMENTS

I would like to express my profound gratitude to my supervisor, Dr. Hassan Babaie, whose support, expertise, consideration, and patience, contributed extensively to my graduate experience. Dr. Babaie, you provided me inspiration, direction, and technical support and became more of a mentor to me than a professor. I would not have considered a graduate career without your motivation and encouragement. I doubt that I will ever be able to fully convey my appreciation, but I owe you my eternal gratitude.

My sincere thanks go to the following members of my committee. Dr. Morteza Khalatbari-Jafari, thank you for presenting me the topic of this thesis, accompanying me in the field, and providing me with constructive criticism, which led to significant improvement of this thesis. Dr. Eirik Krogstad, I am thankful to you for patiently teaching me the basics of the ICP-MS analytical method, and for your inputs, feedback, and critical discussions. Dr. Timothy La Tour, I never forget you for bringing me into the graduate program at Georgia State University and opening a whole new world of geology to me, teaching me the XRF lab, and supporting my microprobe analysis. Thank you very much for all these supports. I thank Dr. Dan Deocampo for fixing the XRF laboratory, and expediting my laboratory work.

I am grateful to the Geological Survey of Iran for providing me facilities to conduct my field work. I would like to acknowledge all the cooperation I have received for the completion of my thesis project at Georgia State University Geology Department of Geosciences, University of Georgia (microprobe), and SGS Mineral Service lab (trace element analysis).

I would like to thank all my good friends (e.g. Dr. Katayoun Mobasher and Emily Smith) for their kindness during my graduate career. Thank you Katty, for introducing me to Dr. Khalatbari, encouraging me to pursue my graduate work, and accompanying me during my Microprobe work at UGA. Thank you Emily for working with me in the ICPMS lab.

I take this opportunity to express my deepest sense of gratitude to my families. I thank my husband for realizing the significance of this milestone in my life. Farhad, thank you for your understanding and patience during my studies. Dear mom, dad, Anita, and Tina, thank you so much for your unconditional and continued love, support, and encouragement that you have provided me through my entire life and especially during this endeavor.

TABLE OF CONTENTS

ACKNOWLEDGEMENTS	iv
LIST OF TABLES	ix
LIST OF FIGURES	x
CHAPTER	
1. INTRODUCTION	1
Major Geological Provinces of Iran	3
General Geology of the Area NW of Saveh	5
Study Area	7
Geological and Tectonic Setting	10
Fold and Fault	11
2. METHODOLOGY	13
Sample Preparation	14
Petrography	15
Electron Microprobe Analysis (EMPA)	16
Trace Element Analytical Methods	18
Determination of the REE	20
Major Element Analysis	25
3. RESULTS	30
Field Work	30
E ^{gt} Unit	34
E ^v Unit	34
Upper Eocene Volcanic Units South of the Bijgerd Fault	37

E ^h Unit	37
E ^{ig} Unit	38
Upper Eocene Volcanic Units in the Bijgerd-Kuh e Kharchin Section	38
E ^{ab} Unit	38
E ^{mb1} Unit	39
E ^{ig1a} and E ^{ig1b} Units	41
E ^c Unit	44
E ^{mb2} Unit	44
E ^{st1} and E ^{st2} Units	45
E ^a Unit	48
E ^{ig2} Unit	48
E ^{hy} Unit	49
E ^{ig3} Unit	50
E ^b Unit	51
E ^{mb3} Unit	51
E ^{ig4} Unit	53
OM ^{lm1}	53
Pl-Q ^C Unit	54
Q ^t Unit	55
Petrography	55
The Middle Eocene Volcanic Rocks (Samples KM 42, 43, 44)	55
Late Eocene Volcanic-Volcaniclastic Rocks	57

Sequence 1 (samples KM 30, 45, 48, 46, 31, 47, 32)	57
Sequence 2 (Samples KM 49, 50, 33, 34)	60
Sequence 3 (Samples KM 35, 36, 51, 37)	62
Sequence 4 (Samples KM 38, 41)	63
Microprobe Analysis	64
Major Element Analysis	65
Trace Elements	78
4. DISCUSSION	104
Field Relationship	104
Petrography	109
Major Element Analysis	113
Trace Element Analysis	118
5. CONCLUSIONS	129
REFERENCES	133

LIST OF TABLES

Table 2.1.	GPS coordinates of the studied volcanic rock samples in the Bijgerd-Kharchin area	15
Table 2.2.	The detection level of the ICM90A method of SGS used for the trace element analysis in this study	20
Table 3.1.	Microprobe data of the four hyaloclastic rocks in the study area, obtained in the University of Georgia (UGA)	75
Table 3.2.	Major element concentrations (wt%) of volcanic rocks in the study area, obtained in the Georgia State University's XRF laboratory	76
Table 3.3.	Characteristics of the rare earth elements (REE)	80
Table 3.4.	Rare earth element concentrations (ppm) obtained through isotope dilution mass spectrometry at GSU	99
Table 3.5.	Trace element concentrations of the volcanic rocks in the study area, obtained at SGS (ICM90A Method)	100

LIST OF FIGURES

Figure 1.1.	Geological map of Iran	5
Figure 1.2a.	Legend for the geological map of the Bijgerd-Kharchin study area	8
Figure 1.2b.	Geological map of the study area, showing the location of the studied samples	9
Figure 2.1.	Vacuum turbo carbon coater	17
Figure 2.2.	Slide holders	17
Figure 2.3.	The EPMA lab at UGA	17
Figure 2.4.	Pouring the melted sample into the beaker	22
Figure 2.5.	Primary (exchange) columns filled with resin (AG 50W-X8)	23
Figure 2.6.	Secondary (exchange) columns or α -HIBA	24
Figure 2.7.	The weighting of the rock sample and flux into a digital scale	26
Figure 2.8.	The platinum crucible containing the sample and flux in the furnace	27
Figure 2.9.	Stirring up the crucible was over the hot triangle	28
Figure 2.10.	Pouring the melt into the hot mold	28
Figure 2.11.	The desiccating cabinet containing the glass disks	29
Figure 2.12.	Rigaku 3270 X-ray fluorescence spectrometer at Georgia State University	29
Figure 3.1.	General view of the Mid-Late Eocene volcanic rocks of the study area	30
Figure 3.2a.	Legend for the geological map of the Bijgerd-Kharchin study area	31
Figure 3.2b.	Geologic map and cross sections of the Bijgerd-Kharchin study area	32
Figure 3.2c.	Volcano-stratigraphic column of the Bijgerd-Kharchin area	33

Figure 3.3.	A general view of the Middle Eocene volcanic rocks of the E ^v unit	36
Figure 3.4.	A sequence of hyaloclastic breccia and tuff at the base	36
Figure 3.5a.	Carbonate minerals in the hyaloclastite	39
Figure 3.5b.	Iron oxide minerals in the hyaloclastite of the E ^{ab} unit	39
Figure 3.6.	Conglomerate of the E ^{mb1} unit	40
Figure 3.7.	The crenulated contact on the mafic-intermediate clast edges (E ^{mb1} unit)	40
Figure 3.8.	A general view of the Late Eocene volcanic rocks (E ^{ab} and E ^{ig1} units)	42
Figure 3.9.	E ^{ig1} unit includes ignimbrite-tuff, ignimbrite-breccia, and ignimbrite fiamme	42
Figure 3.10.	E ^{ig1} unit: Conglomerate, and sandstone.	43
Figure 3.11.	Felsic pseudo fiamme field with intermediate lava (on the left), flaky shape welded ignimbrite-tuff (on the right), E ^{ig1} unit	43
Figure 3.12.	A view of E ^{ig1b} , E ^c , and E ^{mb2} units	45
Figure 3.13.	A field view of the succession of the E ^{ig1} , E st , and E ^{ig2} units	46
Figure 3.14a.	A sequence of siltstone, tuffite, and green tuff in the E st unit	47
Figure 3.14b.	A close view of siltstone(bottom) and tuffite (top) in the E st unit	47
Figure 3.15.	A view of rhyolitic ash tuff in the E st unit	47
Figure 3.16.	Mafic-intermediate enclaves in the ignimbrite	48
Figure 3.17.	Hyaloclastic breccia located at higher stratigraphic levels in the E ^{hy} unit	50
Figure 3.18.	A general view of E ^{ig3} and E ^{hy} units	50
Figure 3.19.	A hand specimen of the trachyandesite lava of the E ^{ig3} unit	51
Figure 3.20.	Red, crystal-lithic tuff	52
Figure 3.21.	Unwelded, mingled breccia with angular fragments of welded ignimbrite at the base of the E ^{mb3} unit	52

Figure 3.22.	E ^{ig4} unit: Mingled ignimbrite, fiamme, and pseudo fiamme ignimbrite	53
Figure 3.23.	Razeghan anticline and Kuh e Kharchin covered by Qom limestone	54
Figure 3.24.	Photomicrograph showing twinned and zoned plagioclase (KM 30)	59
Figure 3.25.	Vermicular pseudo-fiammes, filled with quartzo-feldspathic minerals	59
Figure 3.26.	Photomicrographs showing saussuritization in the altered plagioclases in sample KM 49 of the second sequence	61
Figure 3.27.	Photomicrograph showing zoning and saussuritization in plagioclase KM 50	61
Figure 3.28.	Sieve texture and zoning in plagioclase in samples KM 50 (left) and KM 49 (right)	62
Figure 3.29.	Quartz inclusions (left) and iddingsite minerals in olivine (KM 38)	63
Figure 3.30.	Microprobe images showing different compositional zoning in the core of the plagioclase (KM 38)	64
Figure 3.31.	Total Alkali-Silica diagram modified from Le Bas (1986) and La Martin et al., (1989)	67
Figure 3.32.	Sub-alkalic subdivisions based on potassium composition	67
Figure 3.33.	Loss on ignition (LOI %) vs. SiO ₂ for all volcanic rocks	69
Figure 3.34.	Major elements vs. SiO ₂ (wt %)	71
Figure 3.35.	Major elements vs. MgO (wt %)	73
Figure 3.36.	Major elements vs. Mg number	74
Figure 3.37.	The REE patterns of the collected rock samples of the Middle and Late Eocene volcanic and volcanoclastic rocks in the study area	82
Figure 3.38.	The REE patterns for some selected hyaloclastic rock samples in the Bijgerd-Kuh e Kharchin area	84
Figure 3.39.	The REE patterns for the volcanoclastic (felsic) rocks in the study area	85
Figure 3.40.	The REE patterns for the Middle Eocene volcanic rocks unit (E ^v)	86

Figure 3.41.	The REE patterns for the first Late Eocene sequence (units E ^{ab} and E ^{ig1})	87
Figure 3.42.	The REE patterns for the second sequence (units E ^a and E ^{ig2})	88
Figure 3.43.	The REE patterns for the third Late Eocene sequence (units E ^{hy} and E ^{ig3}) of the Bijgerd-Kuh e Kharchin area	89
Figure 3.44.	The REE patterns for the fourth sequence (units E ^b and E ^{ig4})	90
Figure 3.45.	Comparisons of REE patterns of collected samples in each sequence	92
Figure 3.46.	TiO ₂ (wt%) plotted vs. Zr (ppm)	93
Figure 3.47.	Zr (ppm) plotted vs. SiO ₂ (wt%)	94
Figure 3.48.	Zr plotted against La, Nb, and Ce	95
Figure 3.49.	Ce and Nd concentrations plotted against La	96
Figure 3.50.	U concentrations plotted against Th	97
Figure 3.51.	La concentrations plotted against Yb for each Upper Eocene sequence and for all rock samples	98

CHAPTER 1

INTRODUCTION

This investigation is based on geologic, petrographic, and geochemical studies of the Middle and Late Eocene volcanic, volcanic-sedimentary, and volcanoclastic rocks in the Bijgerd-Kuh e Kharchin area, NW of Saveh, which is a part of the Uromieh-Dokhtar volcanic-plutonic zone of Iran (Figure 1.1).

The NW-SE oriented Urumieh-Dokhtar zone (UDZ), also known as the Sahand-Bazman volcanic belt, is a ~2000 km long and 50-200 km wide zone of Tertiary volcanic rocks, which extends from Uromieh in NW Iran to Pakistan's Baluchistan (Schroder, 1964). Magmatic events in this zone started in Late Paleocene and peaked during Late Eocene (Berberian and King, 1981).

Two competing hypotheses attribute the magmatic activities in the UDZ either to the subduction of the Tethyan oceanic lithosphere under the Iranian micro-plate, which occurred due to the convergence of the Arabian and Central Iranian plates (Forster et al., 1972; Takin, 1972; Dewey et al., 1973; Sengor et al., 1993), or melting of the sialic crust during a continental rifting, perhaps in a backarc basin (Kazmin et al, 1986). Most hypotheses proposed for volcanism in the Uromieh-Dokhtar zone cannot satisfactorily explain the nature of the magmatic processes that led to the Eocene volcanism, and the tectonic setting where it occurred.

Paleogeographic and tectonic reconstructions, using U-Pb and $^{40}\text{Ar}/^{39}\text{Ar}$ isotope, suggest that shallow marine to continental volcanism within the Uromieh-Dokhtar zone was generated by an Eocene subduction-related pulse which was not related to the subduction rate (Verdel, 2008).

However, Amidi et al., (1984) and Amidi and Michel (1985) suggest that the Uromieh-Dokhtar zone was a linear rift basin, unrelated to subduction. The Neotethyan oceanic lithosphere started to subduct under Iranian subplate (part of the Euroasian plate) about Late Triassic, and continued through the Late Oligocene (Barbarian, 1988).

The geochronological data, however, reveal that the extension of the volcanic arc within the Uromieh-Dokhtar zone occurred over a period of ~17 My, which is only a small part of the long period of subduction (McQuarrie et al., 2003) (since Late Triassic). The steep angle of the subducting Arabian lithospheric plate may have led to slab rollback in the mantle (Verdel, 2008). During this process the upper (Iranian) plate was stretched and thinned out, leading to backarc spreading. The rollback and related extension occurred when the subduction rate was more than the convergence rate (Schellart, 2005).

The Eocene crustal thinning, generated by extension, which followed the slab rollback, could have produced decompression melting of the sub-arc mantle (Verdel, 2008), or supported magma generation from the subducting plate, which was enhanced by slab fluids. The upwelling magma plume probably ascended through the thin rift, and cut and rejuvenated the overriding thinned upper plate (Iranian) lithosphere.

The main objectives of this investigation are as follows: (i) Construct a field-based, representative geological map, cross sections, and stratigraphic column of the Bijgerd-Kuh e Kharchin. (ii) Characterize field observations to assist in deciphering the nature of the magmatic processes. (iii) Conduct detailed petrographic analysis of the mineralogy and texture of the volcanic and volcanoclastic rocks and correlate the information with geochemical data to investigate magmatic processes and subsequent alteration. (iv) Apply microprobe analysis, especially of the intermediate composition lava, to determine the compositional variation in the

zonings of phenocrysts such as plagioclase, and their generations and variation over time. (v) Conduct geochemical analyses to determine the major and trace element compositions (including the rare earth, REE) of the volcanic and volcanoclastic rocks, investigate their distribution in space and time, and determine petrological patterns that may help identify the magmatic processes that formed these rocks. These will be done to reveal the magmatic evolution of the study area, and understand the petrogenetic significance of the data.

These detailed and targeted analyses intend to address the following questions: (i) What were the roles of magmatic processes such as differentiation, crystal fractionation, and partial melting in the evolution of volcanic rocks? (ii) What were the sources for the magmas? (iii) Is there any evidence of elemental contributions from the continental crust?

This study is significant because: (i) the geochemical analyses conducted in this project will provide significant clues for the magmatic evolution of the Uromieh-Dokhtar volcanic zone (UDZ), (ii) it will define the Bijgerd-Kuh e Kharchin area as a distinctive representative of the UDZ, and (iii) it will produce a comprehensive set of useful data which can be used to explain the Tertiary volcanic processes in other parts of the UDZ.

Major Geological Provinces of Iran

The Iranian micro-plate is part of the Eurasian plate which includes most of Europe and Asia, except the Indian subcontinent and the Arabian Peninsula, and part of Siberia (http://en.wikipedia.org/wiki/Eurasian_Plate).

The Iranian micro-plate includes several major tectonic provinces which have been developing since the Proterozoic (e.g., Aghanabati, 2006).

The long tectonic and geodynamic evolution of Iran involves formation of geological features such as continental rift, paleo-subduction zone (represented by ophiolites), and collision zone, which are associated with regional zones of volcanic/intrusive, metamorphic, and sedimentary assemblages (e.g. Berberian and King, 1981; Vaziri, 1998). In a traverse from southwest to northeast, the geology of Iran includes the following tectonic zones (Stöcklin and Setudenia, 1972) (Figure 1.1):

1. The Zagros fold-and-thrust belt is representative of a folded and faulted part of a Paleozoic platform, which exhibits a period of no sedimentation from Silurian to Permian. This zone includes sediments that represent a shallow marine sedimentary basin that deposited detrital, carbonate, and locally shale and evaporates from Permian to Late Triassic (e.g., Sepehr and Cosgrove, 2005; Babaie et al., 2001).

2. The Sanandaj-Sirjan zone is defined by extensive exposures of Paleozoic and metamorphic and magmatic rocks, and widespread evidence of Mesozoic magmatism (Eftekharnjad, 1980).

3. The Central Iran zone developed through several Triassic-Jurassic, Early Cretaceous, and Early and Late Cenozoic Alpine orogenic events (Stocklin, 1972).

4. The Uromieh-Dokhtar volcanic-plutonic arc (Sahand-Bazman belt) is characterized by the Late Paleocene and Eocene volcanism (Emami, 1981).

5. The Lut Block represents the old, stable platform, overlain by thick Mesozoic sediments and Eocene volcanic rocks (Aghanabati, 2006).

6. The Alborz and Kopeh Dagh mountain ranges represent the Late Alpine orogenic events with phases of Eocene volcanic and volcanoclastic activities (Wensink, 1980).

7. The Eastern Iran and Makran zones defined by ophiolites developed between Late Jurassic and Late Cretaceous (Shahabpour, 2007).

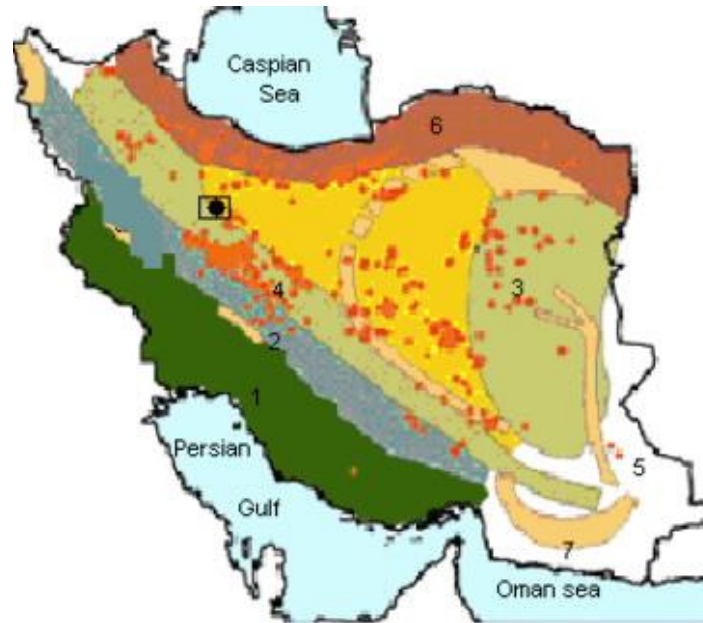



Figure 1.1. Geological map of Iran. Modified from the National Geosciences Database of Iran; (<http://www.ngdir.ir/>) showing major tectonic zones: 1. Zagros fold-and-thrust belt, 2. Sanandaj-Sirjan, 3. Central Iran, 4. Uromieh-Dokhtar volcanic-plutonic arc (Sahand-Bazman belt), 5. Lut Block, 6. Alborz and Kopeh Dagh, 7. The Eastern Iran and Makran, The location of the study area is given by . See text for explanation.

General Geology of the Area NW of Saveh

The study area, northwest of Saveh (Figure 1.1), is located where the Uromieh-Dokhtar zone is considerably narrowed, compared to its extent in central Iran, and aligned parallel to the trend of the Koshke Nosrat and Avaj faults east and west of Saveh, respectively.

The region northwest of Saveh is morphologically divided into three different areas: (i) The northern area of the region, manifested by plains and rolling (hummocky) hills of Pliocene

and Quaternary sediments. (ii) The central area, studied in this thesis research project, encompasses high mountain ranges, and is dominated by successions of Eocene volcanoclastic, volcanic-sedimentary, and Oligo-Miocene sedimentary rocks. The Encheh Ghareh Mountain, west of Bijgerd, with an elevation of approximately 2989 meters, is the highest peak in this region, and is covered by Upper Eocene volcanic rocks. (iii) The southern area is represented by Oligo-Miocene, and locally Cretaceous, sedimentary rocks, and Eocene volcanic-sedimentary rocks (Saveh 1:250,000 Quadrangle, Amidi et al., 1984).

According to Caillet et al. (1972) the region northwest of Saveh is characterized by exposures of Eocene rocks, although older Upper Triassic, Lower Jurassic, and Cretaceous succession is locally exposed in some parts of this region.

NW of Saveh, the oldest NW-SE oriented unit consists of Hamedan slate (Bolurchi, 1979) and phyllite, which extends sporadically to the area north of Saveh (on the Saveh-Nobaran-Hamedan road) parallel to the main Kooshkak fault. Although the metamorphic rocks have a tectonized contact with the Eocene volcanic rocks, they are, in places, covered nonconformably by the volcanic rocks (Amidi et al, 1984).

According to the Saveh 1:250,000 Quadrangle Map (Amidi et al., in 1984) the metamorphic rocks are the eastern extension of the Sanandaj-Sirjan zone, and have a tectonic contact with the Eocene volcanic rocks of the Uromieh-Dokhtar zone. Although the basal contact of the slate-phyllite unit is tectonized and not well-exposed, the unit is thrust, in the Louin and Ghermezin villages, over Eocene volcanic and Oligo-Miocene sedimentary rocks.

In other areas, northwest of Saveh, Eocene volcanic rocks nonconformably overlie the metamorphic unit. Attempts to date the brown dolomite interlayers, between these metamorphic rocks, have not led to any conclusive paleontological age.

However, Bolurchi (1979) discovered some Early Triassic and Late Jurassic *Heneilites Ammonite* in the slate units of his study area, which is equivalent to the slate-phyllite unit of NW of Saveh. Therefore, the age of the oldest unit northwest of Saveh can be inferred to be Late Triassic-Late Jurassic (Bolurchi, 1979). Moreover, the presence of the Upper Cretaceous Orbitolina limestone, which lies conformably on the slate, ascribes the metamorphic process that formed the slate to the latest Late Cimmerian orogenic phase (Khalatbari et al., 2000).

Cretaceous, mostly sedimentary rocks are mainly exposed northwest of Nobaran located in NW of Saveh area, where Khalatbari et al. (2000) have described several Cretaceous units in the Nobaran 1:100,000 Quadrangle Map. Aptian-Cenomanian and Turonian-Senonian ages are determined from the fossils in the Cretaceous biomicrite and pelites (Khalatbari et al., 2000).

Porphyritic andesite overlies the Cenomanian orbitolina-bearing biomicrite north of Nobaran, suggesting a maximum age of Late Cretaceous for the lava.

Locally, a 120-150 m thick sequence of siltstone, sandstone, and calcareous tuff is also assigned a Late Cretaceous age in the Nobaran 1:100,000 Quadrangle by Khalatbari et al., (2000).

Study Area

The study area, Bijgerd- Khuh e Kharchin, is located where the UDZ splits, northwest of Saveh, Iran, into two northern and southern slivers. The southern sliver, henceforth referred to as the Bijgerd-Kharchin area, is located between 35° 13', 50" N and 35° 19', 30" N latitudes, and 49° 53' E and 50° 00' E longitudes (Nobaran 1:100,000 Quadrangle) (Figures 2a-2b).

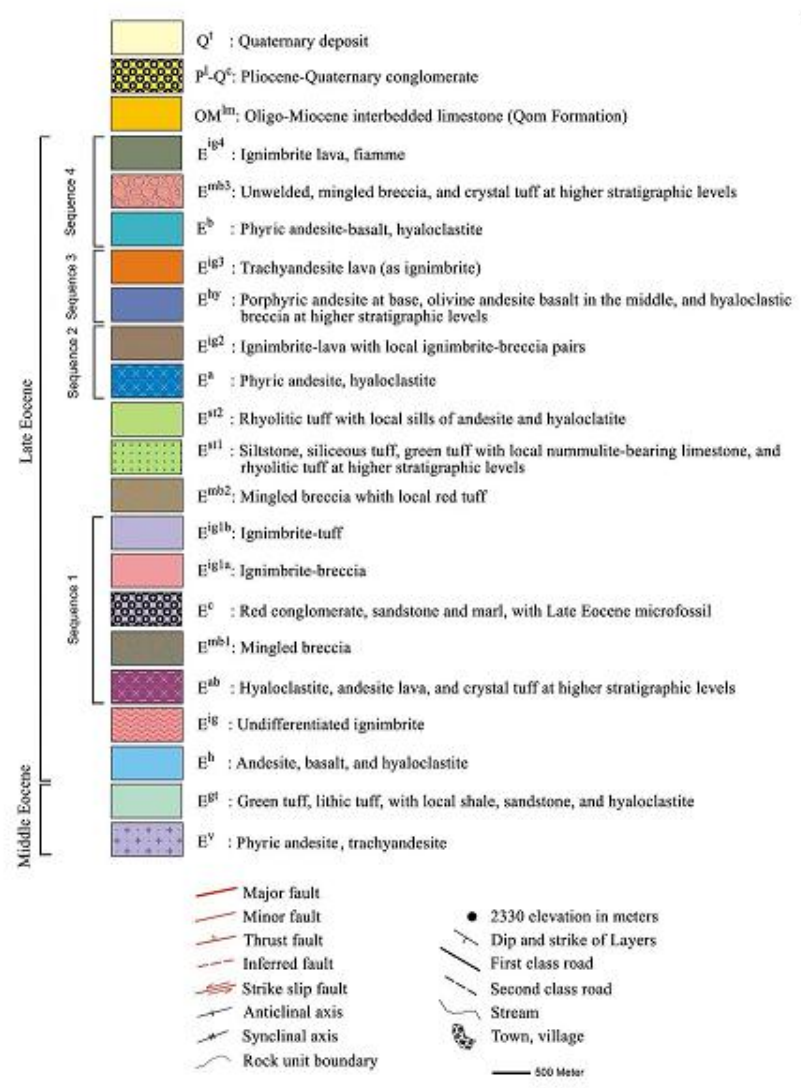


Figure 1.2a. Legend for the geological map of the Bijgerd-Kharchin study area.

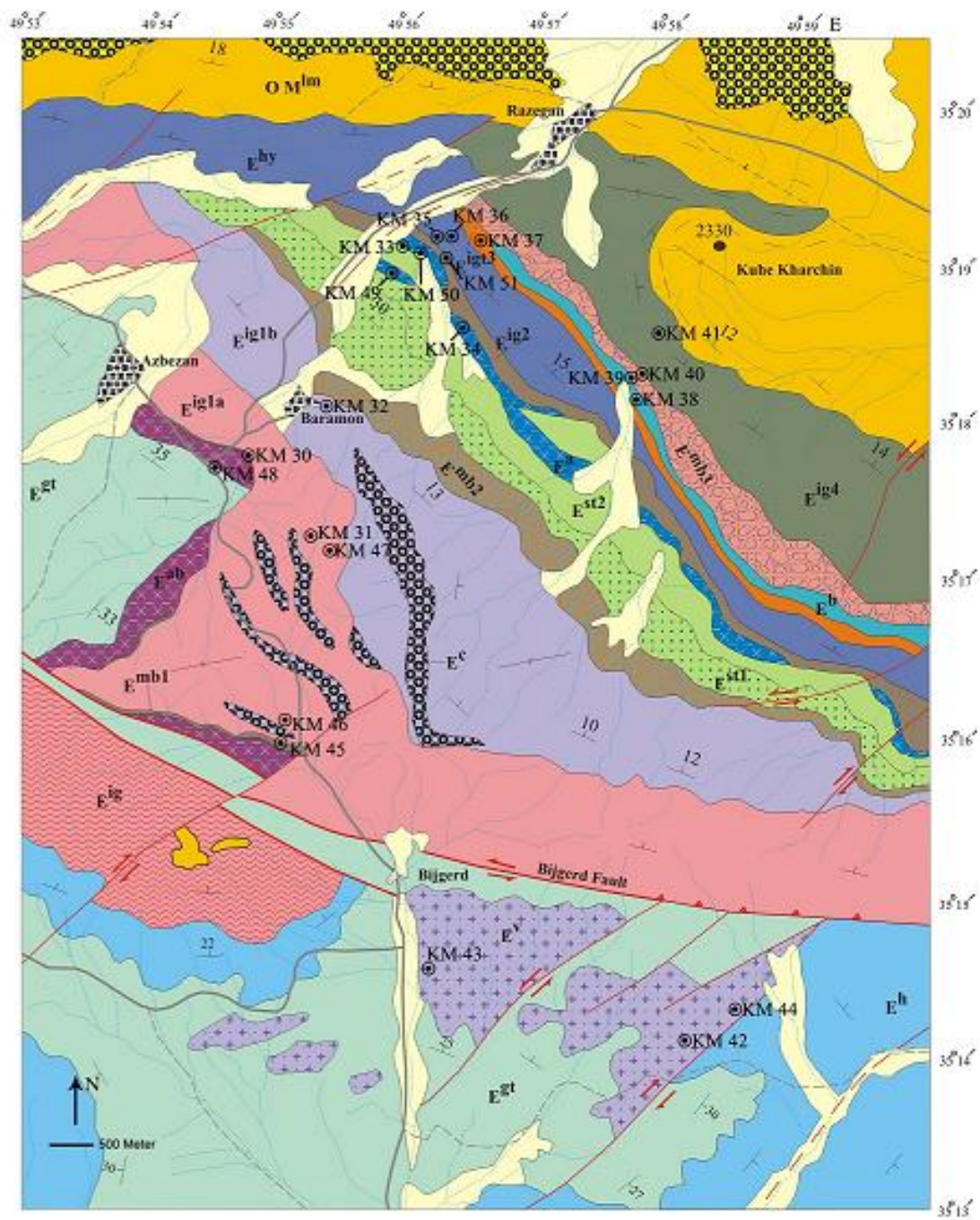


Figure 1.2b. Geological map of the study area, showing the location of the studied samples.

Geological and Tectonic Setting

Field and petrological investigations suggest a change in the nature of volcanic eruption and deposition of volcanic-sedimentary rocks during Eocene in the Uromieh-Dokhtar zone. For example, in some places of the UDZ acidic volcanic rocks and ignimbrites are more extensive than basic and intermediate lava. In places, basic and intermediate lava cooled either on shallow marine sediment or non-marine wet sediments, forming hyaloclastites.

Eruption of lava, especially acidic ones, brought glass shard and lithic fragments in contact with the sea water, growing green minerals such as chlorite and epidote, and forming green tuff which is so common in the Uromieh-Dokhtar zone. The presence of a sequence of shallow and intermediate depth marine sedimentary facies may suggest subsidence during Eocene.

The Bijgerd-Kharchin area exposes Middle and Late Eocene tuffaceous sandstone, lava, and volcanoclastic rocks. The Middle Eocene volcanic rocks have an intermediate composition, and include green tuff, tuffaceous sandstone, sandy tuff, and shale. The shale contains lenses of Nummulite-bearing limestone which gives a Lutetian age.

The Middle Eocene volcanic and volcanic-sedimentary rocks have been divided into two units (Figures 1.2 a, 3.2): E^{gt} - green and lithic tuff, with local shale, sandstone, and hyaloclastite, and E^v - phyric andesite, trachyandesite with basaltic and andesitic-basaltic compositions.

The Late Eocene succession is characterized by the presence of four alternating sequences (layers) of intermediate lava and felsic ignimbrite; the latter is designated as E^{ig} (Figures 1.2a, b, 3.2).

The Late Eocene volcanic rocks include hyaloclastic lava with a general andesitic, trachyandesitic, and basaltic compositions, which alternate with four levels of ignimbrite.

The ignimbrites have a rhyolitic composition, and include ignimbrite-breccia, ignimbrite-tuff, and ignimbrite-lava pairs. A characteristic feature of these ignimbrites is the presence of intercalated red conglomerate and some red sandstone and marl.

The four upper Eocene ignimbrites and associated rocks constitute four sequences of rocks which are designated on the map (Figures 1.2a, b) as sequence 1: E^{ab} , E^{mbr1} , E^{ig1a} , E^{ig1b} , E^{mbr2} , sequence 2: E^a , E^{st1} , E^{st2} , E^{ig2} , sequence 3: E^{hy} , E^{ig3} , and sequence 4: E^b , E^{mbr3} , and E^{ig4} . Various potential indications of magma mixing and mingling in all horizons, and existence of hybrid breccia with oxidized acidic, rhyolitic, and basic-intermediate clasts in at least three levels make the study of the volcanic rocks in this area significant for understanding the magmatic processes.

Fold and Fault

It is impossible to discuss the structural features of the Bijgerd-Kuh e Kharchin area without considering the structural features of NW of Saveh. As mentioned before, the Hamedan phyllite and slate, attributed to the Sanandaj-Sirjan zone, are tectonically juxtaposed with the Eocene volcanic rocks south of the Bijgerd-Kuh e Kharchin area.

Based on paleontological determinations during compilation of the 1:100,000 Kabotar Ahang Quadrangle map (Bolurchi, 1979) and study of *Ammonite* in the slate units of northwest of Saveh (Bolurchi, 1979, doctoral dissertation), the age of the slate and phyllite is assigned to a Late Triassic-Early Jurassic deformation which folded and uplifted them probably during the Late Cimmerian (?) orogeny.

Northwest of Saveh, transgression, following a period of erosion, led to the deposition of orbitolina-bearing limestone of Early Cretaceous (Aptian) age.

The Laramide orogeny, at the end of the Cretaceous, folded the older rocks, and later led to the formation of the Eocene volcanic rocks.

The Pyrenean orogenic phase at the end of Eocene led to the uplift of the area, and later, to the unconformable deposition of the Oligo-Miocene sedimentary rocks (Qom limestone) on top of the Eocene volcanic rocks.

The Bijgerd fault, which is the most important structural feature in the Bijgerd-Kuh e Kharchin area (Figure 1.2b) is one of the subsidiary faults of the main, NW-SE striking Kushk Nosrat fault that extends from west of Hoz e Sultan, west of Saveh, to northwest of Saveh, and connects to the Avaj fault, northwest of the area around Hamedan.

The Bijgerd fault is apparently a thrust fault with a left-lateral strike-slip component, and its minimum age may be post-Eocene.

The Bijgerd fault is cut by smaller left- and right-lateral strike-slip faults, which given that they cut the Qom limestone, these smaller faults must be post Oligo-Miocene, although in places, they may be as young as Quaternary. However, the latest movement along these faults is not documented yet.

The general trend of the geological units in this area is NW-SE, which is parallel to the fold axes, although this trend is changed around the Bijgerd fault, probably indicating rotation by the fault.

CHAPTER 2

METHODOLOGY

This thesis investigation has involved both field and laboratory work. The field work was conducted during the summer of 2008 and resulted in the construction of a detailed geological map (Figures 1.2, 3.22), a volcano-stratigraphic column (Figure 3.23), two cross sections (Figure 3.24), and sampling for geochemical analyses.

The 1:50,000 aerial photographs, available from the Military Geographic Organization in Iran, and Landsat satellite photomaps were used to locate the sampling site and for mapping purposes.

The laboratory analytical methods involved petrographic study and microprobe and geochemical analyses.

The petrographic study, using an optical microscope, was conducted at the Petrology Laboratory of the Department of Geosciences, Georgia State University (GSU).

The microprobe analysis was carried out in the fall of 2008 on selected samples, applying a JEOL JXA-8600 Superprobe, running the Geller Microanalytical laboratory's dQANT32 stage and spectrometer automation, at the Geology Department, University of Georgia (UGA).

The procedures for the preparation of the volcanic and volcanoclastic rock samples, to determine the rare earth element (REE) concentrations employing isotope dilution mass spectrometry (ID-MS) targeting flux fusion dissolutions, were completed at the Laser-ICP Mass Spectrometry Laboratory of the Department of Geosciences, GSU during the spring of 2008.

Other trace element concentrations were determined in a commercial laboratory (Mineral Services SGS, www.sgs.com/geochem) applying the sodium peroxide fusion method (ICP-AES and ICP- MS). The major element concentrations were determined in the summer of 2008, using Rigaku 3270 X-ray fluorescence (XRF) laboratory, at the Geochemistry Laboratory of the Department of Geosciences, GSU.

Sample Preparation

Overall, 24 rock samples were selected from the Bijgerd-Kharchin. All sample sites were located with GPS (Table 2.1). Samples were not taken randomly; they were taken along specific traverses. Since alteration observed in outcrops represents weathering or hydrothermal activity by fluids in volcanic areas, attempts were made to avoid sampling apparently altered and oxidized rock.

Pulverization, sectioning, and powdering of the samples were performed in the college of Earth Sciences, University of Shahid Beheshti, Tehran, Iran. Sledge hammer was used to break the rock apart and expose unweathered parts of the sampled rock. Samples were then pulverized by hammer and powdered in a steel hand mortar, and sieved through 2.5 mm mesh.

Before grounding, all these tools were thoroughly washed and dried. After passing through the sieve, the powder was grind in an agate mortar, which was also cleaned and dried for each new specimen. Specimens from the powder of the selected samples were prepared for major and trace element geochemical analyses.

Table 2.1. GPS coordinates of the studied volcanic rock samples in the Bijgerd-Kharchin area.

Sample Number	Latitude	Longitude
KM 30	N35° 17' 48"	E49° 54' 45"
KM 31	N35° 17' 27"	E49° 55' 26"
KM 32	N35° 18' 14"	E49° 55' 21"
KM 33	N35° 19' 10"	E49° 56' 00"
KM 34	N35° 18' 37"	E49° 56' 20"
KM 35	N35° 19' 09"	E49° 56' 27"
KM 36	N35° 19' 14"	E49° 56' 16"
KM 37	N35° 19' 18"	E49° 56' 26"
KM 38	N35° 18' 08"	E49° 57' 48"
KM 39	N35° 18' 17"	E49° 57' 42"
KM 40	N35° 18' 20"	E49° 57' 40"
KM 41	N35° 18' 35"	E49° 58' 00"
KM 42	N35° 14' 07"	E49° 58' 15"
KM 43	N35° 14' 38"	E49° 56' 06"
KM 44	N35° 14' 27"	E49° 58' 28"
KM 45	N35° 16' 00"	E49° 55' 00"
KM 46	N35° 16' 14"	E49° 55' 06"
KM 47	N35° 17' 15"	E49° 55' 24"
KM 48	N35° 17' 42"	E49° 54' 36"
KM 49	N35° 18' 57"	E49° 55' 53"
KM 50	N35° 19' 07"	E49° 56' 04"
KM 51	N35° 19' 00"	E49° 56' 23"

Petrography

Petrographic analysis helps identifying minerals and rocks, and provides significant mineralogical and textural, hence geochemical and geological evidence to decipher the petrogenetic relationships (Shelley, 1993; Vernon, 2004). An optical microscope was used to investigate the composition, microstructure and texture of the rock samples after they were cut in thin section (Winter, 2001).

Electron Microprobe Analysis (EMPA)

The electron microprobe is a systematic instrument used for the chemical analysis of small amounts of solid materials such as minerals, metals, or glasses (Reed, 1996). EMPA is a versatile analytical technique in geology since it enables determining the compositional variation in the zonings of minerals such as plagioclase, olivine, and pyroxene groups, and calculating their structural formula, exact composition, and variation (i.e., generations) over time (Reed, 1996).

In order to do the microprobe analysis, the standard petrographic thin sections (slides) were prepared by a commercial lab (Spectrum Petrographics, Inc). The slides used were standard, uncovered, 30 micron thick thin sections, with a 27mm x 46mm format. Specimens for EPMA were polished, and surfaces were cleaned so that they were free of dust and oil. From each slide, a couple of zoned minerals of plagioclase, pyroxene, and olivine groups were selected under microscope, and marked by diamond scribe and magic marker. All slides were conductively coated with a layer of carbon through a carbon coating process.

EMPA applies a high-energy concentrated beam of electrons to target samples to create X-rays representing various elements. These X-rays can be compared to the intensity of known X-rays (standard) of elements, which leads to the determination of the chemical compositions of unknown elements (Jansen and Slaughter, 1982). Because rocks are not conducting materials, electrons would be stacked on top of each other in the study samples. The carbon coating process of samples causes the minerals within rocks to conduct electron beams through inner space of the rocks (Kerrick et al., 1973). Therefore, scanning these beams can determine accurate elemental composition in the rock samples (Figure 2.1). After carbon coating process, all slides need to be placed in the holder to get the coordination for each selected/marked mineral (Figure 2.2).



Figure 2.1. Vacuum turbo carbon coater.

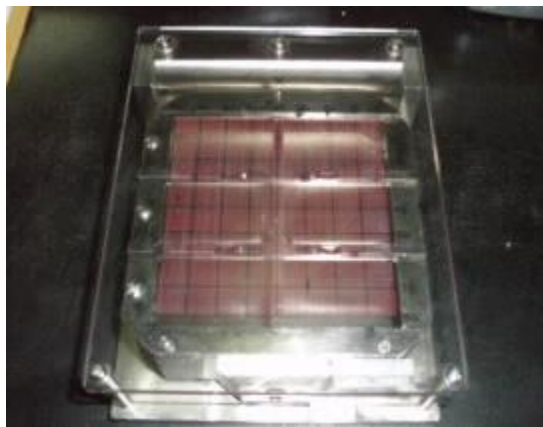


Figure 2.2. Slide holders.

Microprobe analysis was performed with an accelerating voltage of 15kv, 15 nA beam current, approximately 1-5 μm beam diameter, and 10 second counting times. Natural and synthetic mineral standards were used, and analyses were calculated using the J.T. Armstrong's (1988) phi-rho-z-matrix correction. Backscattered electron photomicrographs were acquired using Geller Micro analytical laboratory's dPICT32 imaging software. To minimize the migration of Na of the rock samples, 5 μ beam diameters for plagioclase group and 1 μ beam diameter for pyroxene and olivine were applied in the EMPA of this study (Figure 2.3).



Figure 2.3. The EPMA lab at UGA. It includes, from left to right, an electron gun, and sample chamber with detector array, control console, and monitors.

Trace Element Analytical Methods

Trace elements have concentrations < 0.1 weight percent (wt%) or < 1000 parts-per-million (ppm) of rock's composition (Bowen, 1976). They have an extensive range of valence conditions and ionic radii which can substitute for major elements in minerals where the ionic radii are close enough in value. The majority of the trace elements is varied in the concentrations and appears in a much greater range of concentrations than major elements (Hanson, 1980; Hanson and Langmuir, 1978; White, 2007).

Trace elements are sensitive to processes and conditions such as pressure, temperature, composition, and oxygen activity. The distribution coefficient (K_D) between mineral and the melt is a critical factor for the trace elements. If $K_D > 1.0$, the trace element is said to be compatible compared to the incompatible elements which have a $K_D < 1.0$.

The changes in the concentration do not affect the stability of any phase of the system because the concentration in trace elements is sufficiently low (Hanson, 1980). These qualities typically make trace elements more useful than major elements in petrogenetic studies of igneous rocks.

The rare earth elements (REE) (Table 3.4), which are a subset of the trace elements, are composed of the lanthanide series in the periodic table.

The lanthanide series contain the elements with atomic masses from 57 (lanthanum) to 71 (lutetium) (White, 2007). Yttrium (atomic number 39) also has a charge and ionic radius close to the heavier rare elements (HREE); therefore, it is often referred to as the rare earth element (Jones et al., 1999; White, 2007). Chemically, all of the rare earth elements exhibit a 3^+ oxidation state. Although cerium forms ions with a valence of 4^+ and europium has another valence of 2^+ (Hanson, 1980).

The rare earth elements all reveal similar chemical characteristics since they are comparable in their electron configuration. The filling of the $4f$ orbitals, in the REE's electron configuration, increases with increasing atomic number. This means that the ionic radius systematically decreases as atomic number increases from La to Lu (Jones et al., 1999; White, 2007), resulting in gradual variation between adjacent elements; however the probability of relatively dramatic variation between elements with greater size differences also exists (Hanson, 1980).

The large ionic radii in the REE due to their high charge limit their exchange compatibility and serve them to contribute some substitution or partitioning. For instance, the heavier REE with higher atomic numbers have radii small enough to substitute for Al^{+3} in garnet, while Eu^{+2} preferentially partitions into the plagioclase feldspar where it is determined in anomalous amounts (White, 2007).

The occurrence, distribution, and concentration of the trace elements and investigation of their petrological patterns in rocks help us to constrain the rock's source and mechanisms of origin, which may be useful in determining tectono-magmatic settings (Hanson, 1980).

In this study, the trace element concentrations have been determined applying the sodium peroxide fusion (ICP-AES and ICP-MS) ICPM90 method outlined in Table 2.2 (Mineral Services SGS, www.sgs.com/geochem).

Table 2.2. The detection level of the ICM90A method of SGS used for the trace element analysis in this study. The elements are determined by sodium peroxide fusion/ICP-AES and ICP-MS. The lower and upper detection limits are given for each element.

Ag 1ppm - 0.1%	Ge 1ppm - 0.1%	Sb 50ppm - 10%	Al 0.01% - 25%
Hf 1ppm - 1%	Sm 0.1ppm - 0.1%	As 30ppm - 10%	Ho 0.05ppm - 0.1%
Sn 1ppm - 1%	Ba 0.5ppm - 1%	In 0.2ppm - 0.1%	Sr 0.1ppm - 1%
Be 5ppm - 0.25%	K 0.01% - 25%	Ta 0.5ppm - 1%	Bi 0.1ppm - 0.1%
La 0.1ppm - 1%	Tb 0.05ppm - 0.1%	Ca 0.01% - 35%	Li 10ppm - 5%
Th 0.1ppm - 0.1%	Cd 0.2ppm - 1%	Lu 0.05ppm - 0.1%	Ti 0.01% - 25%
Ce 0.1ppm - 1%	Mg 0.01% - 30%	Tl 0.5ppm - 0.1%	Co 0.5ppm - 1%
Mn 10ppm - 10%	Tm 0.05ppm - 0.1%	Cr 10ppm - 10%	Mo 2ppm - 1%
U 0.05ppm - 0.1%	Cs 0.1ppm - 1%	Nb 1ppm - 1%	V 5ppm - 1%
Cu 5ppm - 1%	Nd 0.1ppm - 1%	W 1ppm - 1%	Dy 0.05ppm - 0.1%
Ni 5ppm - 1%	Y 0.5ppm - 0.1%	Er 0.05ppm - 0.1%	P 0.01% - 25%
Yb 0.1ppm - 0.1%	Eu 0.05ppm - 0.1%	Pb 5ppm - 1%	Zn 5ppm - 1%
Fe 0.01% - 30%	Pr 0.05ppm - 0.1%	Zr 0.5ppm - 1%	Ga 1ppm - 0.1%
Rb 0.2ppm - 1%	Gd 0.05ppm - 0.1%	Sc 5ppm - 5%	

Since sodium peroxide fusion is a low temperature fusion, hydride elements are not volatilized. The fusion procedure typically involves complete dissolution of the sample in molten flux. The ICP95A method is suitable for many intractable, difficult-to-dissolve minerals (www.sgs.com/geochem).

Determination of the REE

Rare earth element concentrations were determined applying isotope dilution mass spectrometry (ID-MS). Several different preparation techniques were used to measure the REE concentrations. These include the flux fusion dissolution technique and the isotope dilution/ion exchange chromatography. The flux fusion dissolution technique was used in this study by mixing approximately 100 mg of sample with approximately 400 mg lithium metaborate flux in a pre-fired graphite crucible. To increase the precision in recording the sample weight, the sample powders were measured into the crucible and weighed several times.

In this technique, lithium metaborate flux breaks down all silicate minerals, and adds only lithium (Li) and boron (B) to the solution. This allows the separation of the REE for the geochemical analysis (Ingamells, 1970). The graphite crucible containing the sample and flux was placed in an 1100° C electric muffle furnace for 15 minutes to entirely melt the sample and flux. At the same time, a clean Teflon beaker, covered in Para film to avoid contamination, containing a magnetic stir-bar, 45 ml of 2 molar HNO₃ and 6 drops of REE spike are placed on a stir plate.

In order to get the best possible data from this technique, the accurate and precise calibration of a multi-element rare earth element spike is required. A multi-element spike, using metallic oxides of polyisotopic rare earth elements (La, Ce, Nd, Sm, Eu, Gd, Dy, Er, Yb, and Lu) with altered isotopic compositions, was prepared at Georgia State University. Except Ce, which is dissolved in trace element grade sulfuric acid, the metallic oxides were all dissolved in concentrated Optima® HNO₃. The two solutions were mixed and then diluted to make a volume of one liter (REE #1). This spike was calibrated using REE concentrations of USGS Geologic Standard BHVO-1 and BIR-1 (Baker et al., 2002).

The REE spike is highly enriched in a single isotope of each element, and it is added to estimate the amount of sample (Eirik Krogstad, personal communication, 2008). The REE#1 spike bottle, removed from the refrigerator, was allowed to achieve thermal equilibration with room temperature. The spike bottle was carefully weighed before and after the drops of spike to the beaker and the accurate weight of the spike was calculated by subtraction.

Since some rock samples (e.g. rhyolite) are iron poor, 1 ml iron solution was added to the solution or ~10 mg of ultra-high purity (99.999%) iron powder was added to the samples to get the precipitation (Tomascak et al., 1996).

When the crucible was removed from the furnace, the contents were swirled to collect all the material, and poured into the beaker. Stirring continued until the melted sample was successfully dissolved into the solution.

Co-precipitation of the REE with Fe is completed when the melted sample was totally dissolved (Rankama and Sahama, 1950; Evans and Hanson, 1993). Then, the trace metal grade concentrated ammonium hydroxide (NH_4OH) was added to the solution until the pH was ~ 6.5-7.5 (Figure 2.4).

In this range of pH the color of the solution is changed and the precipitated mass containing the trace elements are appeared and aqueous Fe^{+2} is precipitated as Fe^{+3} oxyhydroxides with which REE are co-precipitated.



Figure 2.4. Pouring the melted sample into the beaker.

The solution was then transferred into a 50 ml centrifuge tube, pre-cleaned with a rinse of 2% HNO_3 , and placed in a centrifuge for almost 5 minutes at 4750 rpm. The supernatant fluid was thrown away and 45 ml Milli-Q water was added to the centrifuge tube and shaken to raise the precipitate.

The precipitate was then dissolved by adding 2ml 2M optima HCL and shaking the tube. Meanwhile, ion exchange columns filled with resin (AG 50W-X8) are floated with Milli-Q water. These primary columns (Figure 2.5) was cleaned and equilibrated using specific volumes of 6M trace metal grade HNO₃ and 2M Optima HCL.

Then the dissolved precipitate from the centrifuge tube was carefully loaded through a filter paper cone (11 mm diameter particle retention) to eliminate the presence of graphite particles on the column. The filter cone was placed in polypropylene funnel which was already placed to the prepared 15 mL cleaned centrifuge tube onto the ion exchange column (Figure 2.5).



Figure 2.5. Primary (exchange) columns filled with resin (AG 50W-X8).

After the whole sample fluid was dripped through the primary column, the column was washed with 2M Optima HCL and then by 2M trace metal grade HNO₃. The REE finally were eluted by adding 5mL of 6M trace metal grade HNO₃.

This solution was collected in a clean vial and then dried on a hot plate. In order to reduce the acid degradation in the resin bed, the column needed to be washed with Mill-Q water.

The secondary chemical separations of the REE was done using custom-made 25x 2.2mm PFA Teflon column with different amount and molarities of 2-Methylacetic acid which is also known as α -Hydroxyisobutyric acid, α -HIBA (Figure 2.6).



Figure 2.6. Secondary (exchange) columns or α -HIBA. Secondary columns filled with resin (AG 50W-X4).

A more precise analysis of the individual elements can be determined through the Ion Exchange Chromatography procedure. The variable distribution coefficients are used to separate the individual REE elements. For the secondary chemical separation, α -HIBA column, the column needs to be completely filled with resin (AG 50W-X4).

The dried REE concentrations were dissolved in 40 μ L of 1M Optima HCL and then diluted with 360 μ L of Mill-Q water to make a 0.1 M HCL solution.

The cleaned and labeled vial was used to collect each eluted free REE separates. Using α -HIBA results in the elution of heavy REE (HREE), middle REE (MREE), and then the light REE (LREE). The first separation to be eluted includes Lu using 1.5 mL of 0.10 M α -HIBA. Because of the existence of Hf in the samples, and even the calibrated column, the Lu separation is contained in the Hf and Yb.

The heavy REE (HREE) separation (Yb, Tm, Er, Ho, Dy, and Tb) is eluted with 1.75mL of 0.15M α -HIBA. During this study, the absence or presence of Tb was insignificant because Tb is monoisotopic and its concentration was not evaluated. The Gd separation is eluted using 1.5 ml of 0.15M α -HIBA. The 5.0 mL of 0.225M α -HIBA is used to elude the middle REE (Eu, Sm, Nd, and Pr). The Ce is eluted with 1.0 mL of 0.5M α -HIBA. Finally, the La separation is eluted using 1.0 mL of 0.5M α -HIBA.

The stated procedures take 14-16 hours to complete. The next step was diluting all of the collected solution using 2% Optima HNO₃, and then analyzing them by mass spectrometry.

The collected isotopic ratios were exported into a MS Excel spreadsheet to calculate the element concentrations by the isotope dilution equation.

The Leedeey chondrite abundances (Masuda et al., 1973, as reported in Hanson, 1980) were used for normalization in this investigation (Table 3.4).

The high precision isotope dilution ICP-MS analytical technique combined by more than 2% precision and accuracy of the Leedeey chondrite analysis (Hanson, 1980) consequences the smooth REE patterns of the studied samples to investigate the interpretive comparisons.

Major Element Analysis

Major element concentrations are commonly applied to describe and classify rocks. They supply significant clues for geochemical classification and petrogenetic relations. Twenty four samples were selected, and fine powdered, for major element analysis. Ultra-pure lithium tetra borate (LTB) flux needed to be baked at 550^o C for three hours in the electric muffle furnace (Thermolyne Type 46100).

The crucible was removed from the hot furnace and placed in the desiccating cabinet to achieve the thermal equilibration with room temperature. The measuring dish was placed onto a digital scale and scaled zero.

Precisely 4.5 grams of baked ultra-pure lithium tetra Borate flux was weighed and 0.5 grams of each sample added for a total mixture of 5.000 grams (Figure 2.7).

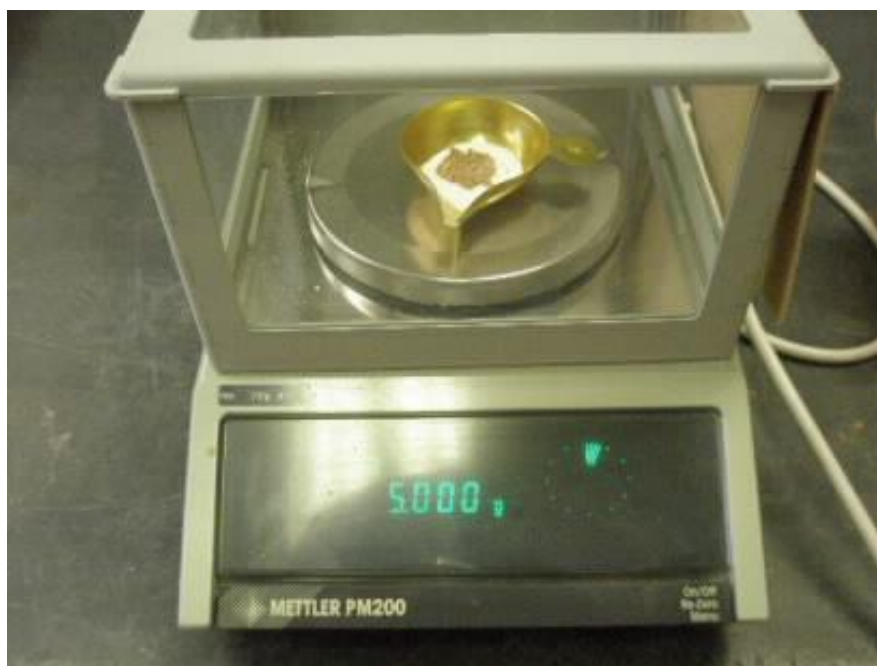


Figure 2.7. The weighting of the rock sample and flux into a digital scale.

The mixture gently was poured into a small glass (cap) vial and shaken to mix flux and rock powder completely. The mixture was then emptied into platinum crucible.

The platinum crucible containing the sample and flux was placed in an 1100° C furnace for 15-20 minutes to entirely melt the sample and flux. In this case, the platinum cover was put onto crucible by the close-fitting heat glove and the platinum tipped tongs (Figure 2.8).



Figure 2.8. The platinum crucible containing the sample and flux in the 1100° C furnace.

The Bunsen burner was ignited by turning on the compressed air first and then the air was adjusted to get appropriate flame. Then the platinum crucible cover was removed by the platinum tipped tongs and the crucible was placed into the hot triangle over the flame.

The crucible was gently stirred up by the tongs to eliminate the bubbles in the melt (Figure 2.9).

The crucible was placed into furnace for another 5-10 minutes. The Bunsen burner needed to be turned off and then re-ignited as before.

The platinum mold was placed into hot triangle and heated up to change to the orange color. Then, the crucible was carried by its left hand side, and removed as before and emptied into the hot mold (Figure 2.10).

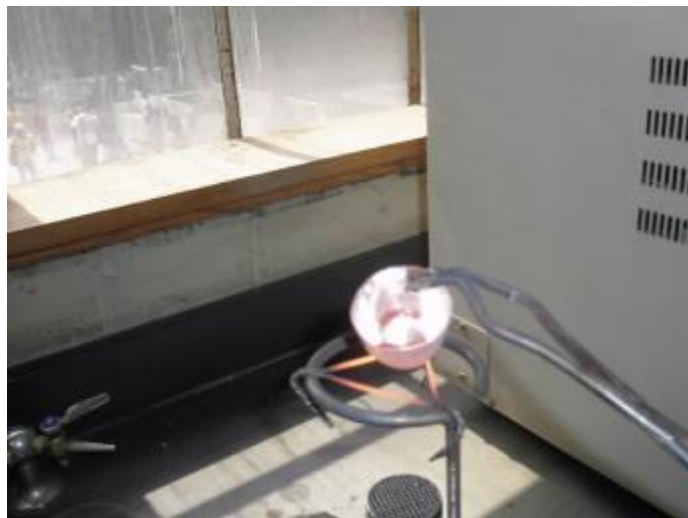


Figure 2.9. Stirring up the crucible was over the hot triangle.

The empty crucible needed to immediately be dropped into acid bath (HCL 10%) and placed under the hood. The mold was agitated to get the melt to cover the bottom of it smoothly and completely. After cooling the mold (10 minutes), the sample number was written on the outer surface by permanent marker.



Figure 2.10. Pouring the melt into the hot mold.

Then the mold was flipped and the glass disk was extracted. All glass disks needed to be placed in the desiccating cabinet (Figure 2.11).

The glass disks were analyzed on a Rigaku 3270 X-ray fluorescence (XRF) spectrometer using a Rh tube, operating voltage of 50 kv and operating current of 50 mA (Figure 2.12).



Figure 2.11. The desiccating cabinet containing the glass disks.

Results are reported as weight percent (wt %) SiO_2 , TiO_2 , Al_2O_3 , Fe_2O_3 , MnO , MgO , CaO , Na_2O , K_2O , and P_2O_5 . The rock samples were also run at three different times to ensure that the recorded data were of the highest precision. Additional support for the precision and accuracy of this method is derived based on duplicate analyses of some USGS standard (e.g., BHVO-1, IR) (Table 3.2). The Loss on Ignition (LOI) test, the difference in weight before and after igniting, for all samples is determined to measure the amount of volatile substances (e.g., H_2O and CO_2) and impurities escaped during the heating (Table 3.2).



Figure 2.12. Rigaku 3270 X-ray fluorescence spectrometer at Georgia State University.

CHAPTER 3

RESULTS

Field Work

The thesis project involved investigations in the field and laboratory. The Bijgerd-Kharchin area exposes Middle and Late Eocene tuffaceous sandstone, lava, and volcaniclastic rocks (Figure 3.1). The field work was conducted during the summer of 2008, and resulted in the construction of a detailed geological map (Figure 3.2a, b), two cross sections (Figure 3.2b), and a volcano-stratigraphic column (Figure 3.2c). Based on field work and inspection of the Nobaran 1:100,000 map, the Middle Eocene volcanic and volcanic-sedimentary rocks were divided into two units (Figures 3.2, 3.3): E^v: Phyric andesite and E^{gt}: green tuff, lithic tuff, with local shale, sandstone, and hyaloclastite. The descriptions of the stratigraphic units, from oldest to youngest, are given in the following sections.

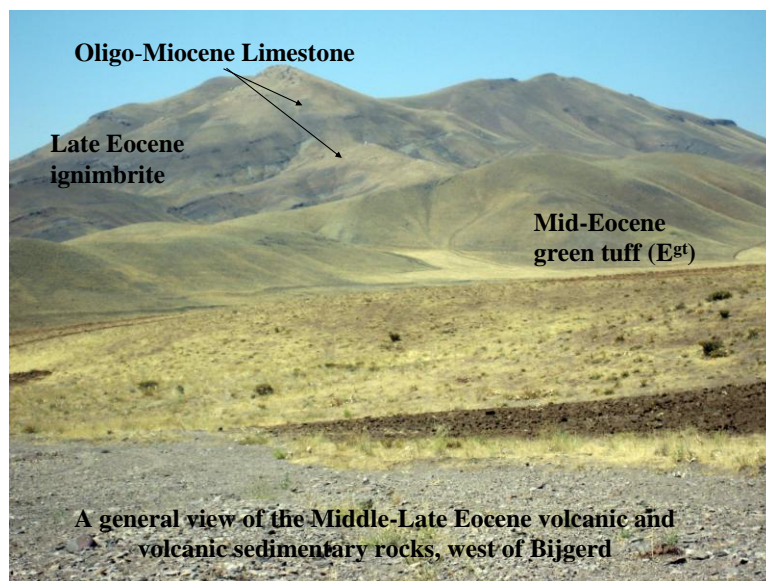


Figure 3.1. General view of the Mid-Late Eocene volcanic rocks of the study area.

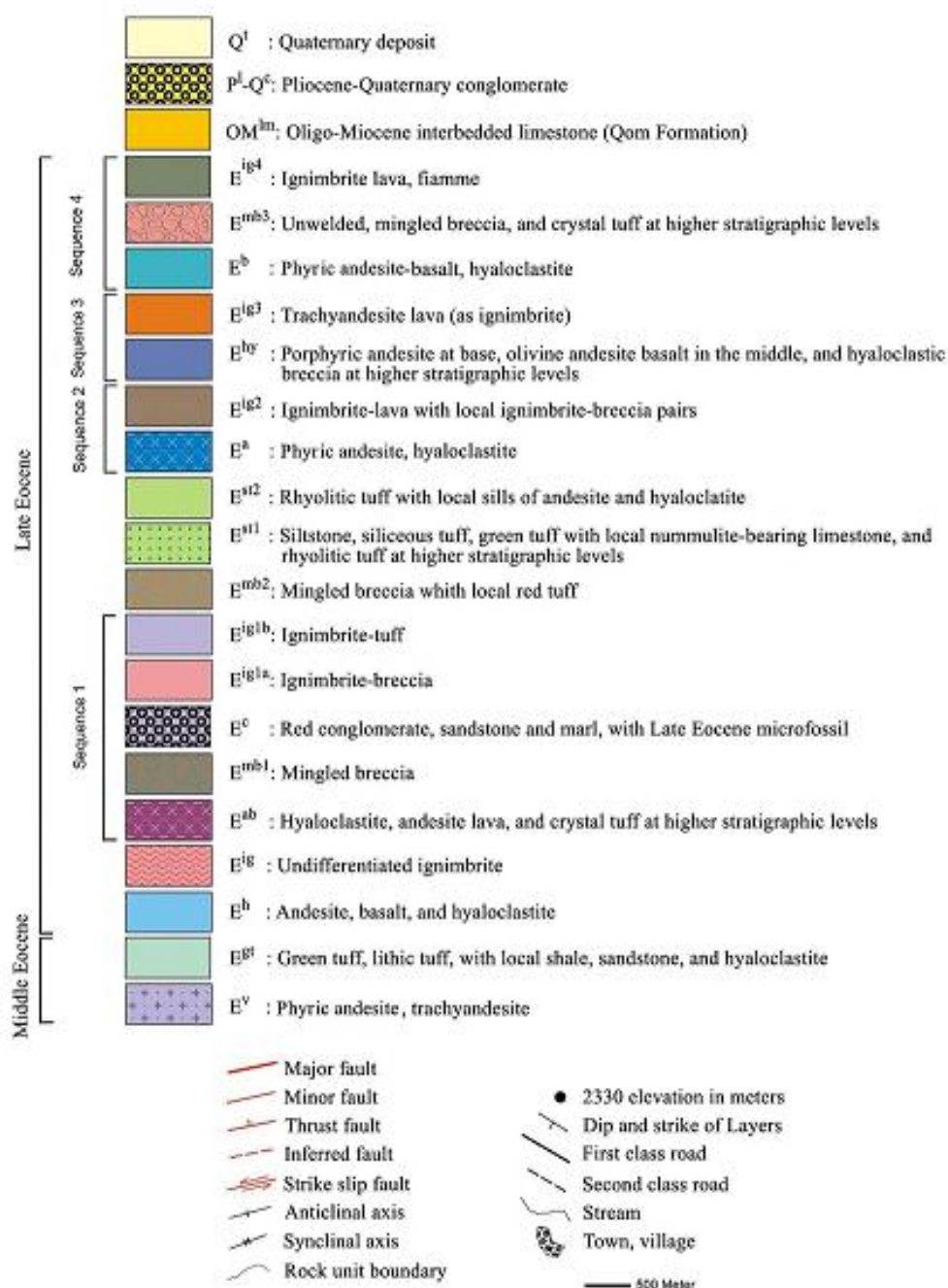


Figure 3.2a. Legend for the geological map of the Bijgerd-Kharchin study area.

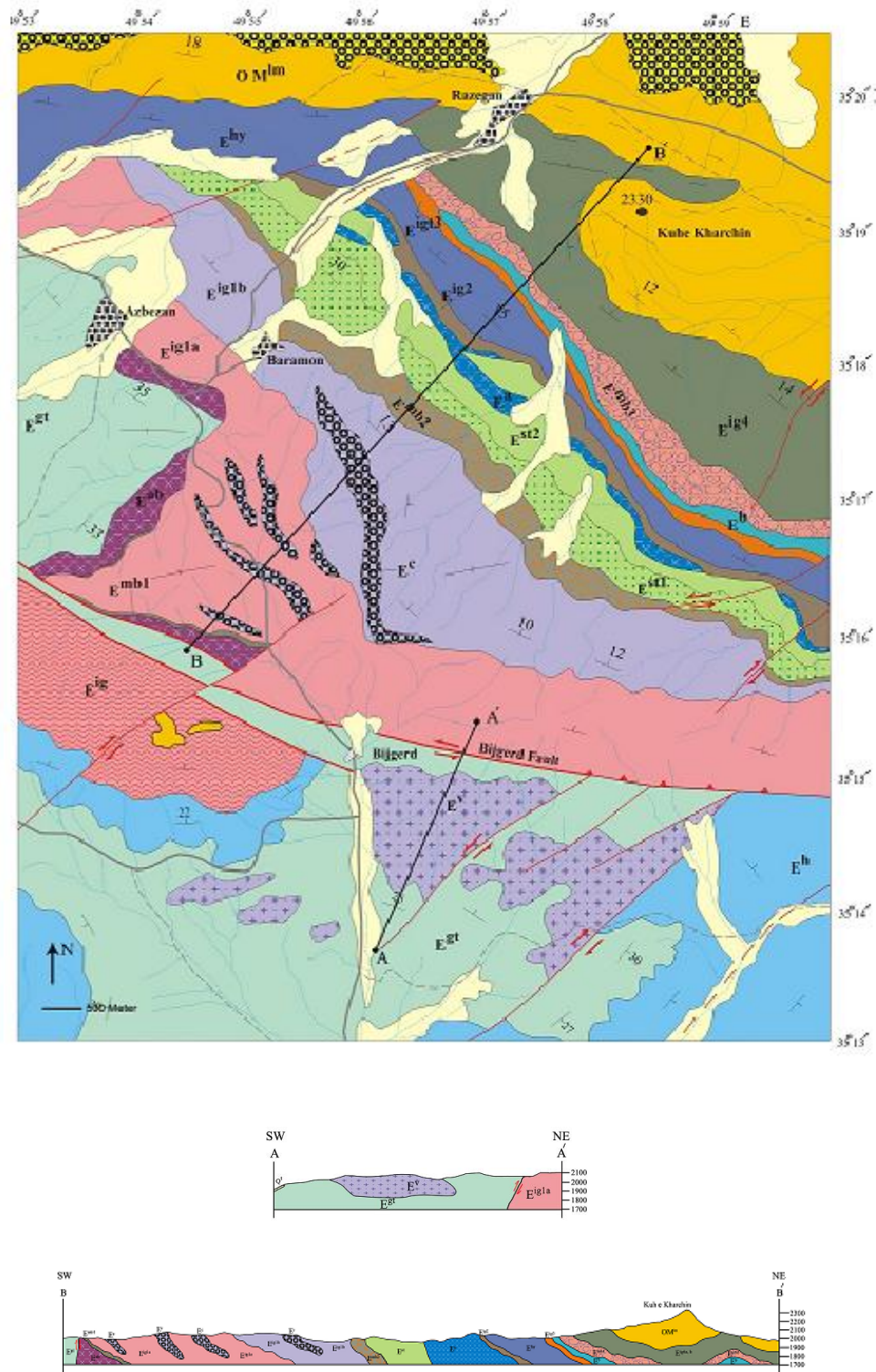


Figure 3.2b. Geologic map and cross sections of the Bijgerd-Kharchin study area.

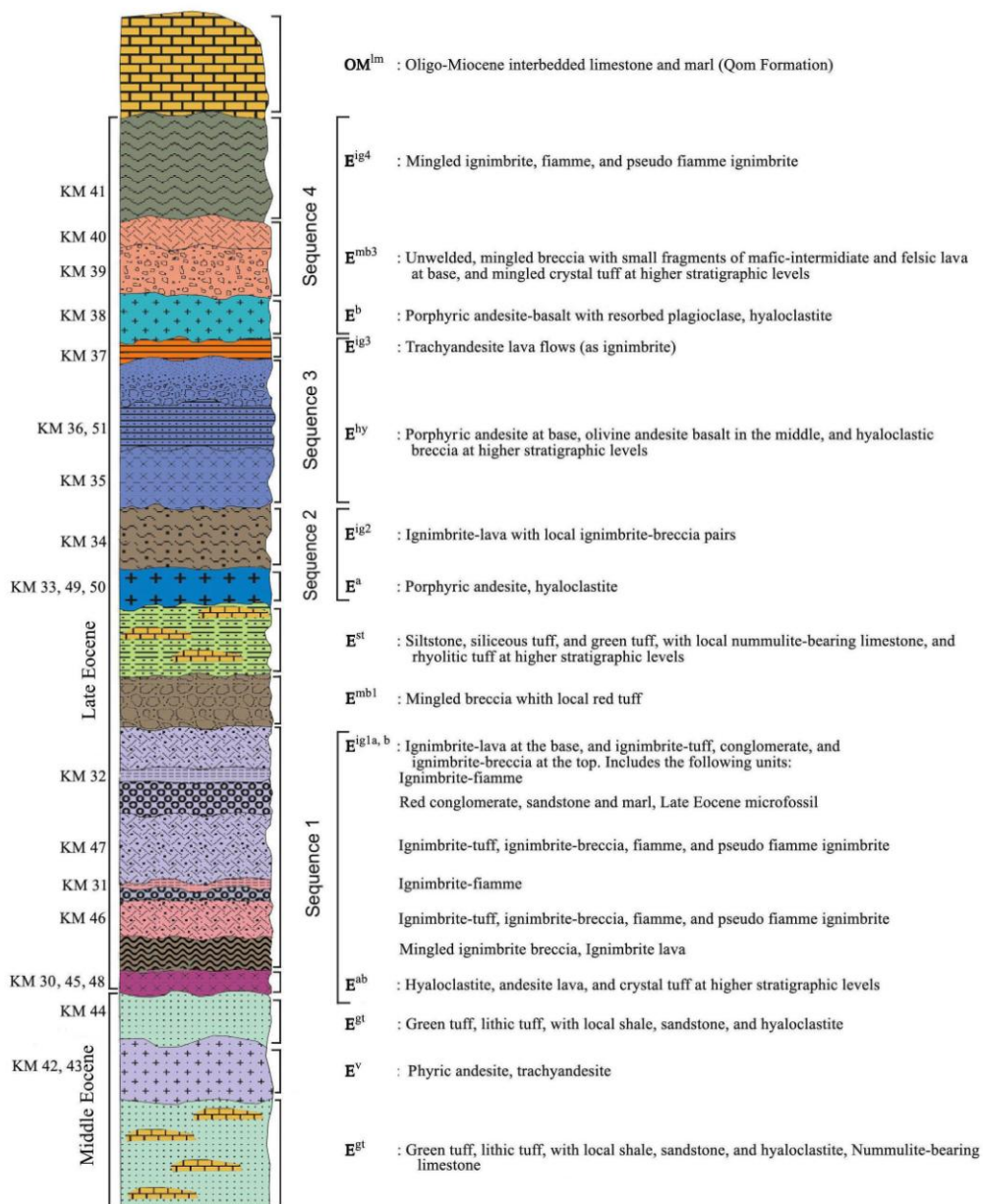


Figure 3.2c. Volcano-stratigraphic column of the Bijgerd-Kharchin area. It is showing the stratigraphic position of the studied samples.

Est Unit

This unit, exposed in the southern part of the mapped area, is made of green tuff with some lithic tuff, sandstone, shale, and sporadic layers of conglomerate and lenses of Nummulite-bearing limestone. In places the Est includes hyaloclastic lava with interlayers of andesitic and basaltic composition, which is designated by E^v on the map. The rocks making up the E^v unit are deformed into anticlines and synclines in the southern part of the mapped area, south of the Bijgerd fault. The green tuff is dominantly made of volcanic grains, which due to explosive acidic eruptions were ejected as glass shards (now devitrified) and other fragments into a marine environment, forming green minerals such as chlorite and epidote, with various clay minerals (Winter, 2001). Light-colored rhyolitic tuff is exposed in the southwestern part of the map and in the western part of the study area, south of Kuh e Inche Ghareh, reaching a thickness of about 1000m. The following Middle Eocene microfossils were identified in the Nummulitic limestone, west of the mapped area, and east of the Badam Jalogh village by the Paleontology Department of the Geological Survey of Iran in 2000 and 2007:

Nummulites millecapit, *Operculina complanata*, *Amphistegina sp.*, *Asterigerina sp.*, *Assilina sp.*, *Operculina sp.*, *Radiolaria sp.*, *Lithophylum*.

South of the map, and south of the Bijgerd fault, the E^v unit occurs in, and units E^h and E^{ig} lie on top of the Est unit.

E^v Unit

This unit is mainly exposed south of the map area, south of the Bijgerd fault in the Est unit. E^v is made of a sequence of hyaloclastic breccia and tuff at the base, which grade upward into phyric lava, followed by aphyric lava, and finally autoclastic breccia at the top (Figure 3.3).

A series of green tuff and breccia of the E^{gt} unit overlie the E^v unit. The contact between the hyaloclastic breccia and tuff at the base of this unit with the E^{gt} unit is gradational, i.e., first the phyrlic lava occurs as interlayers in the green tuff, followed by the tuff and hyaloclastic breccia.

The tuff grains vary in size between few cm to few mm, and the smaller grains, are substituted with green minerals such chlorite and epidote, probably because of reaction with water while the larger grains are more intact. Some grains are also oxidized.

Upper in the section, phyrlic lava was deposited as flow over the tuff and hyaloclastic breccia. Hand specimens of these rocks show altered phenocrysts of clinopyroxene and plagioclase. Aphyric lava overlies the phyrlic lava. Thick autoclastic breccia, few tens of meters thick, occurs at the top of this unit, and is made of aphyric andesitic clasts and a matrix of smaller clasts of the same lithology. In places, large clasts are broken into several clasts like a jigsaw puzzle. The clasts have a crenulated contact, and it seems that the breccia formed as a result of the accumulation and fall of broken aphyric lava from the edge of a cliff.

Higher in the unit, the density of the vesicles reduces, and lavas resemble flows on land. After the deposition of the autoclastic breccia, which apparently occurred on land, a variety of tuff and green breccia with hydrated volcanic clasts were deposited on the autoclastic breccia, again indicating formation of the tuff in a marine environment. Higher in the unit, the density of the vesicles reduces, and lavas resemble flows that form on land. After the deposition of the autoclastic breccia, which apparently formed on land, a variety of tuff and green breccia, with hydrated volcanic clasts, were deposited on the autoclastic breccia, again indicating formation under water.

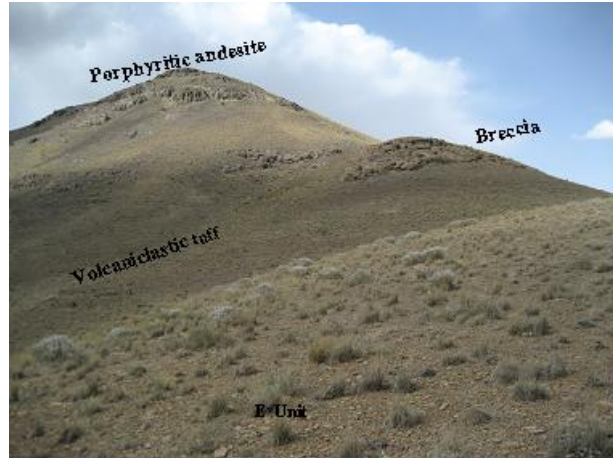


Figure 3.3. A general view of the Middle Eocene volcanic rocks of the E^V unit.

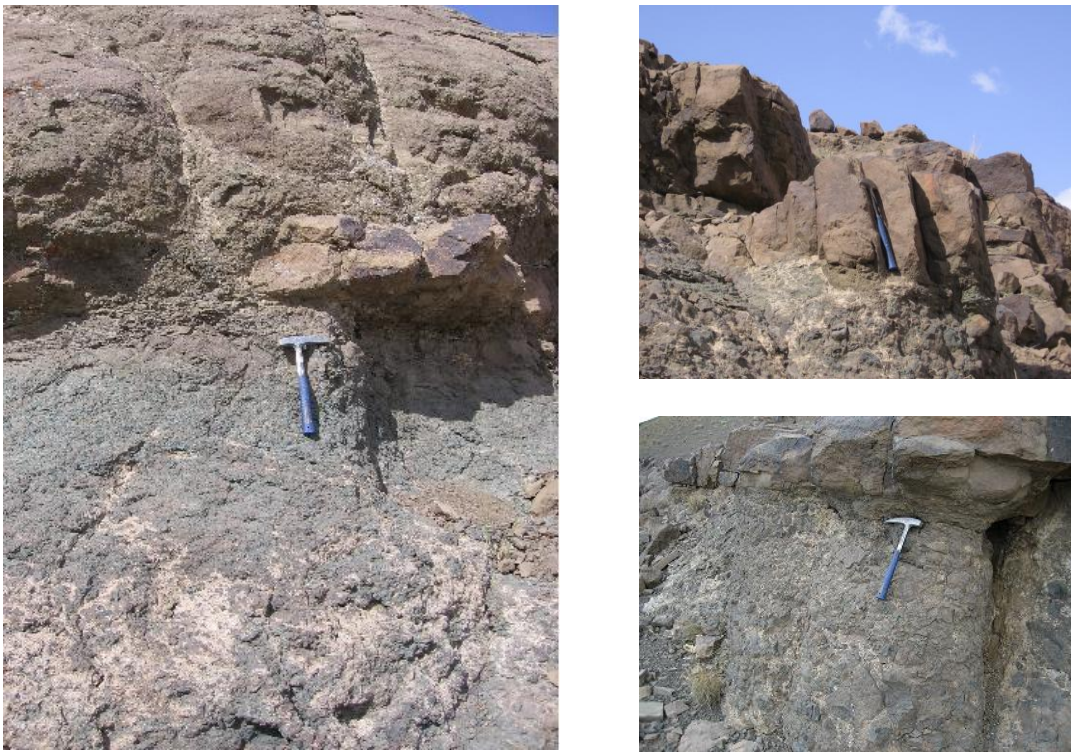


Figure 3.4. A sequence of hyaloclastic breccia and tuff at the base. It is followed by aphyric lava of the E^V unit. Scale provided by rock hammer.

Upper Eocene Volcanic Units South of the Bijgerd Fault

The Upper Eocene volcanic units south of Bijgerd, designated as E^h and E^{ig}, are extensively exposed northwest of Saveh. These units are comparable with four horizons of bimodal volcanic rocks north of the Bijgerd fault (Figure 3.2b).

E^h Unit

The E^h unit is exposed in the area south of Bijgerd, and includes hyaloclastite with basaltic, olivine basaltic, and andesitic-basaltic compositions. In places, this unit is cut by feeder dikes or is interlayered with andesitic and basaltic tuff, or calcareous tuff containing lenses of Nummulite-bearing limestone.

The following microfossils give a Late Eocene age for the Nummulite-bearing limestone north of the Badam Jalogh village, west of the Bijgerd highlands:

Nummulites fabiani, *Nummulites sp.*, *Nummulites cf. globules*, *Discocyclina*, *Assilina sp.*, *Operculina sp.*, coral, and algal debris (Geological Survey of Iran, 2008).

The E^h lavas were probably laid down in shallow marine environment, and for this reason, they form few cm to mm wide blobs (lumps) in a highly hydrated, oxidized, and altered volcanic matrix. In many cases, the exterior of the margins of these blobs is made of volcanic glass or oxidized material, while the interior parts are more intact, and have preserved original volcanic texture and structure. South of the map, these lavas lie on green tuffs of the E^{gt} unit, and are covered by ignimbrites of the E^{ig} unit. The thickness of this unit ranges between 150 m and 200 m.

E^{ig} Unit

This unit is exposed in the southern part of the mapped area and includes a variety of ignimbrites. Given of the considerable extent of this unit west and east of the Bijgerd-Kuh e Kharchin, and because of being covered by the Oligo-Miocene Qom Formation, it is not possible to correlate this unit with any of the units in the Bijgerd-Kuh e Kharchin section. The thickness of this unit west of Bijgerd is about 200 m, but outside of this area, around the Sangak village north of Nobaran, is about 500 m (Nobaran 1:100,000 Quadrangle).

Upper Eocene Volcanic Units in the Bijgerd-Kuh e Kharchin Section

These units are designated on the map with E^{ab}, E^{ig1a}, E^{ig1b}, E^{st1}, E^{st2}, E^a, E^{ig2}, E^{hy}, E^{ig3}, E^b, E^{mbr}, E^{mt}, and E^{ig4}. The descriptions of these units are given below.

E^{ab} Unit

This unit is exposed to the north of the deserted Bijgerd village. E^{ab} comprises a sequence of hyaloclastite, andesitic lava at the base, and andesitic crystal tuff at the top. The green and hydrated minerals (e.g. chlorite and epidote groups) in hyaloclastite of E^{ab}, produced by the reaction of lava and water (Winter, 2001), are cut by veinlets of carbonate minerals oriented in different directions.

The same carbonates also occur in the hyaloclastite (Figure 3.5a). The lavas are vesicular in places, and the vesicles are filled with green minerals such as chlorite and epidote, and calcite. Iron oxides (e.g. hematite) also occur as secondary minerals in the hyaloclastite, giving it a red color (figure 3.5b). The oxidization of lava may have occurred because of eruption into an aqueous environment (Brain et al., 2002).

The andesitic crystal tuff is medium to thinly layered, and cut by veinlets filled with iron oxides (e.g., hematite). In the north western part of Bijgerd, the E^{ab} is tectonized at its base, and overlies the E^{gt} unit through a branch of the Bijgerd fault (see map). However, a series of mingled and hybrid breccia of the E^{mb1} unit covers it. E^{ab} may be the first basic-intermediate lava of the bimodal volcanic rocks of the Bijgerd-Kuh e Kharchin area.



Figure 3.5a. Carbonate minerals in the hyaloclastite. 3.5b. Iron oxide minerals in the hyaloclastite of the E^{ab} unit.

E^{mb1} Unit

The E^{mb1} unit lies above the E^{ab} crystal tuff and under the E^{ig1a} ignimbrite (the first level of Late Eocene ignimbrite), and includes mingled and hybrid pyroclastic breccia (Figure 3.6). This unit may be hybrid part of the first occurrence of basic-intermediate lava under the ignimbrites of the E^{ig} sequence. It includes light felsic (rhyolitic) and dark, oxidized mafic-intermediate clasts and inclusions.

Clast size ranges between a few millimeters to several centimeters. The crenulated contacts on the edges of the mafic-intermediate clasts are shown in Figure 3.7. In some cases, mafic clasts contain plagioclase phenocrysts.

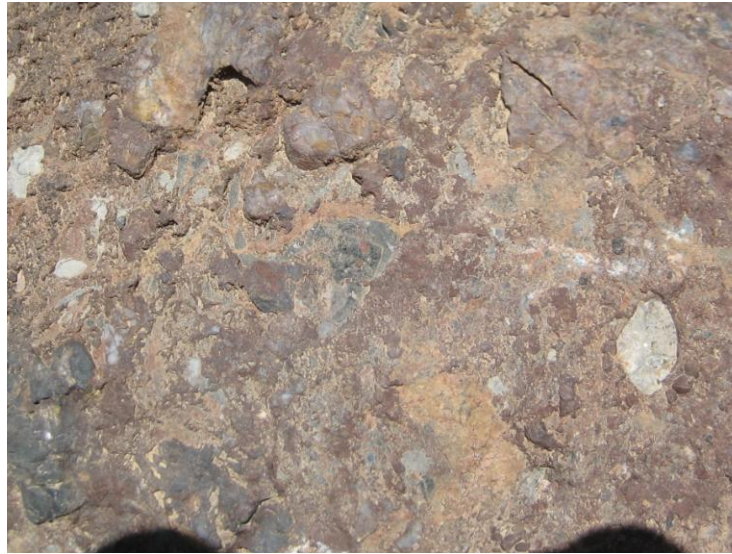


Figure 3.6. Conglomerate of the E^{mb1} unit.



Figure 3.7. The crenulated contact on the mafic-intermediate clast edges (E^{mb1} unit). Pen cap provides scale.

E^{ig1a} and E^{ig1b} Units

The E^{ig1a} and E^{ig1b} units are the first occurrences of the felsic-ignimbrite in the Bijgerd-Kharchin area (Figure 3.8) and include ignimbrite-fiamme, ignimbrite-tuff, and ignimbrite-lava pairs, and red conglomerate, and some sandstone and marl which are designated as E^c (Figures 3.9, 3.10).

Mafic-intermediate inclusions inside the felsic groundmass of some ignimbrites modify the composition of the rock from rhyolite to trachyandesite. These inclusions have varying sizes and are aligned with the flow direction in the ignimbrite.

The presence of fine and microscopic flame and vermicular pseudo-flames, filled with quartzo-feldspathic minerals shown in Figure 3.29. The longest dimension of the elongated vesicles, like that of the basic-intermediate inclusions in the ignimbrite, aligns with the direction of the ignimbrite flow.

Extensive ignimbrites-fiamme, including pseudo-flames filled with intermediate lava, which in some cases contain plagioclase phenocrysts, are exposed along the Bijgerd pass toward the Barehmoon village (Figure 3.11).

At higher stratigraphic levels, the ignimbrites are more explosive, forming different kinds of ignimbrite-tuff (E^{ig1b}). These rocks have a flaky weathering, producing thin sheets. The E^{mb2} is laid down on this unit (Figure 3.11).

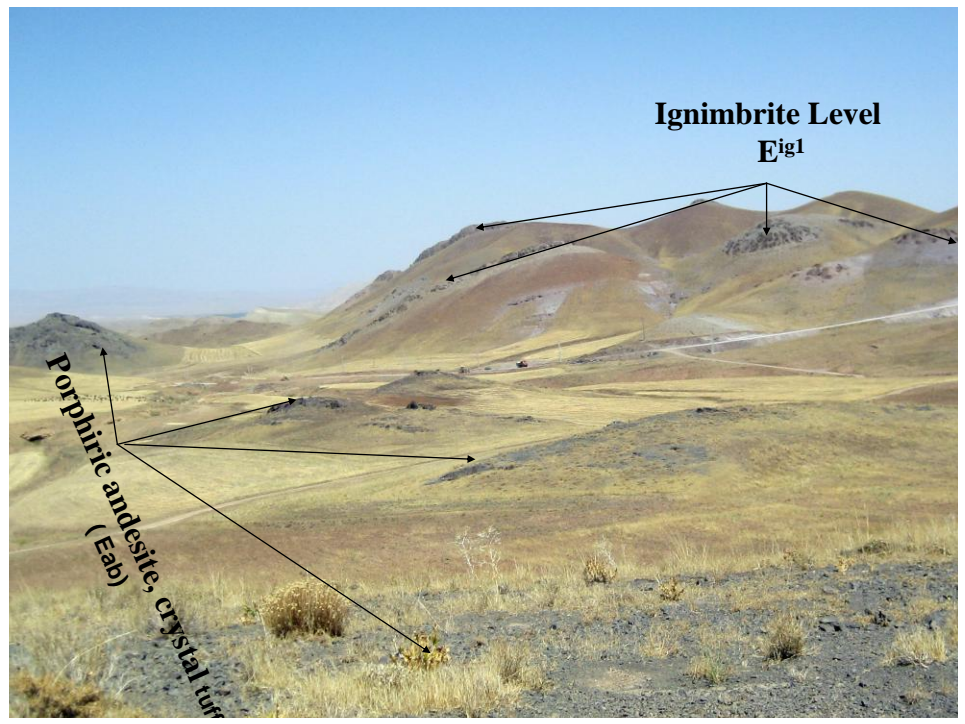


Figure 3.8. A general view of the Late Eocene volcanic rocks (E^{ab} and E^{ig1} units).

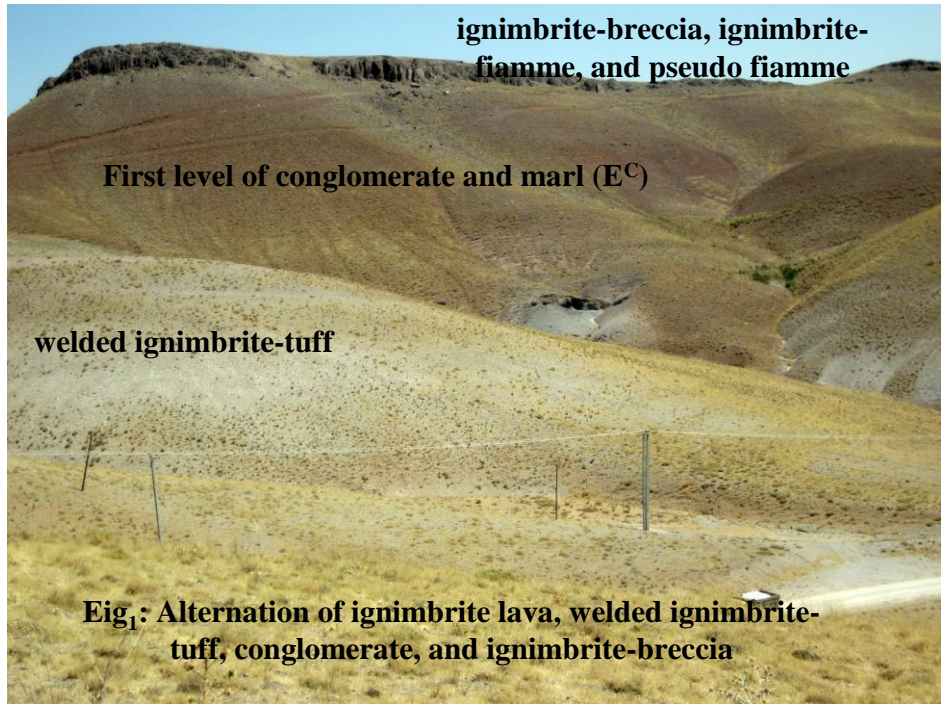


Figure 3.9. Ei^{s1} unit includes ignimbrite-tuff, ignimbrite-breccia, and ignimbrite fiamme.



Figure 3.10. E^{ig1} unit: Conglomerate, and sandstone. Rock hammer provides scale.

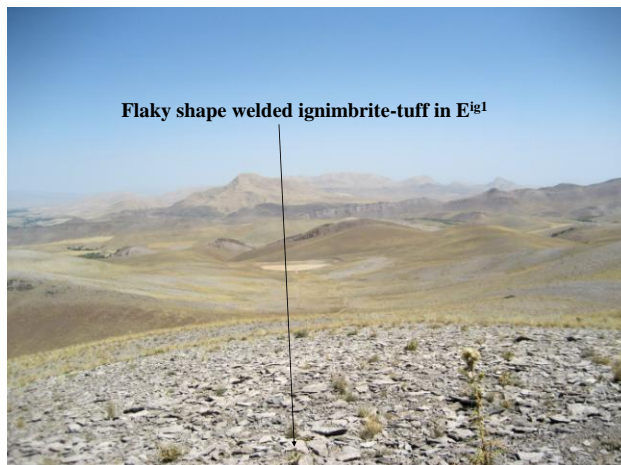


Figure 3.11. Felsic pseudo fiamme field with intermediate lava (on the left), flaky shape welded ignimbrite-tuff (on the right), E^{ig1} unit. Pen cap provides scale.

E^c Unit

The E^c unit occurs as layers, up to 30 meters thick, in the ignimbrite, of the E^{ig1a} unit, and is dominated by conglomerate and some red sandstone and marl. Although these rocks are interpreted on the 1:250,000 geological map of Saveh (Amidi et al, 1984) as the product of the Oligo-Miocene volcanic activity, the 1:100,000 Nobaran Quadrangle Map (Khalatbari et al., 2000), and this thesis project, assign a Late Eocene age for them.

The Late Eocene age is based on the following microfossils identified in the marl washings: *Nummulites sp.*, *Nummulites aff.*, *Stiata.*, *Assilna cf.*, *spira.*, *Assilina cf.*, *exponsa* (Geological Survey of Iran, 2007). The pebbles in the conglomerate are mostly moderately- to well-sorted and well-rounded volcanic rock and Nummulite-bearing limestone.

The following microfossils give a Middle Eocene age for the Nummulite-bearing limestone pebbles: *Nummulites cf globules*, *Nummulites millecapit*, *Operculina complanata*, *Operculina sp*, *Amphistegina sp.*, *Asterigerina sp.*, *Discococylina sp.*, *Assilina sp.*, *Operculina sp.*, *Lithophylum.*, *Algal debris.*, and *Crinoid*. No limestone pebble younger than Middle Eocene has been found.

E^{mb2} Unit

The E^{mb2} unit which is the second horizon of the hybrid breccia, is exposed on the road to the Barehmoon village, and extends to the west. This unit is mostly hybrid breccia with some red tuff at the base. The general characteristics of the hybrid breccia in this unit are the same as those of the hybrid breccia of the E^{mb1} unit.

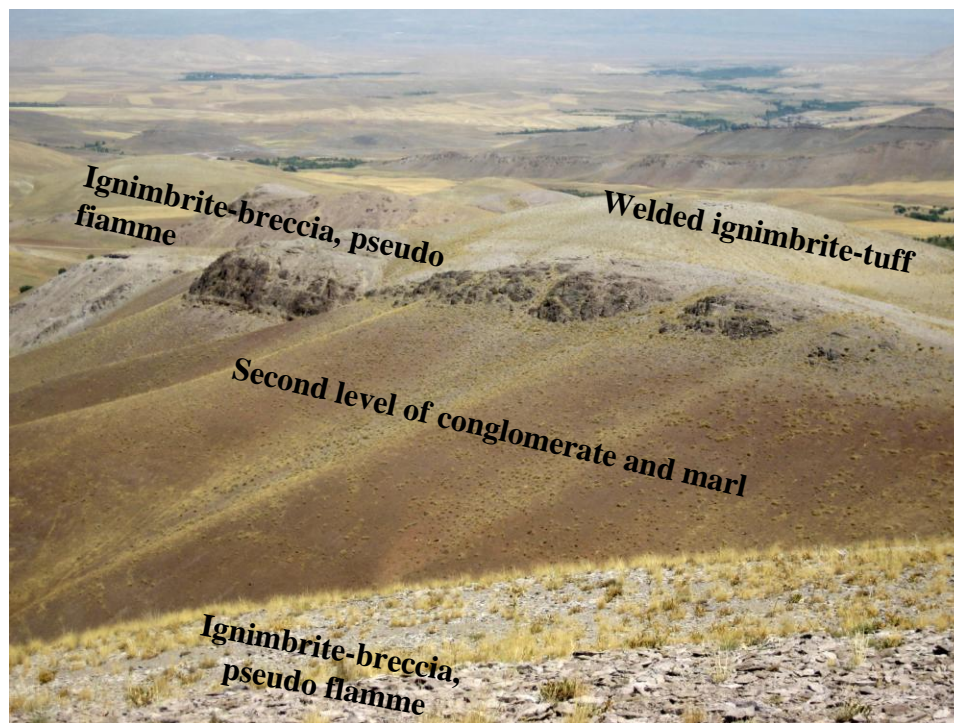


Figure 3.12. A view of E_i^{g1b} , E^c , and E^{mb2} unites.

E^{st1} and E^{st2} Units

The E^{st1} , E^{st2} units, forming high hills with gentle slopes, are exposed in the northern part of the Bramoon village. In the mapped area, the E^{st} unit is divided into two units. The lower unit, designated as E^{st1} on the map, includes volcanic and volcanic-sedimentary rocks, dominated with siltstone, tuffite, and green tuff.

Based on the classifications of volcanic-sedimentary rocks, tuffite includes at least 50% sedimentary material. The tuffite in the E^{st1} unit is characterized by thin, buff-colored layers which fizz with hydrochloric acid (Figure 3.13).

The siltstone and green tuff are thin- to medium-bedded (Figure 3.14). The siltstone and tuffite are more common at the base, and the amount of green tuff increases upsection. The E^{st1} unit grades into the E^{st2} unit higher in the stratigraphic section, which includes green tuff and

rhyolitic ash tuff, reaching a thickness of about 90 m north of the Baramoon village. Both E^{st1} and E^{st2} units contain green tuff and rhyolitic ash tuff with altered glass shards and volcanic ash (Figure 3.15).

Although paleontological study of the E^{st1} unit, which comprises more sedimentary rocks, has not been successful, the following microfossils in a thin limestone layer, east of Kuh e Kharchin, give a Late Eocene age: *Morzovella sp.*, *Globigerinatheka sp.*, *Globigerina sp.*

At the higher stratigraphic levels, the hyaloclastite layers are concordant with layers of the E^a unit that covers these units.



Figure 3.13. A field view of the succession of the E^{ig1} , E^{st} , and E^{ig2} units.



Figure 3.14a. A sequence of siltstone, tuffite, and green tuff in the Est unit. Rock hammer provides scale.



Figure 3.14b. A close view of siltstone(bottom) and tuffite (top) in the Est unit. Compass and pen provide scale



Figure 3.15. A view of rhyolitic ash tuff in the Est unit.

E^a Unit

This unit is dominated by hyaloclastite which occurs as layers in or above the E^{st2} unit, and sits below the first ignimbrite level. Fragments in the blobby and splintered andesitic lava, probably attesting to eruption and cooling under water, have margins that are hydrated and contain a variety of green minerals such as chlorite and epidote. The overlying lava and hyaloclastite are mostly eroded or covered by debris. In this unit the outcrops of barite (BaSO₄) are exposed along the road north of the Baramoon village.

E^{ig2} Unit

This rhyolitic ignimbrite, which covers the E^a unit, contains abundant fine-scale flames and sparse basic inclusions (Figure 3.16). The nature of the eruption in this unit is ignimbrite-lava.



Figure 3.16. Mafic-intermediate enclaves in the ignimbrite.

E^{hy} Unit

This unit is characterized by massive andesitic lava at the base, olivine basaltic lava at the middle, and hyaloclastic breccia at higher stratigraphic levels. It seems that the porphyritic andesitic lava formed on land. Plagioclase phenocrysts occur in a fine-grained groundmass or as few mm long clusters.

Hand specimens of these rocks show vesicles which are filled with agate (cryptocrystalline quartz) along the margin and quartz crystal at the center which grew from rim to the core. Upper in this unit, there are hyaloclastic olivine basalt and patches of olivine basalt enveloped by hyaloclastite.

These lavas are covered by hyaloclastic breccia (see stratigraphic column and Figure 3.17) which contains oxidized, unoxidized, and more or less altered clasts set in a hyaloclastic matrix. Occasionally, the minerals in the hyaloclastites matrix are entirely substituted by green minerals, and in some cases are vesicular. In the upper section of this unit, the clast size decreases.

General characteristics of the E^{hy} unit are as follows: The products of the explosive Late Eocene volcanic/volcaniclastic activity in this area, which constitute the basalt porphyritic, andesitic lava in unit E^{hy}, formed in a dry land environment.

On the other hand, the underlying units, such as Est, formed in an aqueous environment.

Moreover, the olivine basaltic lava at the middle, and hyaloclastic breccia at higher stratigraphic levels, in the E^{hy} unit indicate explosive volcanic/volcaniclastic activity under water, probably in a shallow marine basin.



Figure 3.17. Hyaloclastic breccia located at higher stratigraphic levels in the E^{hy} unit. Rock hammer provides scale.

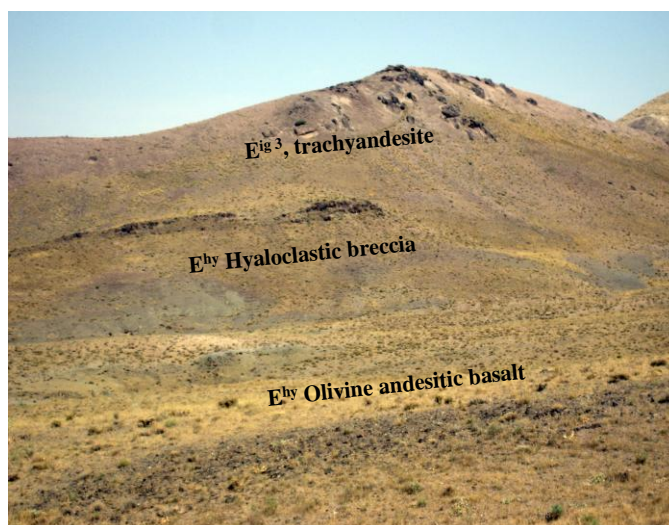


Figure 3.18. A general view of E^{ig3} and E^{hy} units.

E^{ig3} Unit

This unit, extended along an east-west direction, south of the Razghaan village, includes the ignimbrite-lava with trachyandesitic composition, and plagioclase phenocrysts in an aphanitic groundmass with flow structure.

The thickness of this unit is several meters. Unlike those in other units, the ignimbrites of the E^{ig3} unit lack fiamme, or pseudo fiamme.

The mineral lineation and glass flow, and the formation of the fiamme, which are discernible even in hand specimen, however, show that the trachyandesite lavas of the E^{ig3} unit are ignimbrite (Figure 3.19).



Figure 3.19. A hand specimen of the trachyandesite lava of the E^{ig3} unit. Pen provides scale.

E^b Unit

The E^b unit occurs locally west of the Razeghan village, and includes andesitic basalt. This unit is covered by the debris of the overlying E^{mb3} unit in the Bijgerd-Kuh e Kharchin area.

E^{mb3} Unit

The E^{mb3} unit includes the third level of the hybrid breccia in the Bijgerd-Kuh e Kharchin area. The hybrid breccia of the E^{mb3} unit typically represents magma mingling in this area, and can be considered as a marker bed for magma mingling in the Uromieh-Dokhtar zone.

The breccia contains clasts with crenulated contacts, and can be divided into two groups: light colored, acidic or felsic (rhyolitic composition), and dark colored, partly oxidized, basic or mafic-intermediate (Figure 3.20). The light colored clasts are aphanetic and have a rhyolitic composition. The dark colored basic clasts are aphanetic to porphyritic and have a basaltic to andesitic composition. The porphyritic rocks contain large plagioclase phenocrysts set in an aphanetic groundmass. In places, felsic clasts occur in the mafic clasts.

Higher in the section, red, crystal-lithic tuff is defined by alternating dark and light bands. Some of the dark bands are oxidized, and in places have ferromagnesian minerals. The red crystal and lithic tuffs are covered by trachyandesite in which the magma mingling and mixing are probably represented by a mixture of basic and acidic glass shards.



Figure 3.20. Red, crystal-lithic tuff. Pen provides scale.



Figure 3.21. Unwelded, mingled breccia with angular fragments of welded ignimbrite at the base of the E^{mb3} unit.

E^{ig4} Unit

The E^{ig4} unit includes ignimbrite-lava with andesitic composition at the base, and ignimbrite pseudo-fiamme at higher stratigraphic levels. The lower ignimbrite-lava is more massive and contains acidic and basic glass shard (Figure 3.22). Pseudo fiamme-ignimbrite with rhyolitic composition occurs higher in the section. The pseudo fiammes in the ignimbrites occur as long and snaking bands which have been filled by aphanetic minerals such as quartz and, to a lesser extent feldspar.



Figure 3.22. E^{ig4} unit: Mingled ignimbrite, fiamme, and pseudo fiamme ignimbrite.

OM^{lm1}

The OM^{lm1} unit is made of a sequence of limestone, medium to thick beds of sandy-gravelly limestone, and marl, equivalent to the Oligo-Miocene Gom Formation. In places, there are interbeds of conglomerate and rhyolitic tuff.

In the southern limb of Kuh e Kharchin, the base of this unit is not exposed and is entirely covered by limestone scree (Figure 3.23). However, around the town of Elvir, located in the northern part of the study area, Oligocene marl and sandstone, which are equivalent to the Lower Red Formation, are exposed in the lower part of this unit.

The following microfossils give an Late Oligocene (Aquitanian)-Miocene age for the Nummulite-bearing limestone: *Eulepidina elephina.*, *Eulepidina dilate*, *Operculina complanta*, *Miogypsina sp.*, *Lepidocyclina sp.*, *Molepidocyclina sp.*, *Operculina sp.*, *Asterigerina sp.*, and *Cibides sp.* The marl and limestone also have sponges and bivalves.

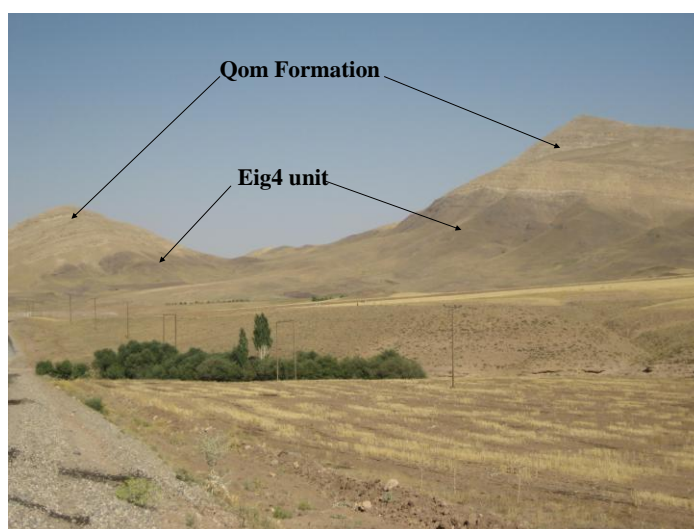


Figure 3.23. Razeghan anticline and Kuh e Kharchin covered by Qom limestone.

Pl-Q^C Unit

The Pl-Q^C unit is exposed to the north of the map area, and forms rolling (hummocky) hills of Pliocene-Quaternary conglomerate which separates the two northern (Alishar) and southern (Bijgerd-Kuh e Kharchin) exposures of the Eocene volcanic-volcaniclastic slivers (Iran 1:250,000 geological map).

This unit is made of a sequence of thickly- to medium-bedded, gently-dipping, folded conglomerate and limestone. The clasts in the PI-Q^C unit include Eocene volcanic rocks, Cretaceous limestone, Oligo-Miocene limestone, and schist. The PI-Q^C unit is estimated to be up to 500 meters thick, and lies, unconformably, over the Eocene volcanic units outside of the study area, and over the Oligo-Miocene limestone in the study area.

Q^t Unit

The Q^t unit includes alluvial plain, old alluvial fan, loose conglomerate with intercalated sandstone and clay, and sporadic travertine.

Petrography

Petrographic analysis helps identifying rocks, and provides significant mineralogical, hence geochemical and geological evidence for petrogenetic relationships (Shelley, 1993, Vernon, 2004). To conduct the petrographic analysis, selected samples from each unit of every sequence were prepared as thin section. Besides the Middle Eocene rock samples, the Upper Eocene volcanic and volcanoclastic rocks in the Bijgerd-Kuh e Kharchin area were petrographically studied for each sequence to understand mineralogic and textural changes through time. The implications of the mineralogical and textural evidence for petrogenetic evolution are summarized and discussed below.

The Middle Eocene Volcanic Rocks (Samples KM 42, 43, 44)

The medium-grained rock samples taken in the Middle Eocene succession (categorized based on field observation, Figures 3.3a-3.3c) include intermediate lava with general basaltic and

andesitic compositions. These rocks (KM 42, 43, 44) are micro porphyries, with the phenocrysts dominated by plagioclase, set in a fine grained groundmass made of tiny plagioclase laths.

However, both KM 43 and 44 are altered, and plagioclase crystals in these samples are calcified.

The phenocrysts of the Middle Eocene rock samples are mostly K-feldspar, and make up approximately 20%-25% of the porphyritic rocks by volume (charts from Folk et al., 1970).

Grain size ranges from less than 0.2 mm to several mm in length. These rock samples (KM 42, 44, and 43) also contain minor rounded and resorbed grains of pyroxene and biotite, besides the ubiquitous laths of plagioclase. Pyroxene is minor, approximately less than 1% of the phenocrysts by volume, altered around the edges, and is mostly clinopyroxene.

Plagioclase laths in these samples (notably in KM 43) display a distinct preferred orientation (around the phenocrysts) and in some cases zoning and polysynthetic twinning. Abundant green and high birefringence minerals (e.g. calcite and chlorite groups) are observed, both as phenocryst inclusions and in the matrix.

Opaque minerals abound, as a ubiquitous partial replacement of some phenocrysts and in the groundmass. Porphyritic texture in these rocks attest to the two-stage cooling of the magma, once at some depth and later at the earth's surface (Winter, 2001).

The Middle Eocene volcanic rocks are petrographically similar; however, the presence of some quartz crystals in KM 44 causes the higher silica content ($\text{SiO}_2 = 59.21\%$) of this sample compared to the others (KM 42 and 43). Moreover, since KM 44 is highly altered, the analytical results obtained of this sample may not reveal magmatic processes.

Late Eocene Volcanic-Volcaniclastic Rocks

Sequence 1 (samples KM 30, 45, 48, 46, 31, 47, 32)

The first Upper Eocene sequence is dominated by porphyritic volcanic and volcaniclastic rocks. KM 30 contains phenocrystic plagioclase with 30%-35% modal composition compared to ~20% for the Middle Eocene rock samples. Although some plagioclases are deformed or broken, a few of the plagioclase phenocrysts show impressive zoning and polysynthetic twinning (Figure 3.24).

Some of the plagioclases in this rock samples have sieve texture, defined by a partially resorbed core (Shelley, 1993), which is overgrown by a rim containing several small, subhedral plagioclase crystals.

Phenocrysts are dominated by plagioclase, but also include 2% small, prismatic clinopyroxene (more than the sparse distribution in the Middle Eocene rock samples). Like KM 43, grains of chlorite, biotite, and opaque minerals abound in the matrix.

Sample KM 45, with angular crystal texture and ~ 25-30% glass fragments, is probably a pyroclastic rock such as crystal-vitric tuff. However, based on the major element concentrations, this rock is classified as a trachyandesite (Table 3.3). Feldspar and opaque minerals abound in the matrix of this rock.

Sample KM 48 is also porphyritic, typified by smaller broken, and in some cases bent grains of plagioclase phenocryst, but contain rounded and resorbed grains of biotite and pyroxene. The composition of the plagioclase of this mafic rock sample is highly calcic, and show alteration. This rock is more phenocryst rich than KM 45 with approximately 35%-40% modal composition.

Saussuritization (Lauri et al., 2003; Shelley, 1993), in which the An-component forms epidote, zoisite, clinozoisite, and usually calcite and sericite, is observed in these studied thin sections (KM 30, 45, and 48).

Opaque minerals such as magnetite partially or entirely replace phenocryst minerals like biotite, and constituents of the matrix of these rocks samples.

The volcaniclastic rocks, KM 31, 41, and 47, are micro-porphyrific silica rich, distinguished by abundant fine and microscopic scale fiammes, vermicular pseudo-fiammes, and sparse basic inclusions inside the felsic groundmass (Figure 3.35).

The fiamme and vermicular pseudo-fiammes, in these rock samples, are filled with quartzo-feldspathic minerals and in some cases also by plagioclase. The margins of the pseudo-fiammes have thin edges of oxidized basic glass which possibly suggest the mingling of the felsic lava with basic-intermediate magma. Opaque grains are abundantly observed as in phenocryst inclusions and within the matrix.

Km 32 is glomeroporphyritic, characterized by its vitroclastic texture and abundance of volcanic glass shard mixed with oxidized basic glass.

Base on major element concentration all Late Eocene volcaniclastic rocks of the first sequence, have felsic composition and contain rounded and resorbed grains of biotite and K-feldspar due to alteration. They all are silicified and contain secondary quartz and calcite, occurring as scattered grains, and in microveinlet which likely reflect the complex major element concentrations data obtained for these volcaniclastic rocks.



Figure 3.24. Photomicrograph showing twinned and zoned plagioclase (KM 30).

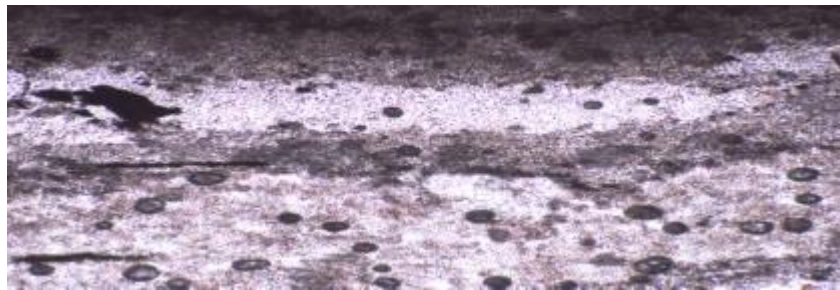


Figure 3.25. Vermicular pseudo-fiammes, filled with quartzo-feldspathic minerals. Sequence 1, sample KM 47. See Figure 3.24 for scale.

Sequence 2 (Samples KM 49, 50, 33, 34)

Sample Km 49 is highly altered (Figure 3.26), and is dominated by laths of plagioclase (~20-25% of the rock, by value), in addition to the ubiquitous grains of chlorite and calcite (CaO =11.38%, Table 3.3). Most plagioclases resorbed; however some simple twins and zoning occur. Ferromagnesian minerals are minor, less than 2% have oxidized rims, and some grains have been entirely replaced with Fe-Ti oxides (Fe_2O_3 =11.38%, TiO_2 =0.91). There are within a highly oxidized groundmass.

Sample KM 33 and 50 are micro porphyritic, but also include about 5% clinopyroxene. KM 33 is typified by coarse-grained plagioclase laths which account for approximately 25%-30% of the rock, by volume. Carbonate and chlorite minerals abound, as inclusions or replacement minerals in phenocrysts and as components of the groundmass.

Although the original shape of the olivine phenocrysts in the mafic volcanic rocks is preserved, in this sample (KM 33), olivine is altered into iddingsite (iron oxide) through a process called opacitization (Feldman, 2001, Shelley, 1993). There are also some pseudomorph (untypical form) minerals within KM 33 groundmass, formed by substitution, deposition, or alteration (Shelley, 1993) which are recognized by the residual minerals.

Sample KM 50 is also porphyritic, but dominated by smaller grain size of plagioclase laths compared to that in KM 33 and the absence of quartz. The euhedral and anhedral plagioclase grains in KM 50 contain internal oxidation rims and corroded cores (sieve texture) (Figure 3.27). Some grains in both KM 33 and 50 are sporadically sharp-edged and some have rounded and resorbed edges. Some crystals are also twinned, and some are compositionally zoned (Figure 3.28). There are small grains of chlorite, calcite, and opaque minerals in the groundmass in these two rock samples.

Sample KM 34 as a volcanoclastic rocks is particularly similar to volcanoclastic rocks of the first sequence, KM 31, 46, and 47. It contains abundant fine-scale flames, aligned with the direction of the matrix flow and filled with quartzo-feldspathic minerals.

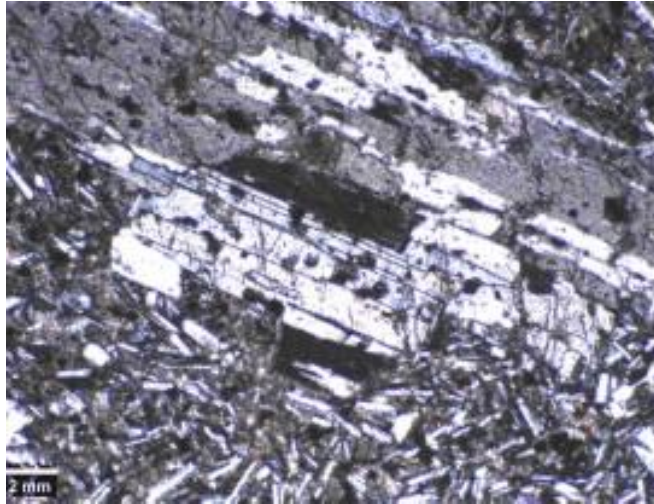


Figure 3.26. Photomicrographs showing saussuritization in the altered plagioclases in sample KM 49 of the second sequence.

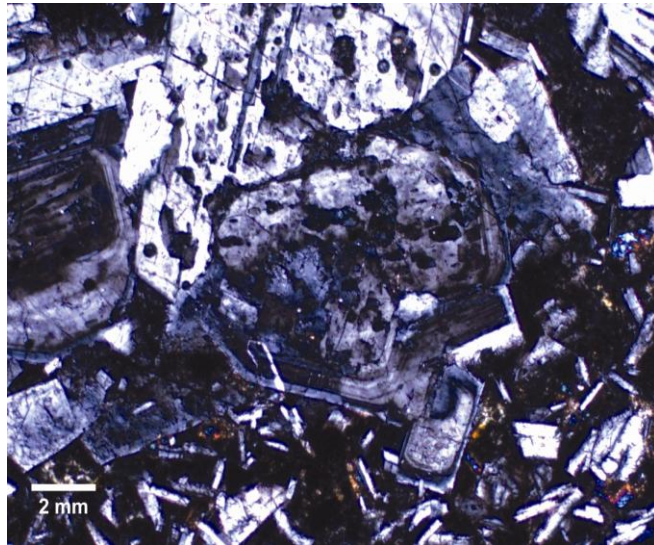


Figure 3.27. Photomicrograph showing zoning and saussuritization in plagioclase KM 50.

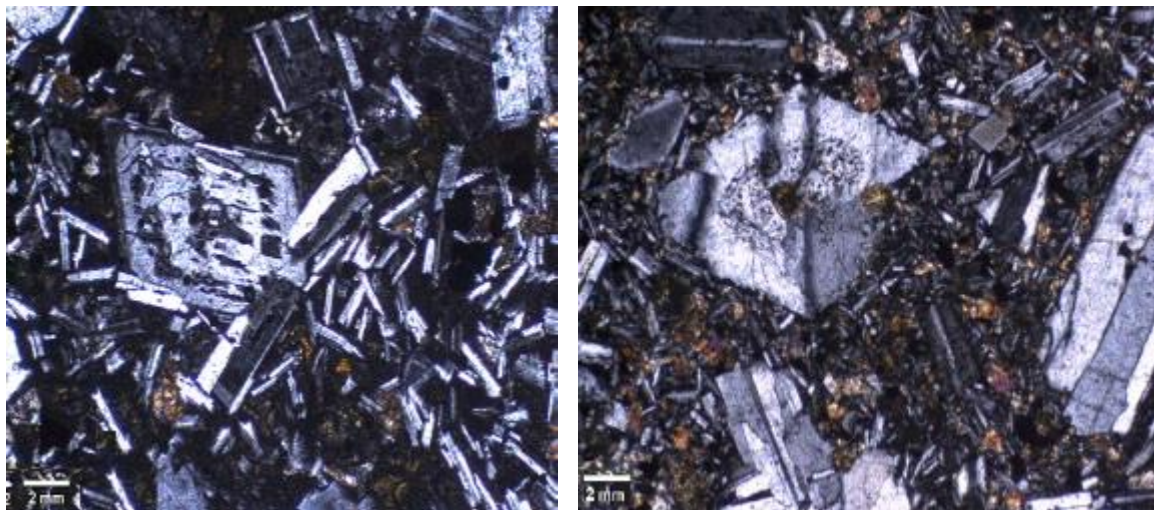


Figure 3.28. Sieve texture and zoning in plagioclase in samples KM 50 (left) and KM 49 (right).

Sequence 3 (Samples KM 35, 36, 51, 37)

The phenocryst assemblage in KM 35 is again dominated by ~ 20-30% plagioclase, and includes 1- 2% small clinopyroxene and olivine. Iron oxide minerals ($\text{Fe}_2\text{O}_3 = 10.13\%$), calcite ($\text{CaO} = 11.6\%$), and biotite ($\text{Al}_2\text{O}_3 = 19.36\%$) are abundant in the groundmass (Table 3.3). Both KM 36 and 51 show subophitic textures as plagioclase laths are enclosed by ferromagnesian minerals (e.g. pyroxene or olivine) (Shelley 1993; Verner, 2004).

The plagioclase laths are mostly oriented and accounted for approximately 30%-40% of the phenocrysts. They also contain resorbed grains of pyroxene and olivine (2-5% of the rock, by volume). These rocks also contain resorbed grains of biotite, calcite, and chlorite.

The plagioclase laths in the KM 37 show a preferred orientation with a trachytic texture, formed as the result of flow (Shelley, 1993). Groundmass is made of very fine-grained plagioclase laths. Phenocrysts account for approximately 20-30% of the rock, by volume. Most plagioclase phenocrysts are zoned and twinned, while some grains are broken. Abundant biotite and opaque minerals occur as phenocryst inclusions and in the matrix.

Sequence 4 (Samples KM 38, 41)

The coarse-grained rock sample KM 38, taken in the topmost sequence of the Late Eocene succession, is phenocryst-rich porphyry. It is dominated by coarse grained plagioclase set in the fine- to medium -grained matrix. Phenocrysts account for approximately 25-35% of the rock, by volume. Quartz inclusions are evident in plagioclase (Figure 29).

This rock also contains 2-5 % pyroxene and biotite, and secondary quartz and calcite, which occur as scattered grains, and in microveinlets (CaO= 10.8%, Table 3.3). The phenocrystic plagioclases in sample KM 41, with ~ 25-30% modal composition, are comparable to ~30% for KM 37 of the third sequence. The groundmass of this sample is silicified, replaced by secondary quartz (SiO₂= 60%, Table 3.3). The majority of plagioclases are twinned and zoned. The sieve texture is evident in this sample. Iron oxide minerals appear to have partially or completely replaced most of the olivine grains which are recognized by the remnant olivine or by its typical form (Figure 3.29).

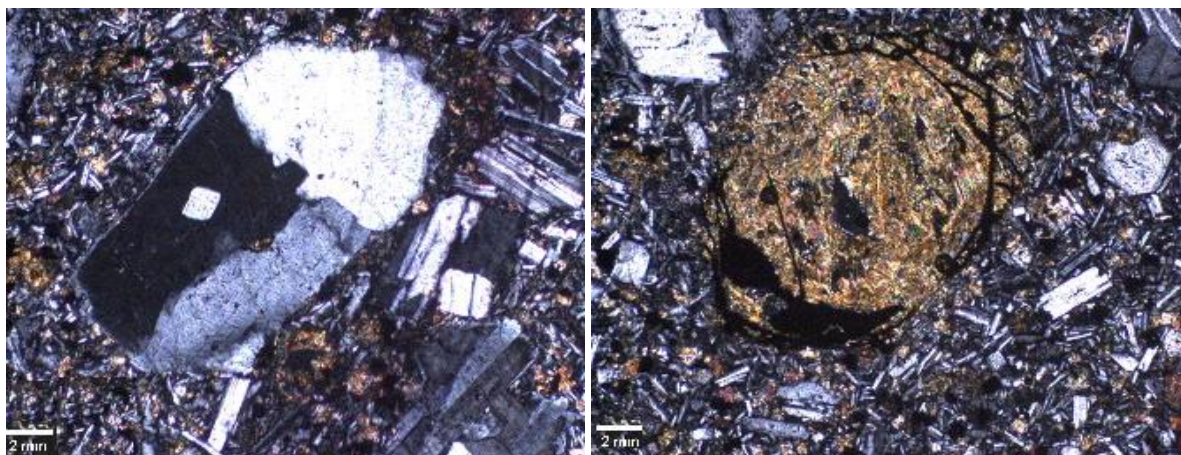


Figure 3.29. Quartz inclusions (left) and iddingsite minerals in olivine (KM 38).

Microprobe Analysis

Normal and fairly oscillatory zoning in plagioclase were revealed during microprobe analysis on four thin sections (Table 3.2). The plagioclase phenocrysts in the studied thin sections (KM 30, 36, 38, and 42) are dominated by anorthite and bytownite; calcium-rich members of the plagioclase family. They also displayed normal compositional zoning (i.e., anorthite rich core to albite rich rim) from $An_{98.3} Ab_{1.68}$ to $An_{71.82} Ab_{28.18}$.

Orthopyroxene presents a constant range in (Fe, Mg) replacement between pure enstatite ($Mg_2Si_2O_6$) and pure ferrosilite ($Fe_2Si_2O_6$). Based on the microprobe analysis of samples (KM 30, 36, 38, and 42), these volcanic rocks contain small phenocrysts of clinopyroxene (augite) and minor orthopyroxene (hypersthene).

Average augite composition is $En_{44}Fs_{16}Wo_{40}$, and hypersthene composition is ($En_{44}Fs_{53}Wo_3$). As shown in Figure 3.30, the core of the zoned plagioclases is probably not homogeneous in composition.

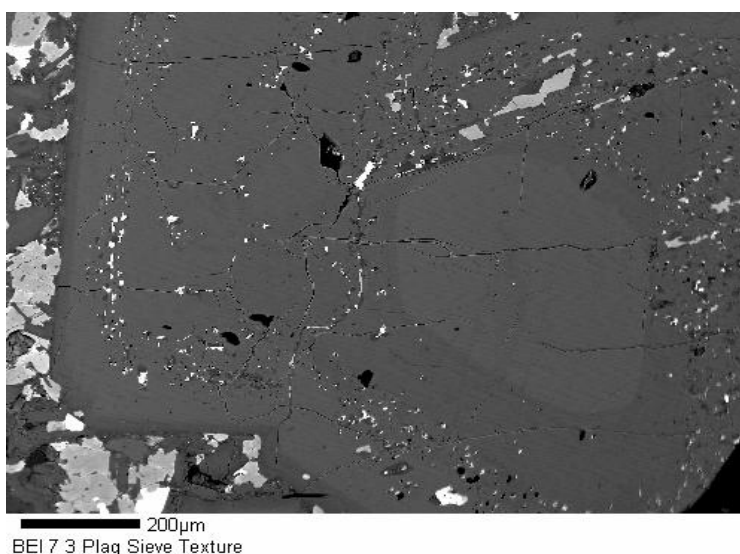


Figure 3.30. Microprobe images showing different compositional zoning in the core of the plagioclase (KM 38).

Major Element Analysis

Major element concentrations are commonly used to classify igneous rocks such as basalt and andesite, and, if rocks are not altered, can supply significant clues for the geochemical evolution and petrogenesis of these rocks.

There are various geochemical diagrams for the classification and identification of volcanic rocks based on the major element concentrations. The Total Alkali-Silica (TAS) diagram (Figure 3.31), an International Union of Geological Sciences (IUGS) classification scheme, is one such diagram which is commonly used by petrologists.

The TAS diagram assists in characterizing the various types of volcanic rocks (Le Bas et al, 1986). Due to the significance of the alkalis (Na_2O , K_2O) and silica (SiO_2) in determining the precise mineralogy of unaltered rocks, the TAS diagram uses the combined alkali content (Na_2O wt% plus K_2O wt%) against the silica content (SiO_2 wt%) (Le Bas et al., 1986; Rollinson, 1993). Despite the acceptance of this method in the scientific community, their application of the TAS diagrams to this investigation was limited due to the varying degrees of alteration of most studied rocks.

In order to reveal the temporal relationship between the degrees of alteration of the rock samples, taken in different stratigraphic positions, loss on ignition (LOI) was plotted versus silica in Figure 3.33.

As shown in Figure 3.31, the TAS diagram has specific fields corresponding to individual rock types. Each type of volcanic rock is plotted in a particular demarcated field on the diagram, and is classified and named on the basis of its texture, and chemical characteristics (Rollinson, 1993).

Studies of the chemical composition of numerous specific volcanic rocks have delineated the compositional boundaries of the fields of the TAS diagram, which basically signify the dividing lines of these rock types based on the major element composition of previously published.

Consequently, the boundaries are rather random, and points on either side of a given field boundary may actually represent the same rock type (Rollinson, 1993). Fresh igneous rocks are commonly subdivided based on the silica content into: felsic or acidic (> 66 wt% SiO_2), intermediate (52 - 66 wt% SiO_2), mafic or basic (45 - 52 wt% SiO_2), and ultramafic (< 45 wt% SiO_2) (Winter, 2001; Le Maitre, 2002).

The major element concentrations of the volcanic rocks in the study area, obtained at the GSU XRF geochemistry lab, are given in wt% in Table 3.3a, b. Rocks also are specifically named and identified using the common Total Alkali-Silica diagram as shown in Figure 3.31. The TAS diagram is also divided into alkaline and subalkaline fields by a solid line (Figure 3.31). Subalkaline rocks are commonly subdivided into calc-alkaline and tholeiitic series based on the iron or aluminum oxide content. Calc-alkaline rocks are relatively poor in iron, and contain 16% - 20% Al_2O_3 .

The calc-alkaline groups commonly represent subduction zone; however, they are also found in volcanic arcs on the continental crust (Baker, 1983). In contrast, the iron rich tholeiitic rocks which contain 12% - 16% Al_2O_3 , are routinely characterized by mafic igneous rocks (e.g. basalt and gabbro) found along oceanic ridges or on the ocean floor (Philpotts, 1989). Furthermore, in order to divide the sub-alkaline rocks into high-K, medium-K, and low-K (tholeiitic) groups, an additional classification, based merely on the K_2O wt % concentration, is used as is shown in Figure 3.32 (Le Maitre et al., 1989; Rollinson, 1993).

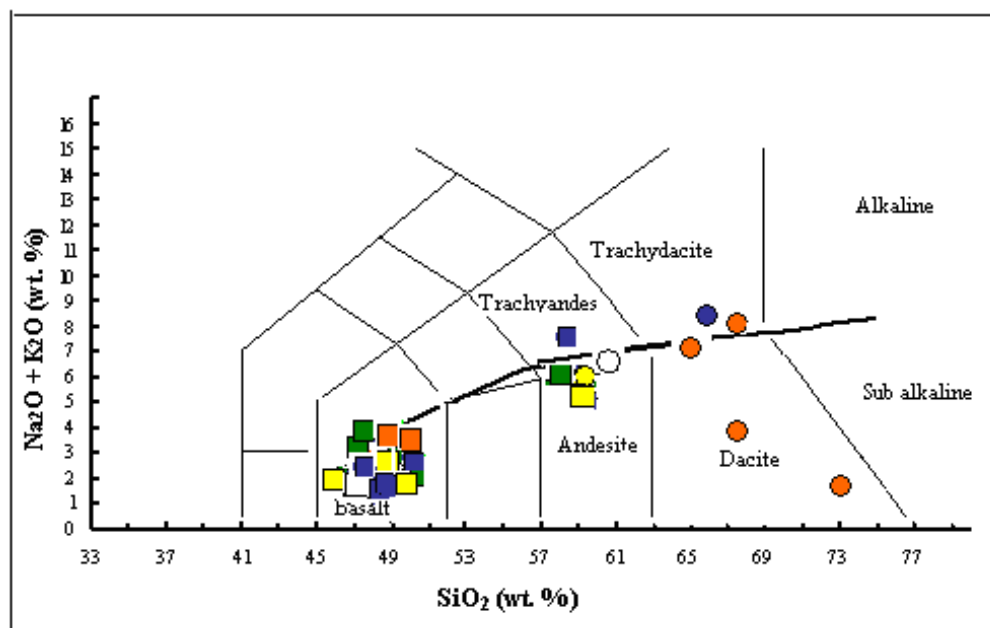


Figure 3.31: Total Alkali-Silica diagram modified from Le Bas (1986) and La Martin et al., (1989). \blacksquare E^v, E^{gt} \blacksquare E^{ab} \bullet E^{ig1} \blacksquare E^a \bullet E^{ig2} \blacksquare E^{hy} \bullet E^{ig3} \square E^b \circ E^{ig4} (geology.about.com/od/more_igrocks/ig/igroxdiagrams/TASvolcanic.htm)

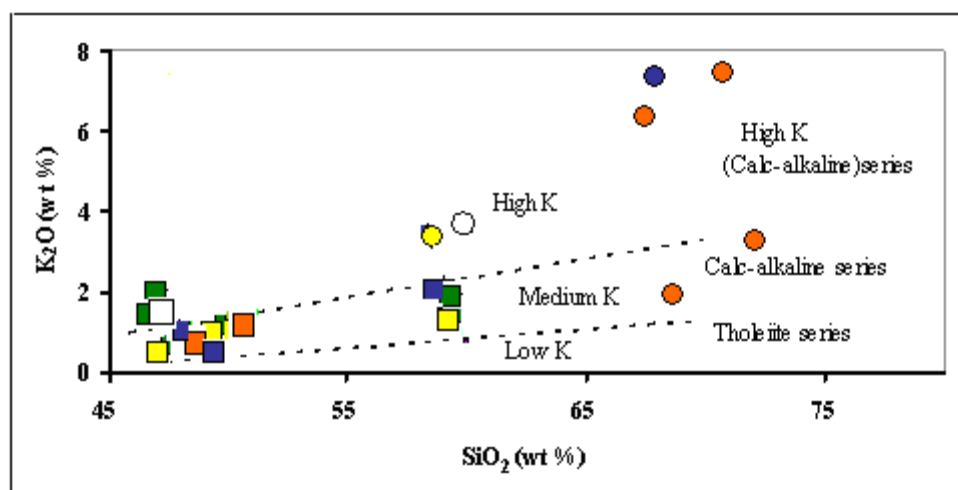


Figure 3.32: Sub-alkalic subdivisions based on potassium composition. High-K, Middle-K, and Low-K fields separated by dashed lines. Fields from LeMaitre, 1989, and Rollinson, 1993.

\blacksquare E^v, E^{gt} \blacksquare E^{ab} \bullet E^{ig1} \blacksquare E^a \bullet E^{ig2} \blacksquare E^{hy} \bullet E^{ig3} \square E^b \circ E^{ig4}

The Harker diagram (Figure 3.34), the oldest bivariate type of diagram (1909), plots oxides of elements against SiO_2 . Due to the abundance of silica (SiO_2) in igneous rocks, and its significant variation in rock compositions, bivariate diagrams use silica concentrations as a plotting feature (Rollinson, 1993; Winter, 2001). However, some researchers (e.g., Cox et al., 1979; Rollinson, 1993) have argued that, due to the failure of increasing the silica concentration in the residual liquid of former melts, negative inclination, and false correlation in some patterns, applying the SiO_2 as an evolutionary index might be less reliable.

The bivariate plots of Figure 3.34 present the major elements plotted against silica concentrations (as wt %) to reveal any evolutionary trends. concentrations (as wt %) to reveal any evolutionary trends.

Petrologic relationships, especially for the mafic (basalt) and ultramafic rocks, can best be detected by applying a bivariate plot of MgO vs. all other major oxides rather than using SiO_2 (Wright, 1974; Rollinson, 1993; Winter, 2001). Since magnesium is very compatible, it preferentially partitions into minerals crystallized (e.g. olivine) in the early stages of crystallization and it is depleted in the residual melt.

Therefore, magnesium decreases in abundance in the melt as crystallization proceeds. Conversely, Mg will remain behind, in the rock, as melt is primarily formed through partial melting; as a result, with decrease in Mg content and increase in silica content in an evolving cogenetic series, rocks produced through fractional crystallization are originally Mg-rich and silica-poor (Winter, 2001).

Figure 3.35 displays plots of the major oxides against MgO. The major oxides have also been plotted against the magnesium number (Figure 3.36) as a degree of fractionation during the evolution of magma.

The formula used for calculating the Mg number is as follows: $\text{Mg number} = 100 \times (\text{moles Mg} / (\text{moles Mg} + \text{moles FeO}^t))$ which shows the relationship of magnesium to iron concentrations as an index of crystal fractionation (Rollinson, 1993; Wright, 1974).

Magnetite commonly affects and reduces the Mg/Fe ratio than the predictable Mg/Fe ratio in an evolving crystal-liquid series. Therefore, if magnetite would be one of the crystallizing phases, as in some of the studied rock samples, the magnesium number cannot potentially be a realistic crystallization index (Cox et al., 1979). Higher degrees of alteration are evident in the older sequences compared to the younger ones.

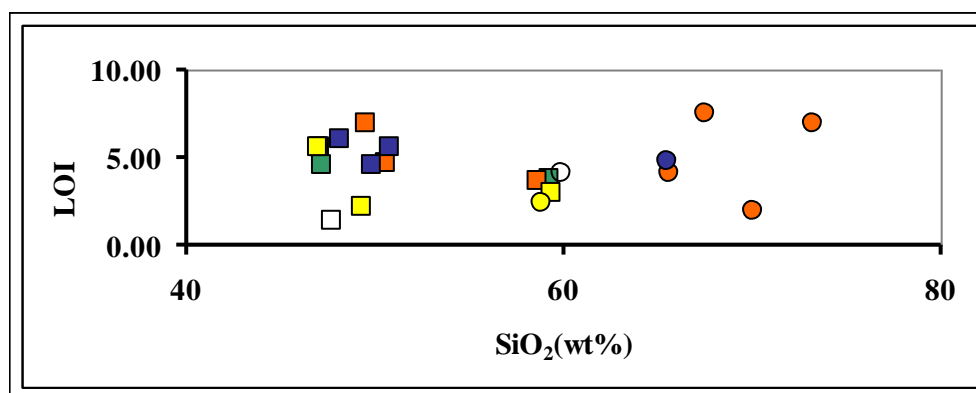
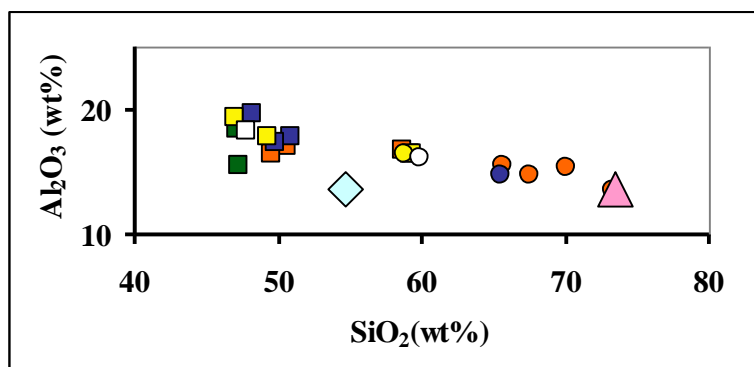
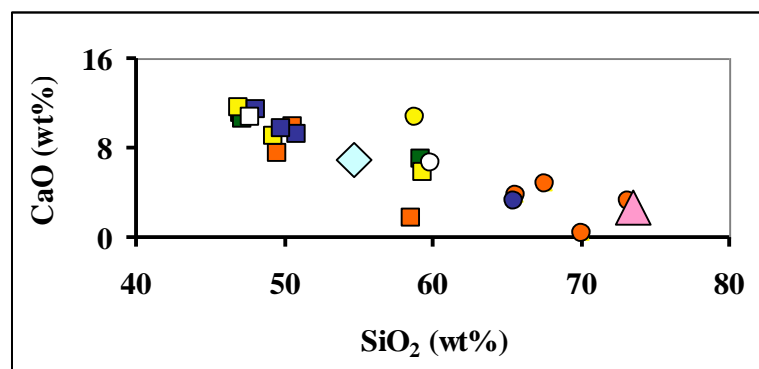
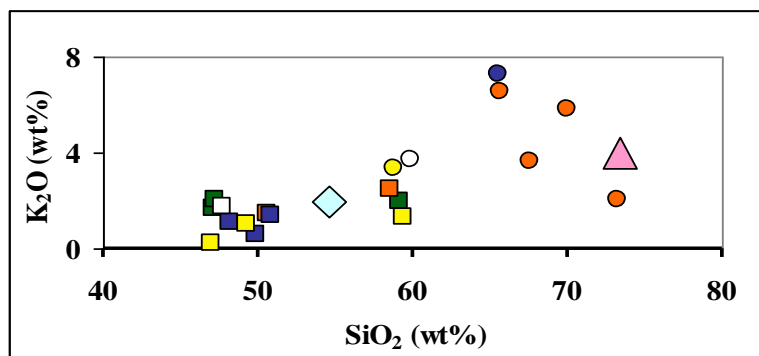
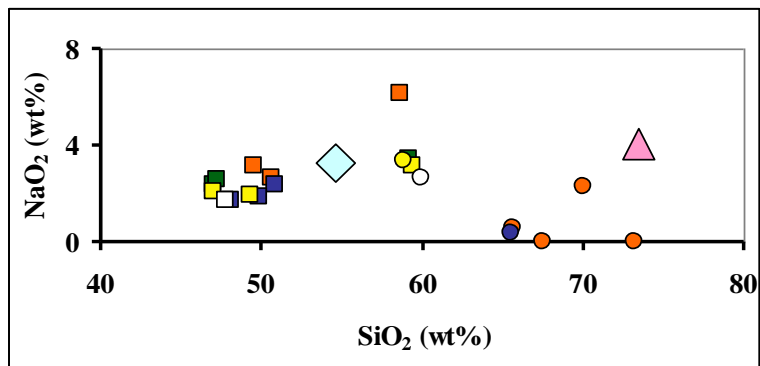


Figure 3.33. Loss on ignition (LOI %) vs. SiO_2 for all volcanic rocks. It is showing most of the rock samples have loss on ignition (LOI) >4 wt%. Middle Eocene E^v , E^{gt} Sequence 1: E^{ab} E^{ig1} Sequence 2: E^a E^{ig2} Sequence 3: E^{hy} E^{ig3} Sequence 4: E^b E^{ig4}

XRF-generated USGS Reference Samples, BCR-1 (basalt) and RGM-1 (rhyolite) (Geostandards, 1984), are included for comparison in the following bivariate plots. Disregarding the high scatter in the distribution of some major oxides between rock samples in each sequence due to alteration, the rock samples follow the same pattern like the pattern between the BCR-1 basalt and RGM-1 rhyolite in the most Harker diagrams.



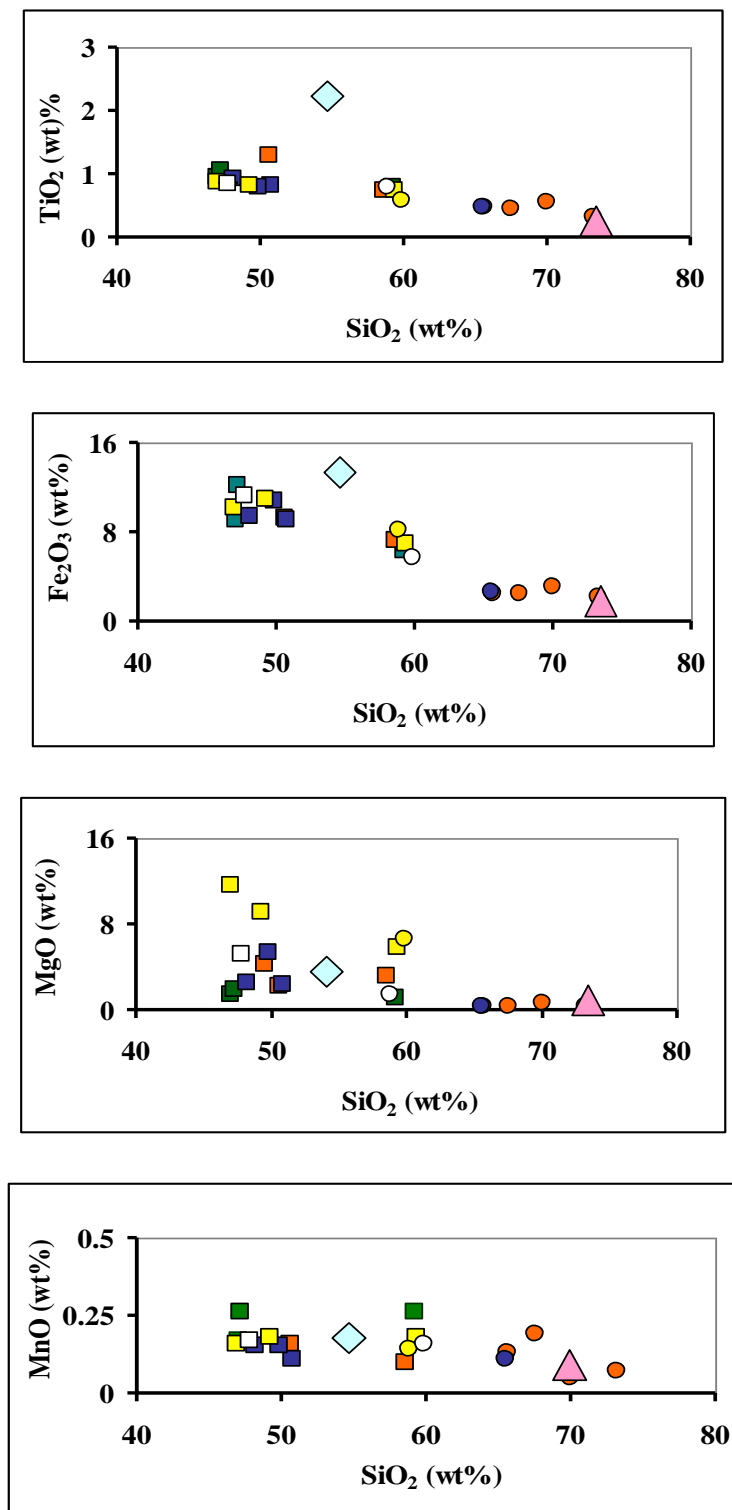
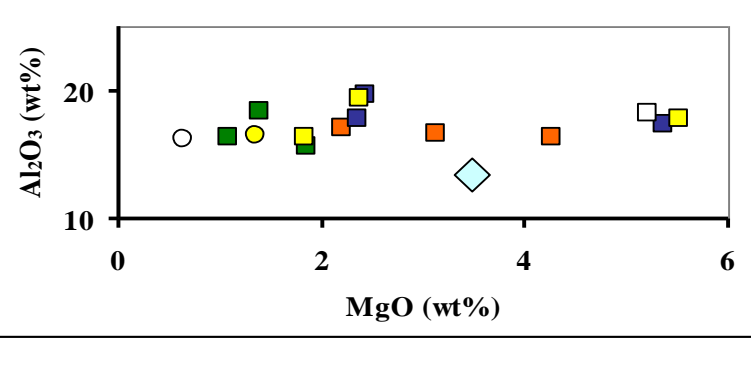
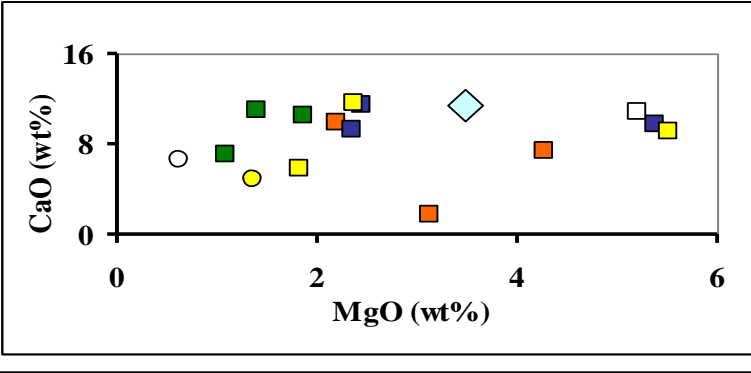
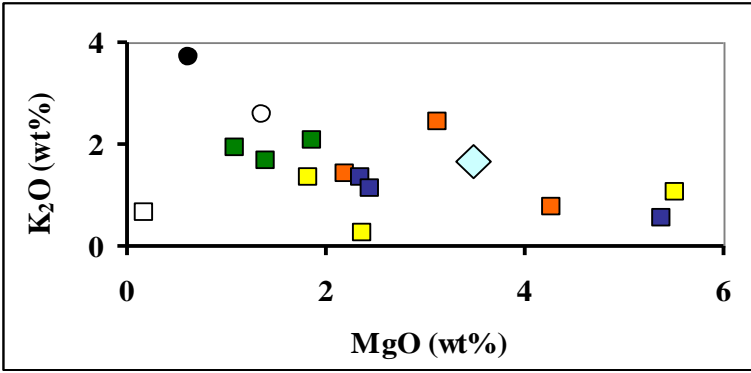
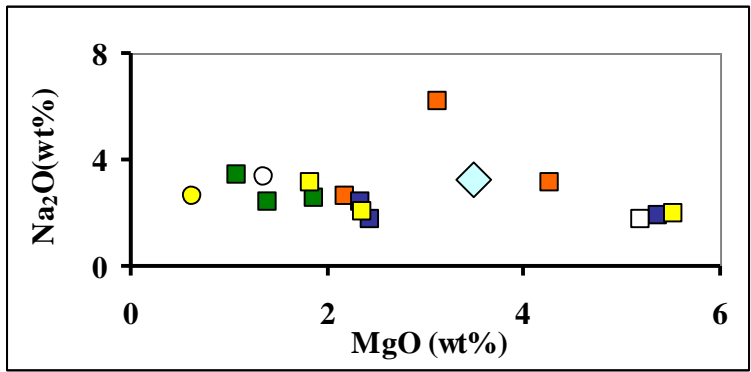


Figure 3.34. Major elements vs. SiO₂ (wt %). Middle Eocene E^v , E^{gt} Sequence 1: E^{ab} Sequence 2: E^a Sequence 3: E^{hy} E^{ig3} Sequence 4: E^b E^{ig4} USGS Reference Samples: \diamond BCR-1 (basalt) \triangle RGM-1 (rhyolite) (Geostandards, 1984).



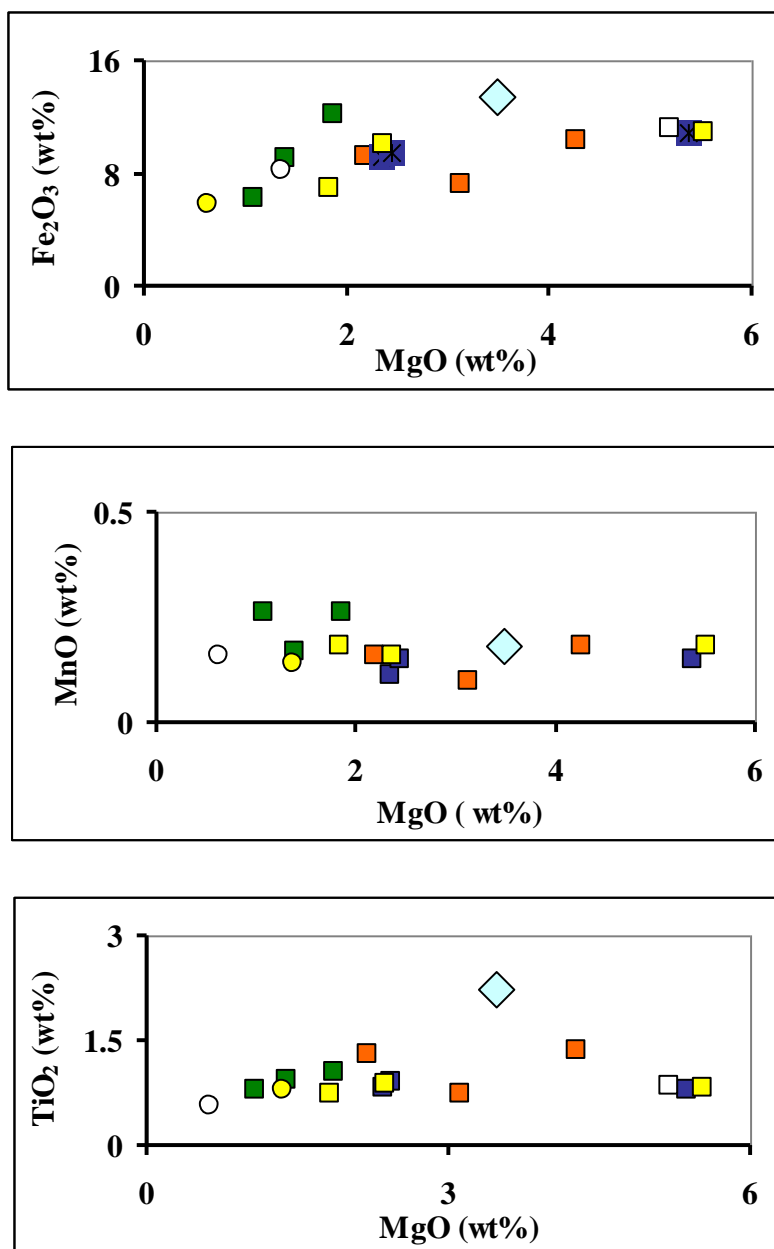


Figure 3.35. Major elements vs. MgO (wt %). Middle Eocene E^V , E^{gt} Sequence 1: E^a Sequence 2: E^a Sequence 3: E^{hy} E^{ig3} Sequence 4: E^b E^{ig4}
 USGS Reference Samples: \diamond BCR-1 (basalt) \triangle RGM-1 (rhyolite) (Geostandards, 1984).

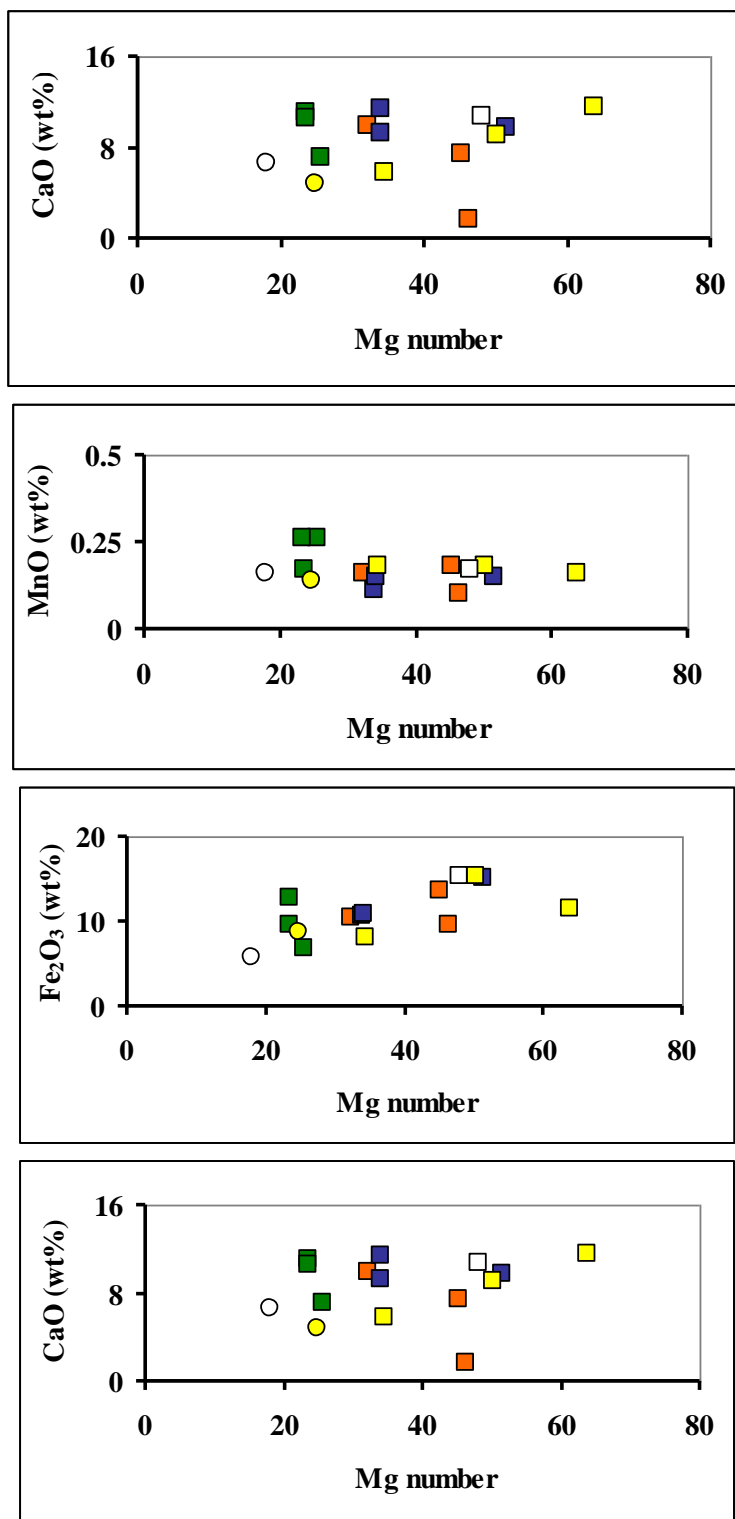


Figure 3.36. Major elements vs. Mg number. Middle Eocene E^v, E^{gt} Sequence 1: E^{ab}, E^{ig1} Sequence 2: E^a Sequence 3: E^{hy}, E^{ig3} Sequence 4: E^b, E^{ig4}

Table 3.1. Microprobe data of the four hyaloclastic rocks in the study area, obtained in the University of Georgia (UGA).

wt. %	E^{ab}						E^{hy}		E^b						E^{ig4}		Standard	
	KM 30						KM 36		KM 38						KM 42		**A	***B
	Pyr		Plag				Plag	Pyr	Plg					Plg		Pyn	Plg	
	5.10	5.5	5.4 rim	5.6 rim	5.7 core	5.7 rim	6.2 core	6.2 rim	7.11	7.3	7.2core	7.2 rim	7.4 core	7.4 rim	8.7 core	8.7 rim		
SiO₂	51.58	50.86	50.67	51.15	50.73	52.13	47.54	50.96	54.79	48.99	44.49	46.45	45.20	44.83	45.47	47.53	40.23	51.53
Al₂O₃	1.98	2.33	31.27	30.85	30.71	29.91	32.75	30.44	0.11	5.61	35.25	33.64	34.42	34.65	34.65	32.95	0.02	30.62
FeO	10.26	9.31	0.37	0.47	0.33	0.69	0.90	0.89	29.73	10.13	0.52	0.76	0.62	0.59	0.61	0.72	16.07	0.56
CaO	19.40	20.87	14.34	13.98	15.32	13.13	16.85	14.10	1.33	19.78	19.09	17.55	18.72	18.84	18.30	16.83	0.02	13.62
MgO	15.50	15.50	0.01	Nd	0.02	0.10	0.05	0.05	13.84	14.39	0.00	0.11	0.04	0.05	*Nd	0.09	43.22	0.13
Na₂O	0.18	0.16	3.11	0.16	0.14	0.20	1.76	3.18	0.06	*Nd	*Nd	*Nd	0.89	0.92	0.94	1.79	*Nd	3.31
K₂O	0.18	0.01	0.12	3.33	2.58	3.78	0.12	0.21	*Nd	*Nd	*Nd	*Nd	0.04	0.03	0.04	0.04	*Nd	13.62
TiO₂	0.61	0.67	0.03	0.02	0.06	*Nd	0.03	0.08	0.05	0.79	0.01	0.07	0.02	0.00	*Nd	*Nd	0.01	0.08
MnO	0.45	0.29	0.04	*Nd	Nd	*Nd	0.05	*Nd	13.84	0.27	0.03	*Nd	0.04	*Nd	0.04	0.01	0.43	*Nd
BaO	*Nd	*Nd	*Nd	*Nd	*Nd	*Nd	*Nd	*Nd	*Nd	*Nd	*Nd	0.01	0.02	0.09	*Nd	*Nd	*Nd	0.02

*Nd: Not detected **A: Olivine 5 Stan U of Ore ***B: Labradorite stan, USNM

Table 3.2. Major element concentrations (wt%) of volcanic and volcanoclastic rocks in the study area, obtained in the Georgia State University's XRF laboratory.

Middle Eocene				Late Eocene										
Four alternating sequences of hyaloclastite& ignimbrite														
Sequence 1							Sequence 2							
Hyaloclastite			Hyaloclastite				Ignimbrite				Hyaloclastite			Ignimbrite
E ^v E ^{gt}			E ^{ab}				E ^{ig1}				E ^a		E st	E ^{ig2}
* wt.%	KM 42	KM 44	KM 43	KM 30	KM 48	KM 45	KM 47	KM 46	KM 31	KM 32	KM 33	KM 50	KM49	KM 32
SiO₂	48.16	47.24	59.21	50.62	49.52	58.60	65.66	67.55	70.05	72.13	50.81	49.82	48.16	72.13
Al₂O₃	18.38	15.56	16.38	17.11	16.40	16.70	15.48	14.70	15.36	13.54	17.73	17.35	19.60	13.54
Fe₂O₃Total	9.04	12.12	6.30	9.18	10.33	7.23	2.39	2.43	3.09	2.14	9.15	10.84	9.43	2.14
CaO	10.99	10.52	7.03	9.87	7.42	1.68	3.72	4.78	0.30	3.27	9.24	9.71	11.38	3.27
MgO	1.39	1.86	1.08	2.19	4.27	3.12	0.33	0.36	0.57	0.25	2.35	5.37	2.44	0.25
Na₂O	2.42	2.57	3.43	2.64	3.12	6.17	0.58	**Nd	2.28	*Nd	2.38	1.86	1.75	*Nd
K₂O	1.70	2.06	1.94	1.43	0.76	2.44	6.51	3.64	5.85	2.03	1.36	0.55	1.11	2.03
TiO₂	0.96	1.06	0.78	1.29	1.36	0.74	0.48	0.46	0.54	0.32	0.82	0.79	0.91	0.32
MnO	0.17	0.26	0.26	0.16	0.18	0.10	0.13	0.19	0.05	0.07	0.11	0.15	0.15	0.07
P₂O₅	0.25	0.26	0.31	0.61	0.40	0.20	0.70	0.07	0.13	0.07	0.24	0.17	0.20	0.07
LOI	5.55	4.53	3.70	4.64	6.89	3.65	4.12	7.52	1.97	6.89	5.61	4.57	6.03	6.89
Total	99.01	98.04	100.42	99.74	100.65	100.63	100.10	100.71	100.19	100.70	99.80	101.18	101.16	99.54

*See Table 3.3b for reproducibility.

**Nd: Not detected

Trace Elements

Trace elements are particularly efficient in provenance studies of igneous rocks since they occur in a much larger range of concentrations than major elements. Trace elements are also susceptible to pressure, temperature, composition, and oxygen activity conditions. However, the changes in their concentration do not affect the stability of any phase of the system because the concentration in trace elements is sufficiently low (Hanson, 1980). These attributes make trace element concentration data more essential than major element concentration data to provenance studies, and determine and understand the relationship between various rock groups (Hanson, 1980; Hanson and Langmuir, 1978).

As mentioned before (chapter 2), the fourteen naturally occurring lanthanide elements, collectively known as the rare earth elements (REE), behave similarly as a homogeneous series since they all have smoothly or gradually varying chemical and physical properties (Hanson, 1980; Winter, 2001).

The REE are significantly insoluble in seawater, with residence times of 50-600 years. They are more stable or resistant to alteration and weathering processes (Piper, 1974). Through the general processes (e.g., sedimentary, diagenetic and metamorphic), the REE are mostly immobile due to their low solubility (Awwiller, 1994; Bierlein, 1995; McLennan, 1989; Taylor et al., 1986), excluding sediments with more than 5% P₂O₅ (Kidder et al., 2003).

These qualities typically make REE concentration data significant to petrogenetic studies and assessment of post-depositional alteration. Since the REE have similar properties (e.g., similarities in their 3+ oxidation state and orderly electron (f-shell) orbital filling), they are not frequently fractionated relating to each other.

The majority of the rare earth elements are chemically trivalent, with minor variation in the ionic size. However, europium (Eu) also has a valence of 2^+ and cerium (Ce) forms compounds with a valence of 4^+ during weathering or hydrothermal alteration (oxidizing conditions) (Hanson, 1980). Because the REE have similar properties, it is difficult to divide or even differentiate them from each other. With the use of isotope dilution (ID-ICP-MS) methods, separation of an individual rare earth element can be accomplished with great ease and precision.

The REE are essentially classified into three groups: the light rare earth elements (LREE), middle rare earth elements (MREE), and heavy rare earth elements (HREE). The LREE are the largest ion elements, with lower atomic numbers; conversely, the HREE are the smallest ion elements with highest atomic numbers.

Table 3.4 shows a list of the REE, their symbols, atomic numbers, and eight-fold ionic radii. REE concentrations are typically plotted, as base 10 log parts per million values (e.g., Chondrite), from light (lanthanum) to heavy (lutetium) elements along the x-axis.

In the REE series, the even atomic-numbered elements such as cerium (Ce), neodymium (Nd), and samarium (Sm), are more abundant than the adjacent odd-numbered elements. The even atomic-numbered, with even number of protons, are low neutron-capture, cross-section elements. Thus, they are not able to capture another neutron and transform into the next-higher element during neutron-flux events.

This phenomenon is called “Oddo-Harkins” effect, and causes the jagged patterns in the REE series. Concentrations are normalized to chondritic abundances to eliminate the Oddo-Harkins effect (Hanson, 1980; Staunton, 2004).

Table 3.3. Characteristics of the rare earth elements (REE).

Name	Symbol	Atomic number	Ionic radius for eight-fold coordination (Angstroms)*	Element	Leedey chondrite values**
Lanthanum	La	57	1.160	La	0.315
Cerium	Ce	58	1.143	Ce	0.813
Praseodymium	Pr	59	1.126	Pr	
Neodymium	Nd	60	1.109	Nd	0.597
Promethium	Pm	61	not naturally occurring	Pm	
Samarium	Sm	62	1.079	Sm	0.192
Europium	Eu	63	1.066	Eu	0.0722
	Eu²⁺		1.250		
Gadolinium	Gd	64	1.053	Gd	0.259
Terbium	Tb	65	1.040	Tb	
Dysprosium	Dy	66	1.027	Dy	0.325
Holmium	Ho	67	1.015	Ho	
Erbium	Er	68	1.004	Er	0.213
Thulium	Tm	69	0.994	Tm	
Ytterbium	Yb	70	0.985	Yb	0.208
Lutetium	Lu	71	0.977	Lu	0.0323

* All elements are described as 3⁺ ions except Eu. From Shannon (1976). ** Leedey Chondrite values (from Masuda et al, 1973, in Hanson, 1980), used to normalize REE abundances.

Rock samples are commonly evaluated and correlated by plotting the patterns of the REE concentrations. Interpretation and comparison of the REE patterns provide significant geochemical and geological clues for the tectonic and magmatic evolution, and also can be used to determine the petrogenetic relationships between the rocks (Hanson, 1980). Because chondrites are supposed to reveal the original (unfractionated) primitive (primordial) earth, the normalized patterns of the REE abundances reveal geochemical evolutionary changes of rock samples compared to the primitive earth rocks (Hanson, 1976; Hanson, 1980; Rollinson, 1993).

The Leedey chondrite abundances (Masuda et al., 1973, as reported in Hanson, 1980) are used for normalization in this thesis project to obtain the smooth REE patterns (see Table 3.4 for the values).

Variations or comparisons among samples are perceived based on the REE patterns (Hanson, 1976; Hanson, 1980; Walsh et al., 1997). Enrichments and/or depletions in the REE elements, or series of elements, are interpretive.

Fourteen out of the twenty four samples collected in the field for the REE analyses were analyzed both at the Georgia State University laser ICPMS Lab and the Mineral Services SGS (commercial laboratory).

Chondrite-normalized values of the rare earth elements, conducted in the Laser-ICP Mass Spectrometry Laboratory of Georgia State University, are displayed in Table 3.5.

Rare earth and other trace element concentrations, obtained from the commercial laboratory (Mineral Services SGS), are displayed, in parts per million (ppm), for all the analyzed samples in Table 3.6. Figures 3.37-3.39 display the REE patterns of the Middle and four sequences of the Late Eocene volcanic and volcanoclastic rocks, except those of breccia (KM 39) and tuff (KM 40).

Chondrite-normalized multi-element plots indicate enrichment of the Eocene Kharchin-Bijgerd area volcanic rocks, characterized with variable ratios of La_N/Yb_N (2.31-9.32) and Nb/Sm (0.19-2.70).

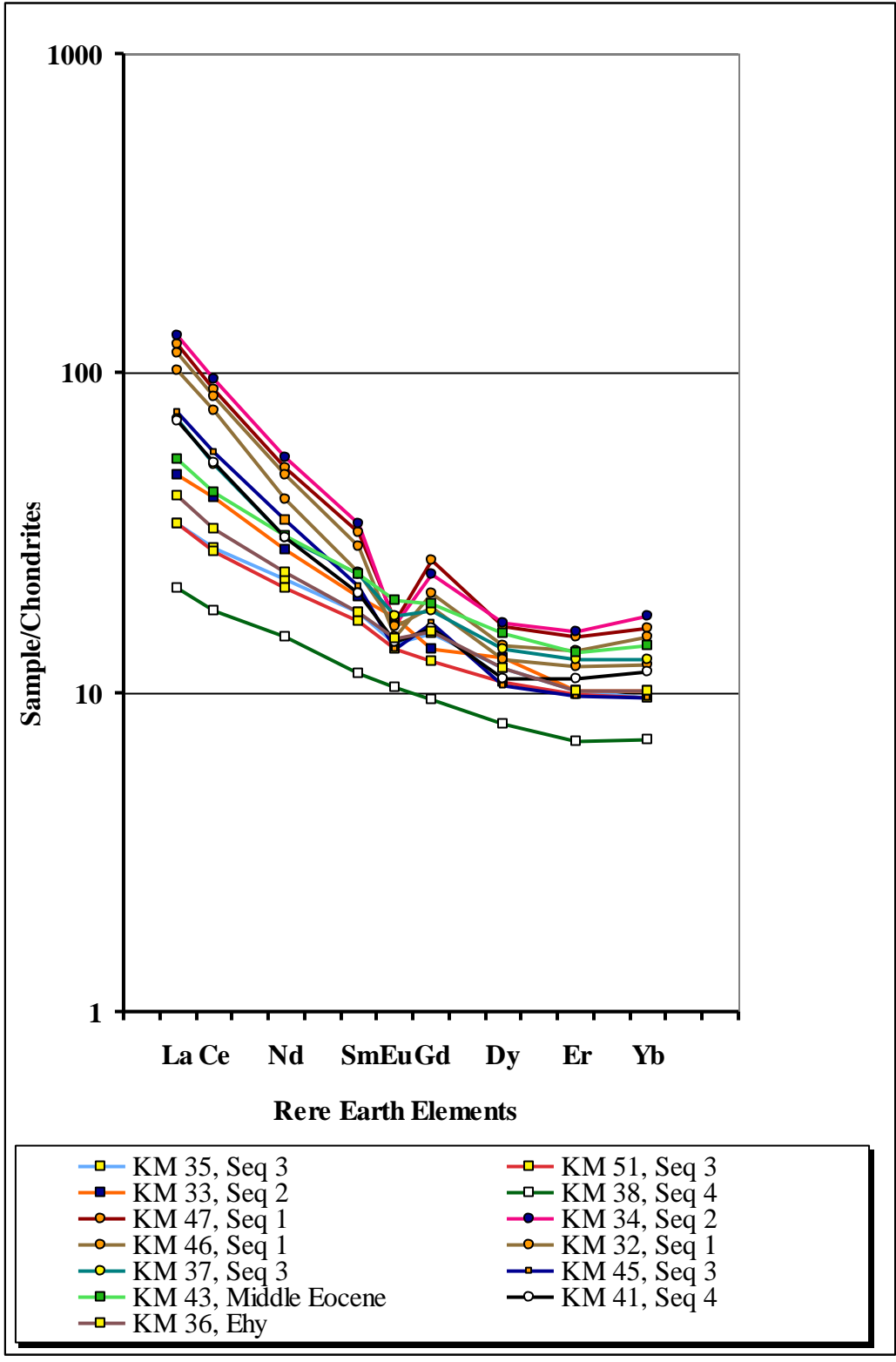


Figure 3.37. The REE patterns of the collected rock samples of the Middle and Late Eocene volcanic and volcanoclastic rocks in the study area.

The REE patterns for the rocks of the study area (Figure 3.37) show an higher enrichment of the LREE concentrations (100x chondrite) compared to the HREE (10x chondrite).

As expected, the ignimbrites have more enriched REE concentrations compared to those in the hyaloclastites on the chondrite-normalized trace element distribution diagram (Figure 3.38).

The ignimbrites are enriched in the LREE (100x chondrite), and have almost flat HREE (10x chondrite) patterns on chondrite-normalized diagrams, characterized with $5.64 < (La/Yb)_N < 9.32$ and a distinctive negative Eu anomaly ($Eu/Eu^* = 0.54-0.69$) due to plagioclase fractionation.

Notice that a flat line pattern at the normalized value of 1, on chondrite-normalized plots, indicates that the REE concentrations have not experienced any geochemical evolution.

Temporal and spatial differences or similarities among the rocks are apparent in Figures 3.40 to 3.46, which display the REE patterns of each sequence, in different stratigraphic levels, from the older (Middle Eocene) to the younger (sequence 4 of the Upper Eocene succession).

The REE patterns of different rock samples from a single unit highlight the homogeneity of the hyaloclastic rocks in the volcanic sequence (Figures 3.40-3.46).

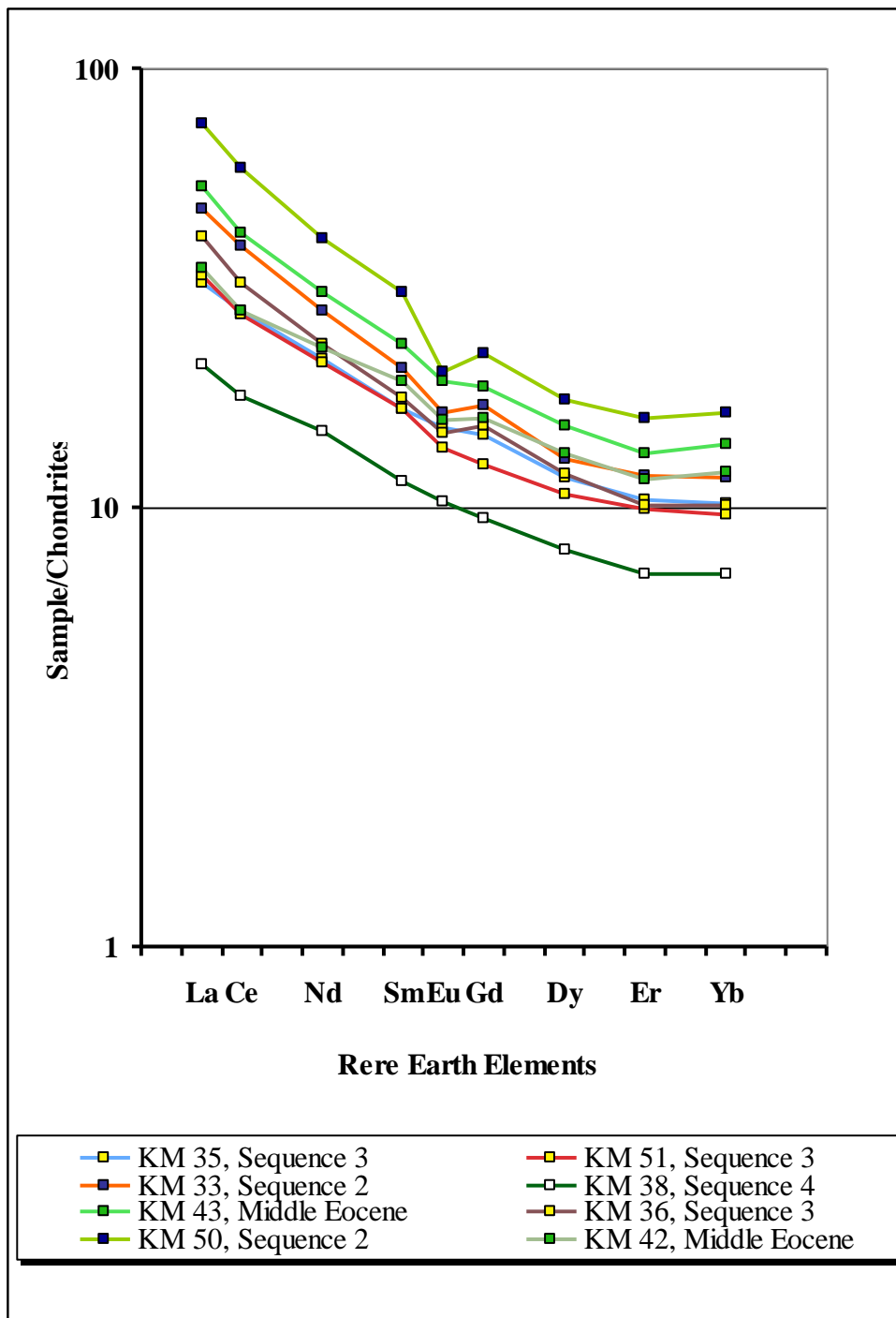


Figure 3.38. The REE patterns for some selected hyaloclastic rock samples in the Bijgerd-Kuh e Kharchin area.

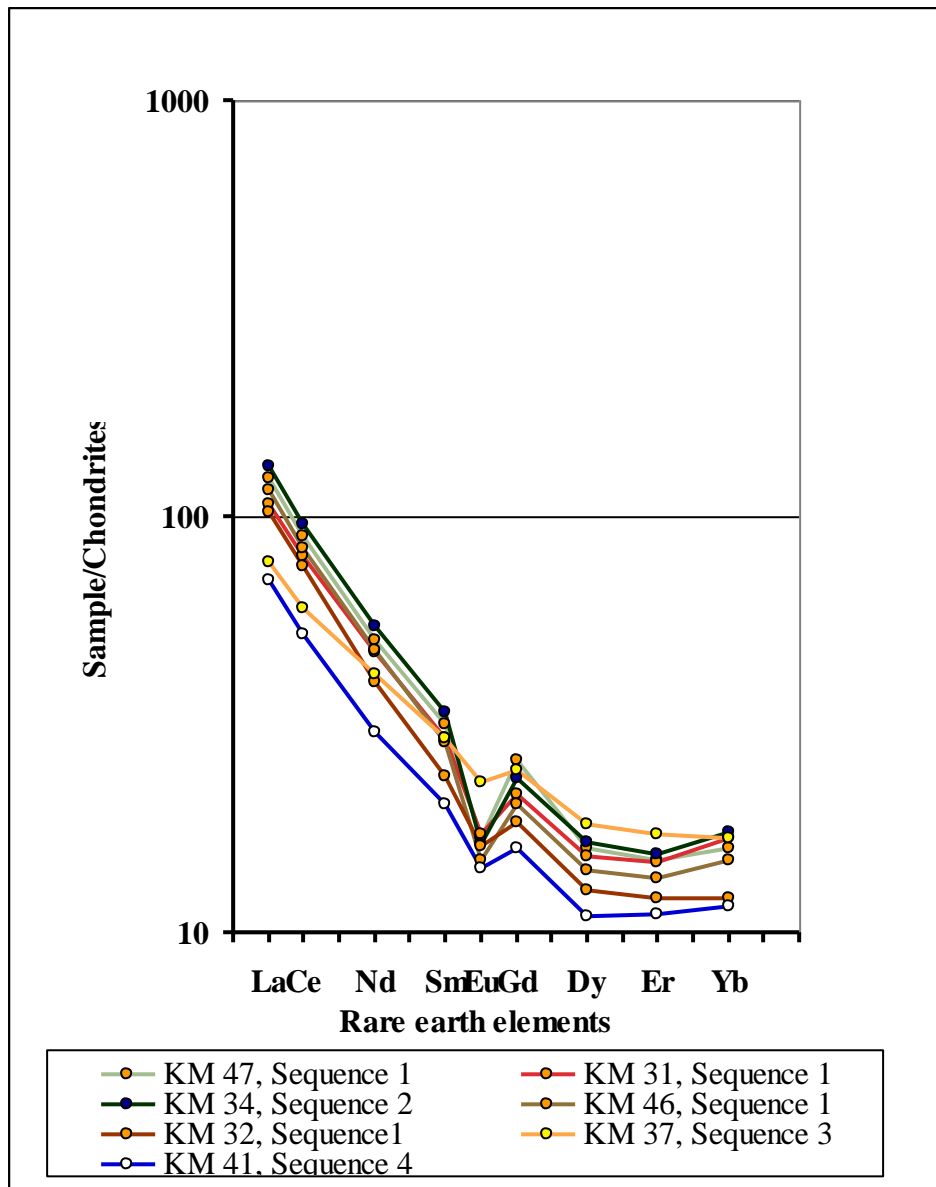


Figure 3.39. The REE patterns for the volcaniclastic (felsic) rocks in the study area.

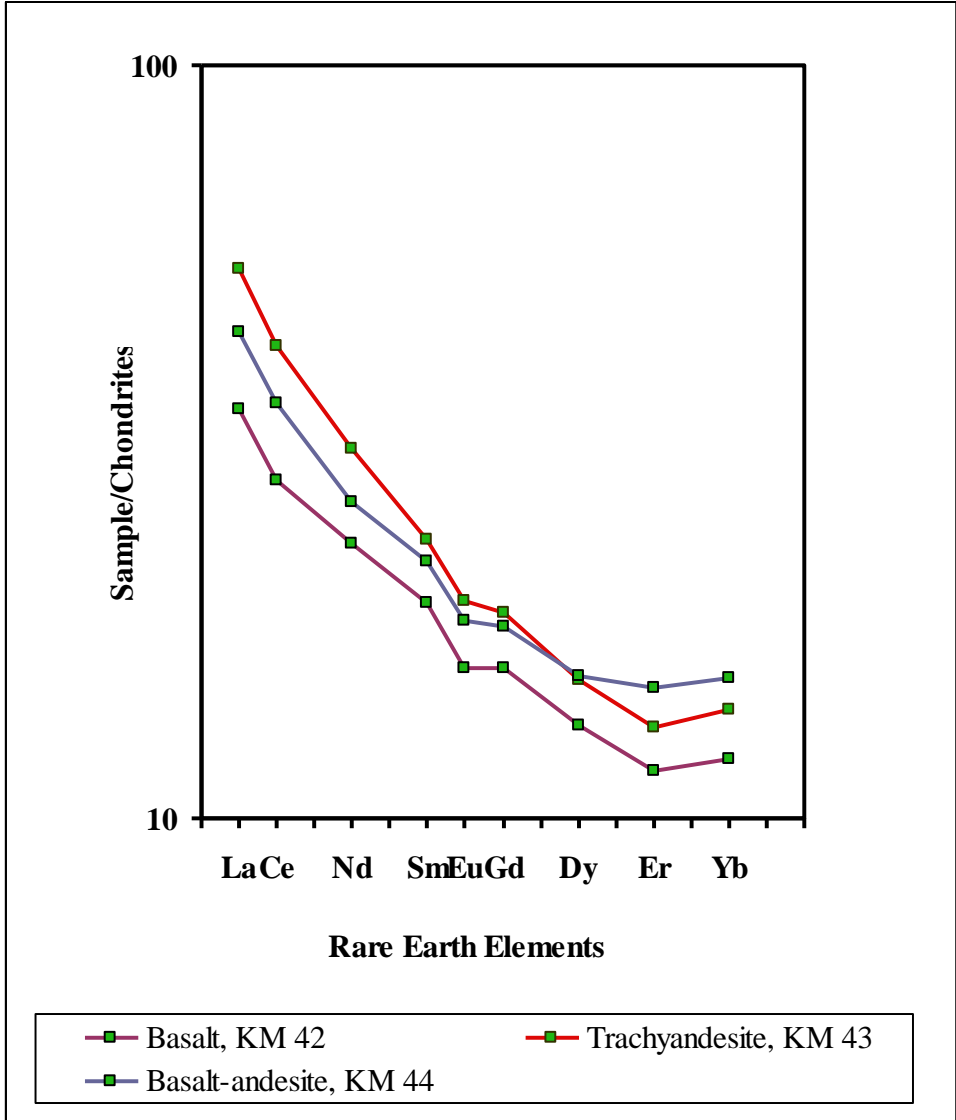


Figure 3.40. The REE patterns for the Middle Eocene volcanic rocks unit (E^v).

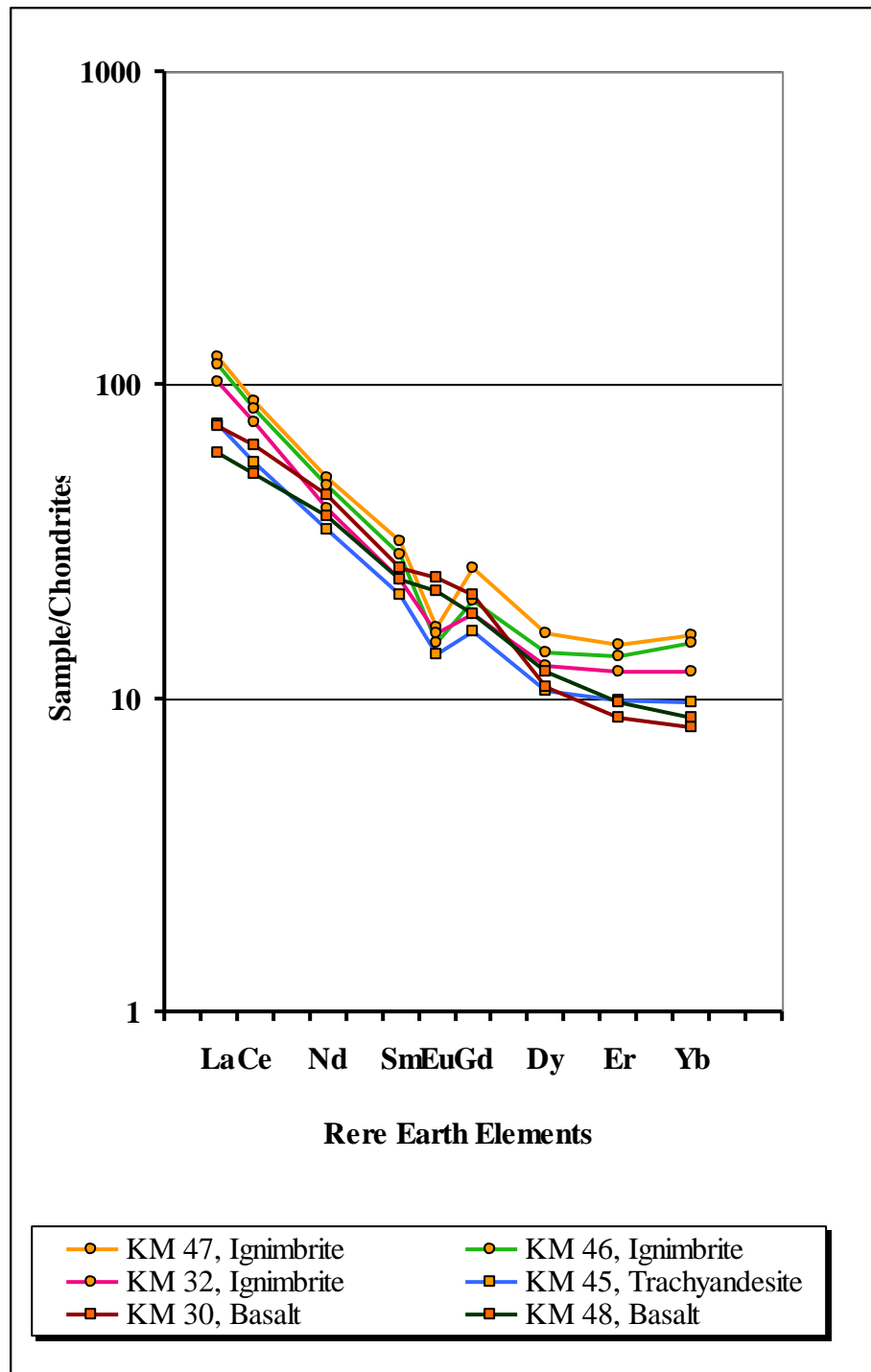


Figure 3.41. The REE patterns for the first Late Eocene sequence (units E^{ab} and E^{ig1}).

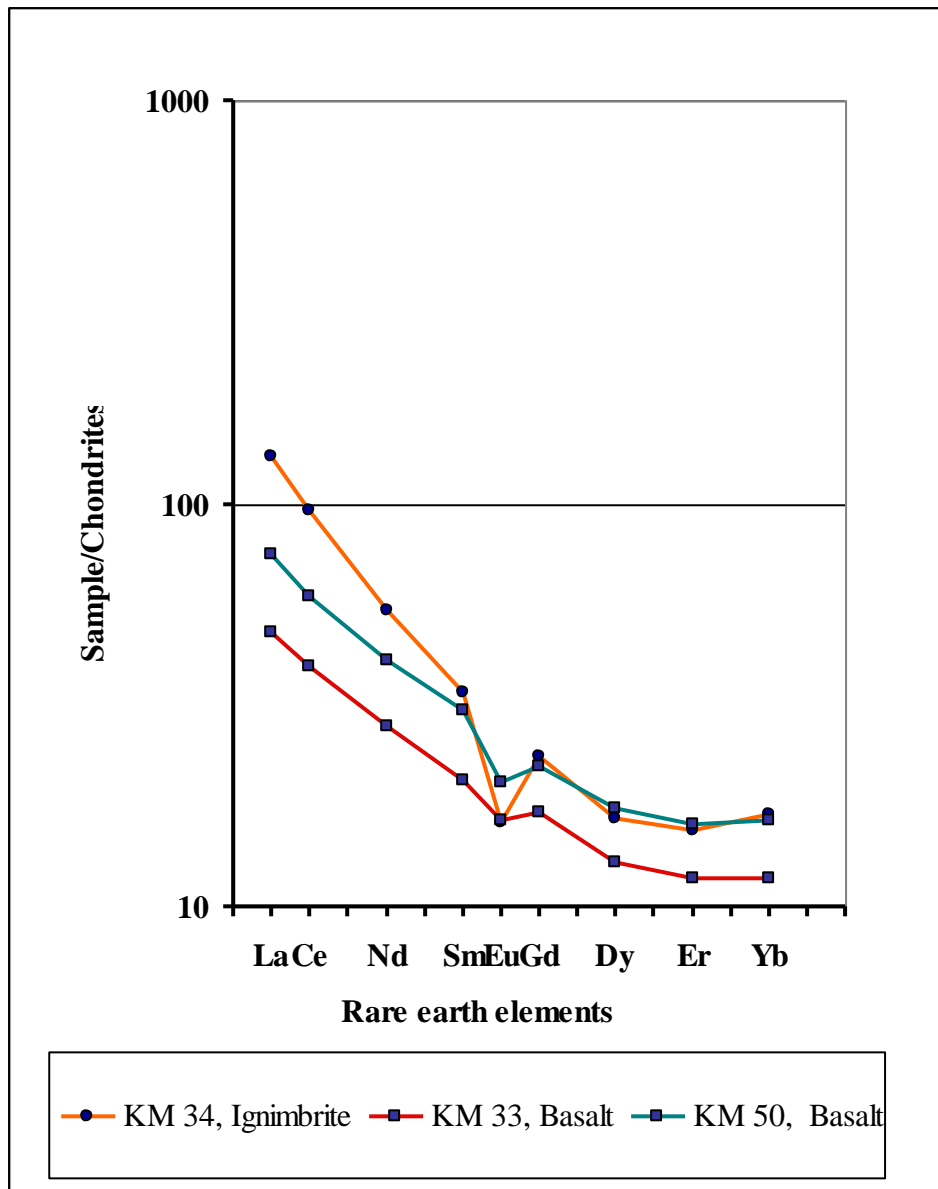


Figure 3.42. The REE patterns for the second sequence (units E^a and E^{ig2}).

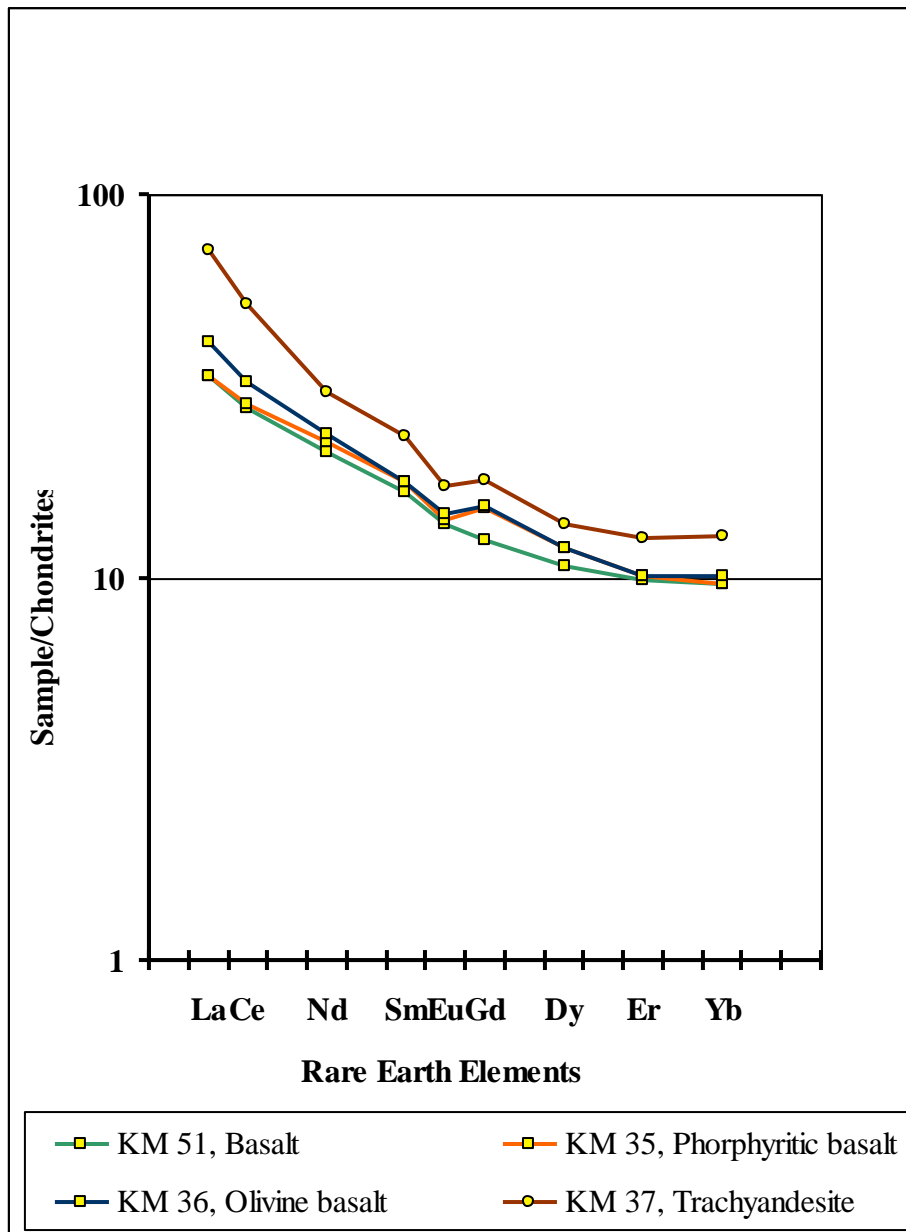


Figure 3.43. The REE patterns for the third Late Eocene sequence (units E^{hy} and E^{ig3}) of the Bijgerd-Kuh e Kharchin area.

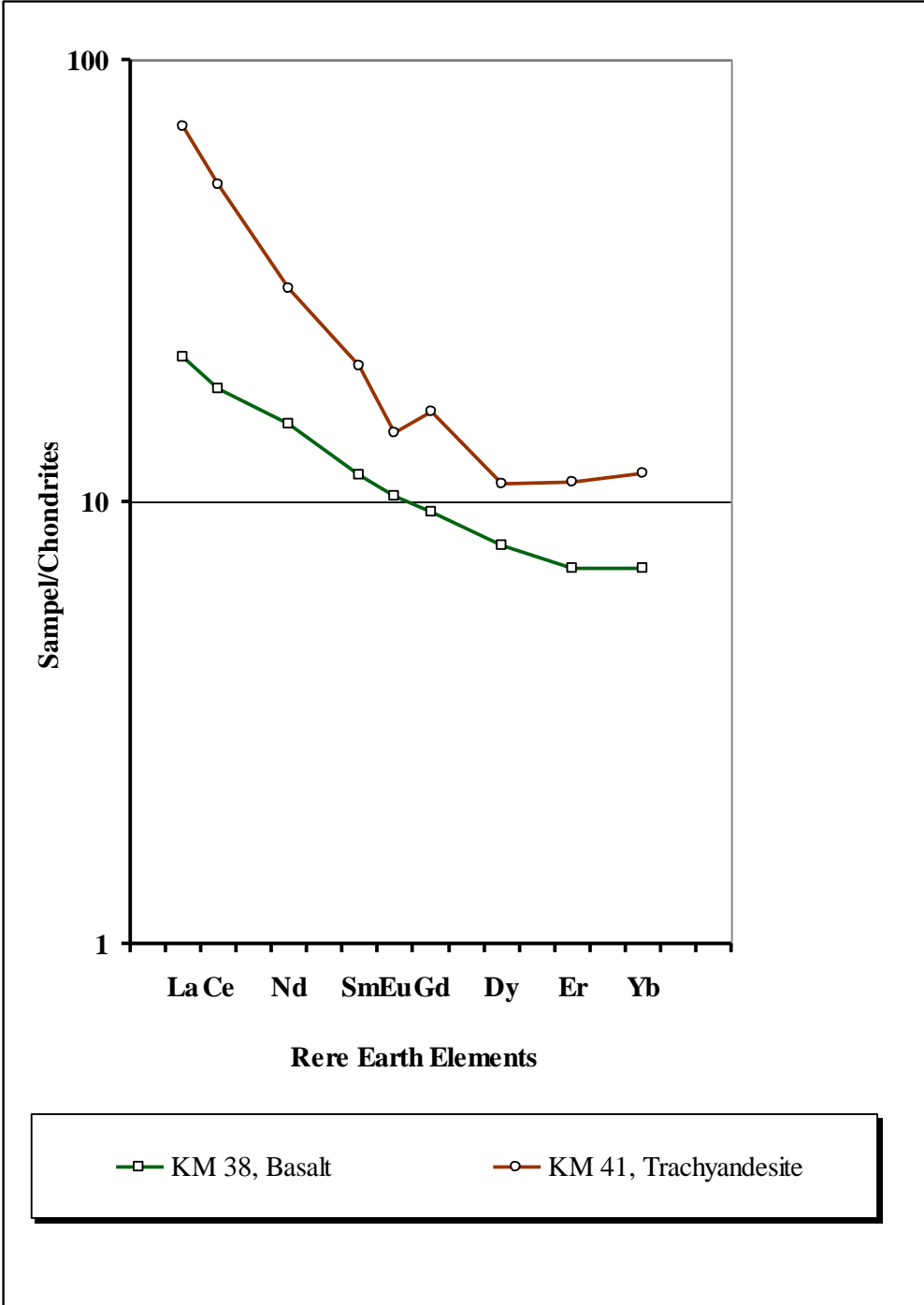
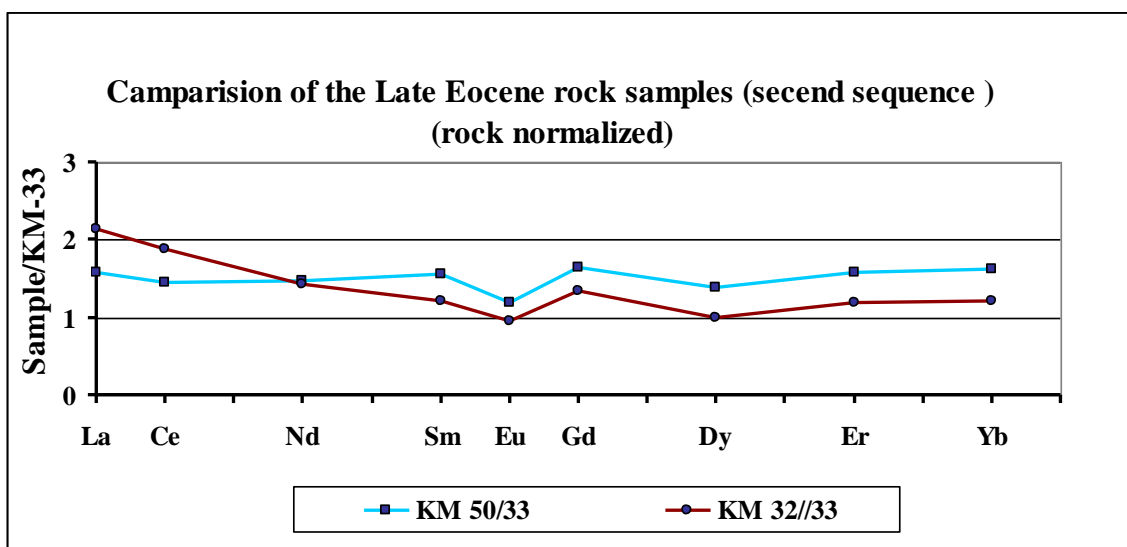
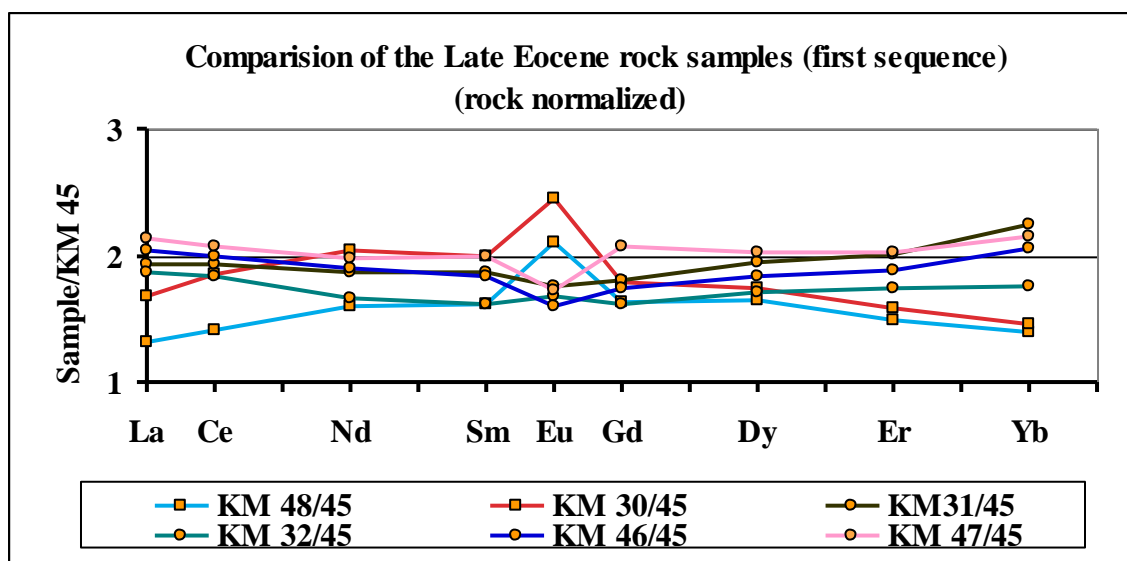
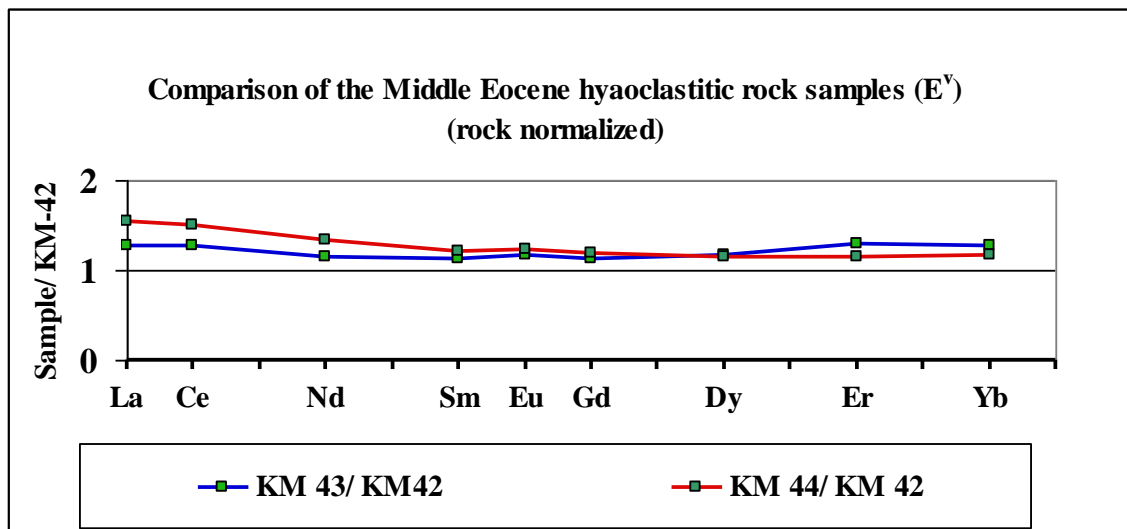


Figure 3.44. The REE patterns for the fourth sequence (units E^b and E^{ig4}).



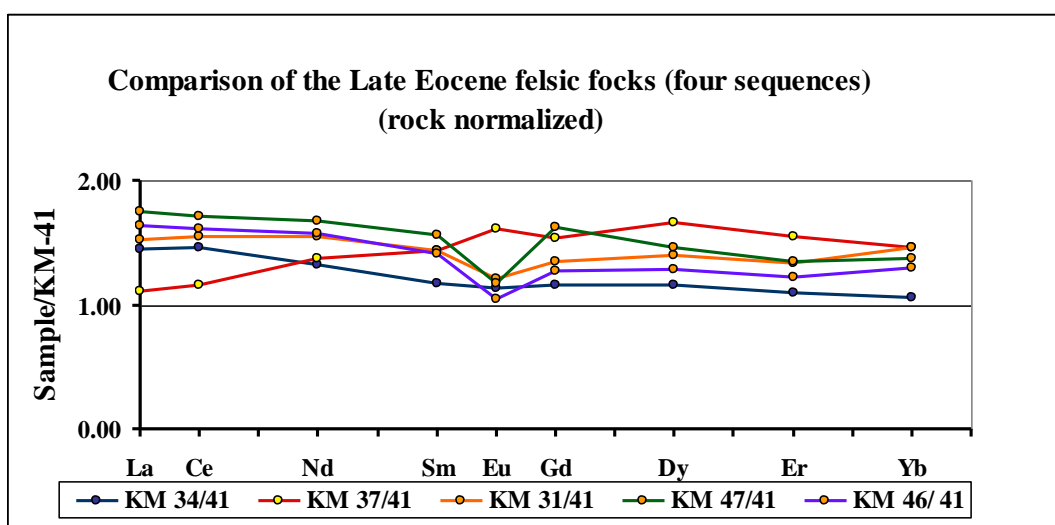
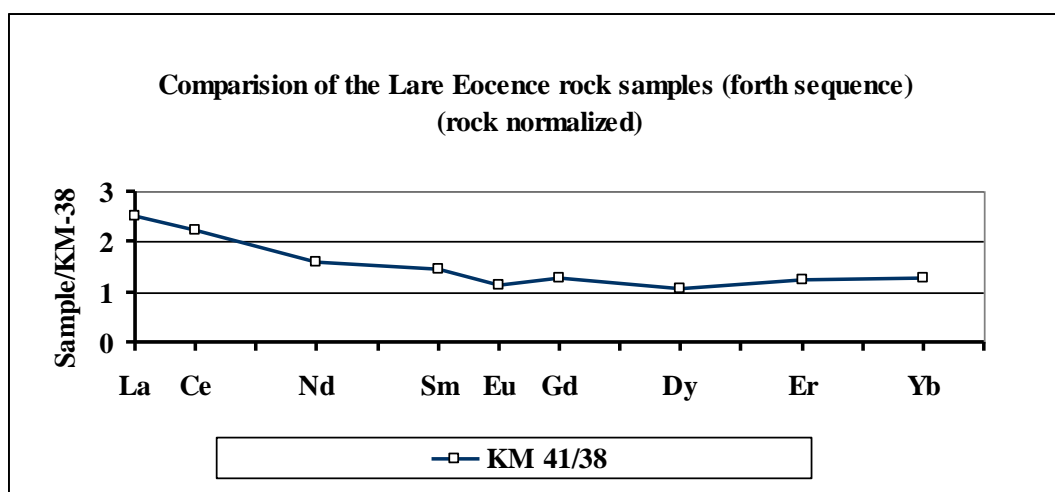
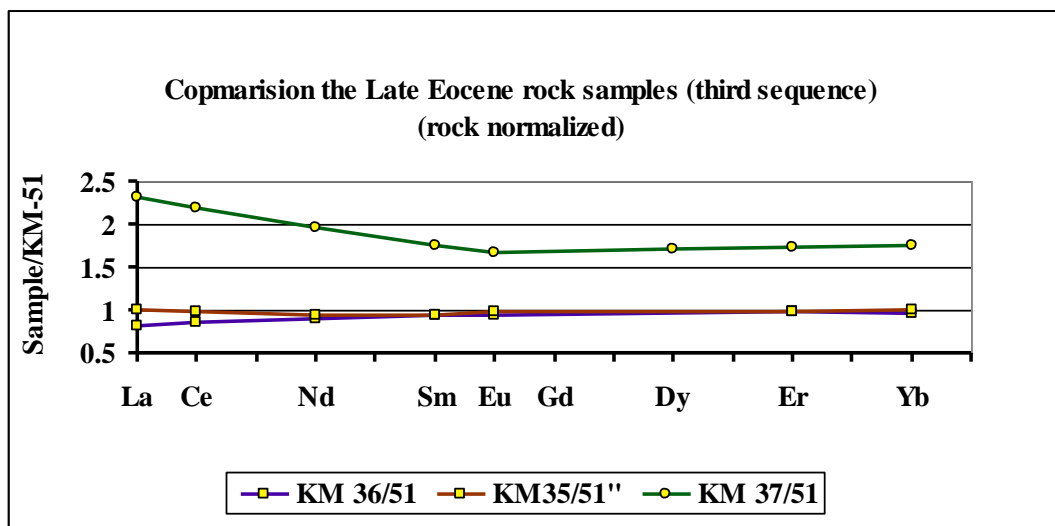


Figure 3.45. Comparisons of REE patterns of collected samples in each sequence. The lower concentrations pattern in each diagram is considered as a primitive rock.

Due to the excellent resistance of Zr and Ti during hydrothermal alteration (Krebs, 2006), they can be used in correlating the hyaloclastic units, and in tracing their sources (Figures 3.46-3.47).

As mentioned before, since the majority of rock samples are altered to varying degrees, the K_2O values are not reliable, therefore instead of the K_2O/SiO_2 ratio, values of some resistant trace elements like Zr versus SiO_2 in the bivariate diagrams can be used to correlate and trace the source of rocks.

In the Zr vs. SiO_2 diagram (Figure 3.47) almost all hyaloclastic rocks fall in the sub-alkaline field and show an evolution from basalt toward andesite-trachyandesite. The negative correlation in the TiO_2 vs. Zr diagram is discerned (Figure 3.46).

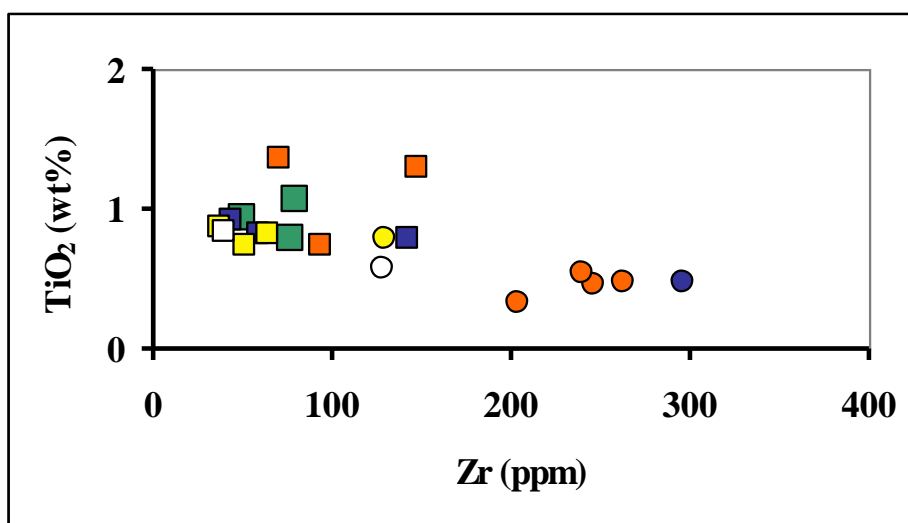


Figure 3.46. TiO_2 (wt%) plotted vs. Zr (ppm). TiO_2 correlates negatively with Zr.
 Middle Eocene ■ E^v, E^{gt} Sequence 1: ■ E^{ab} E^{ig1} Sequence 2: ■ E^a Sequence 3: ■ E^{hy} ● E^{ig3}
 Sequence 4: □ E^b ○ E^{ig4}

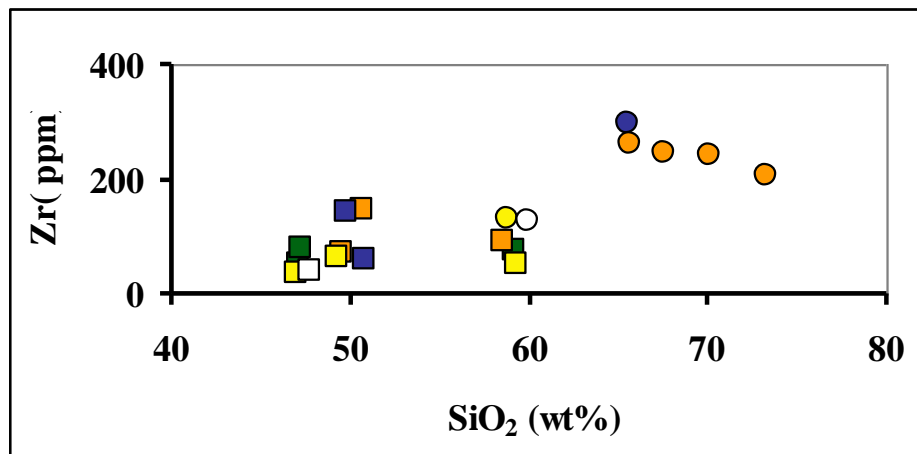


Figure 3.47. Zr (ppm) plotted vs. SiO₂ (wt%). Trendlines for Zr and SiO₂ concentrations show a positive correlation. Middle Eocene ■ E^v, E^{gt} Sequence 1: ■ E^{ab} E^{ig1} Sequence 2: ■ E^a Sequence 3: ■ E^{hy} ● E^{ig3} Sequence 4: □ E^b ○ E^{ig4}

The incompatible elements Zr is plotted against the other incompatible elements such as La, Nb, and Ce in Figure 3.47. The average values of Zr and La, Nb, and Ce correlate positively with increasing SiO₂.

In Figure 3.49 Ce and Nd concentrations are plotted against La. Similar incompatible elements are expected to behave similarly. Plots in Figure 3.50 display similar positive correlation. Other bivariate diagrams of Sm vs. La and U vs. Th are shown in Figures 3.49 and 3.50.

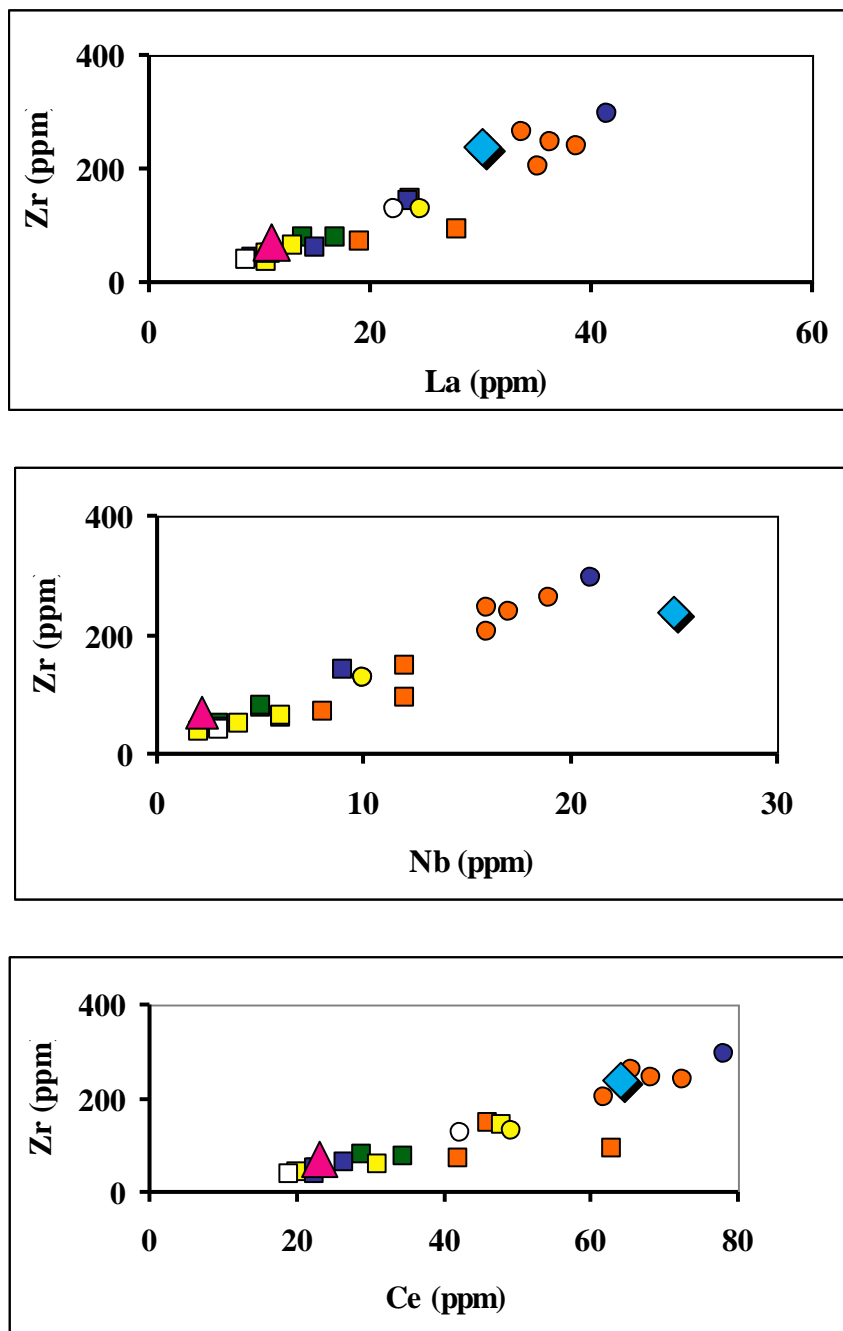


Figure 3.48. Zr plotted against La, Nb, and Ce. In all three diagrams, behavior of the two incompatible elements show a positive correlation. Similar incompatible elements may be expected to behave similarly. Middle Eocene E^v, E^{gt} Sequence 1: E^{ab}, E^{ig1} Sequence 2: E^a Sequence 3: E^{hy} E^{ig3} Sequence 4: E^b E^{ig4} Upper continental crust average \blacklozenge and Lower continental crust average \blacktriangle have been included for comparison. (Data from Taylor and McLennan, 1985).

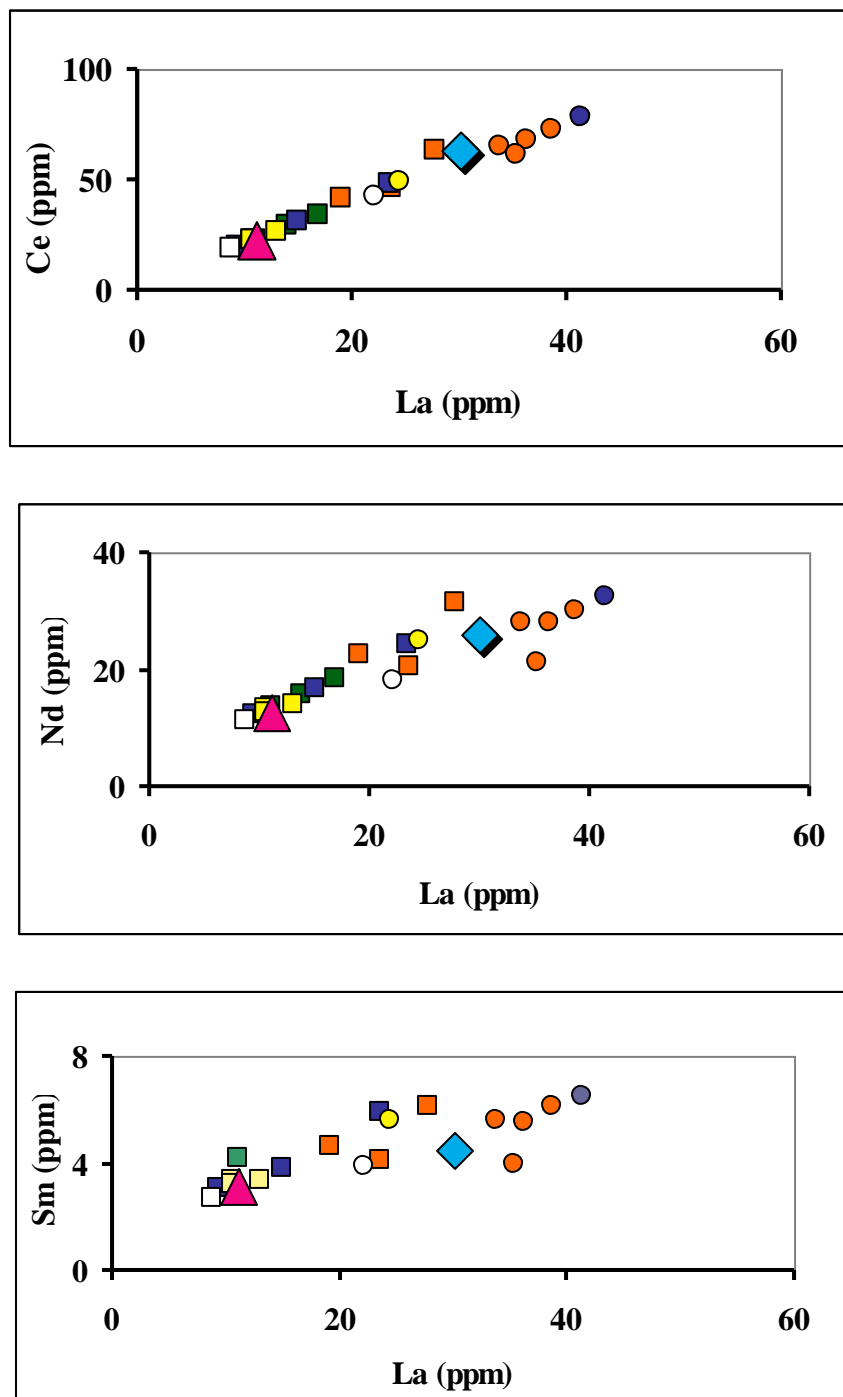


Figure 3.49. Ce and Nd concentrations plotted against La. Ce, Nd, and La are also incompatible elements and behave similarly.

Middle Eocene E^V , E^{gt} Sequence 1: E^{ab} E^{ig1} Sequence 2: E^a Sequence 3: E^{hy} E^{ig3}
 Sequence 4: E^b E^{ig4} Upper continental crust average \blacklozenge and Lower continental crust average \blacktriangle have been included for comparison. (Data from Taylor and McLennan, 1985).

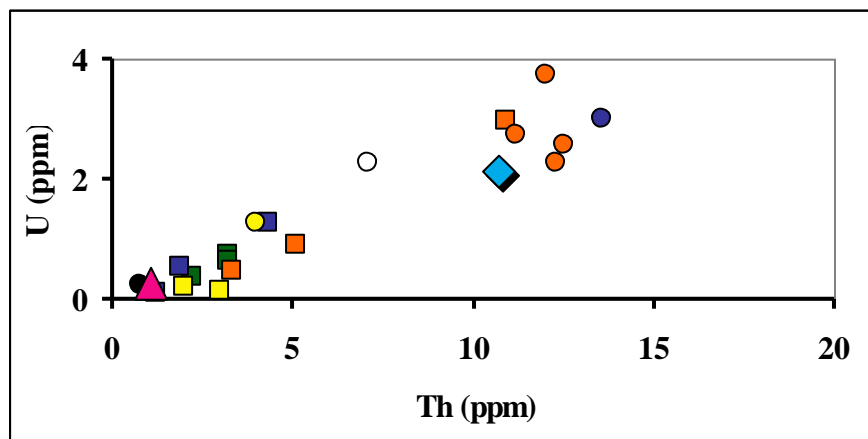


Figure 3.50. U concentrations plotted against Th.

Middle Eocene ■ E^v , E^{gt} Sequence 1: ■ E^{ab} E^{ig1} Sequence 2: ■ E^a Sequence 3: ■ E^{hy} ■ E^{ig3}
 Sequence 4: □ E^b ○ E^{ig4}

Upper crust average ◆ and Lower crust average ▲ have been included for comparison. (Data from Taylor and McLennan, 1985).

Incompatible La is plotted against compatible Yb for all rock samples taken in both Middle Eocene and each of the Late Eocene sequences (Figure 3.51).

Some variation is seen in the concentrations of the incompatible La, while some little variation can be seen in the compatible Yb concentrations in most diagrams.

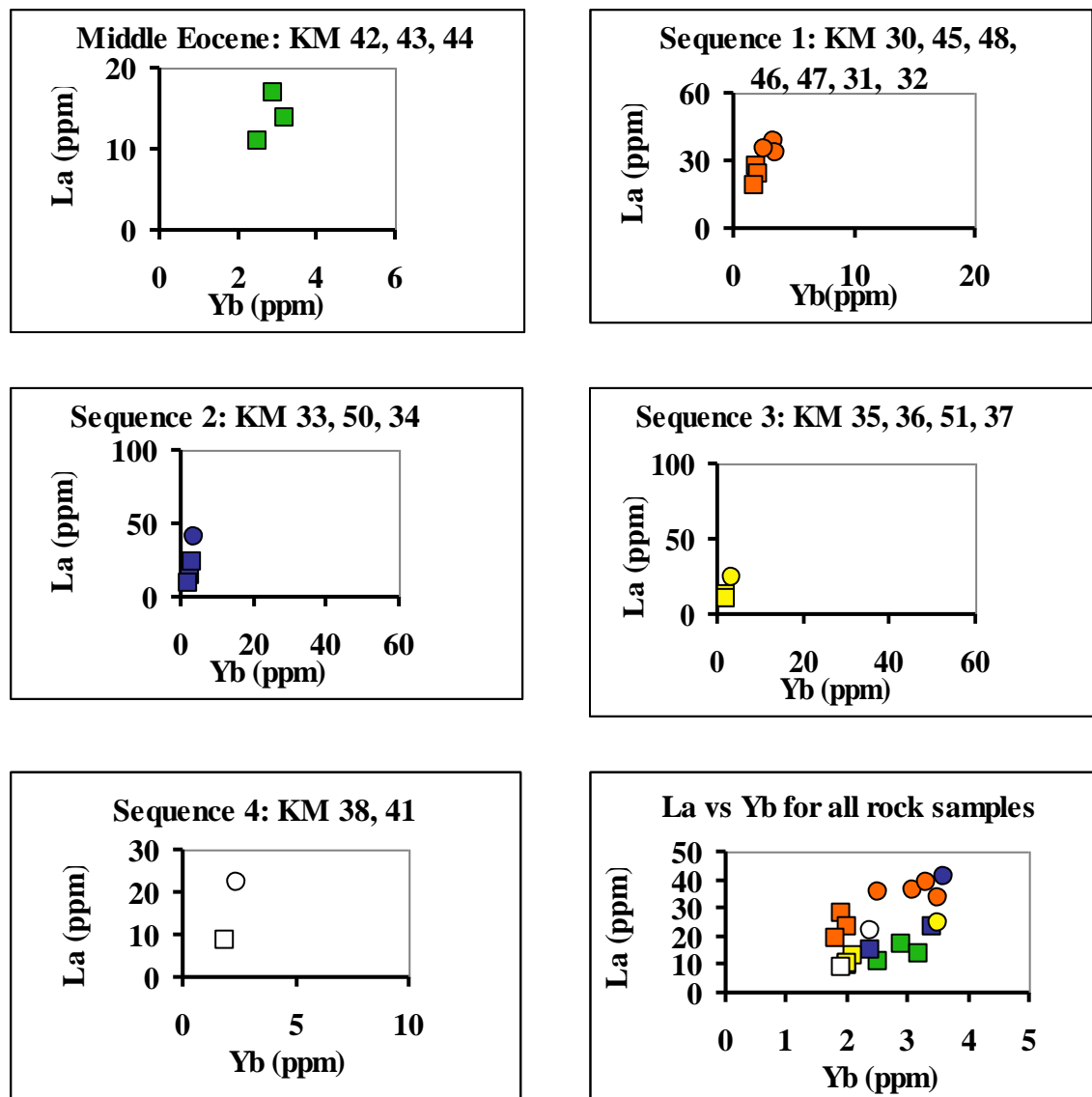


Figure 3.51. La concentrations plotted against Yb for each Upper Eocene sequence and for all rock samples.

Middle Eocene ■ E^v , E^{gt} Sequence 1: ■ E^{ab} E^{ig1} Sequence 2: ■ E^a Sequence 3: ■ E^{hy} ● E^{ig3}
 Sequence 4: □ E^b ○ E^{ig4} Upper crust average ◆ and Lower crust average ▲ have been included for comparison. (Data from Taylor and McLennan, 1985).

Table 3.4. Rare earth element concentrations (ppm) obtained through isotope dilution mass spectrometry at GSU.

	Middle Eocene		Late Eocene										
			Four alternating sequences of hyaloclastite & ignimbrite										
			Sequence 1		Sequence 2		Sequence 3		Sequence 4				
	$E^v E^{gt}$		E^{ab}		E^a	E^{ig2}	E^{hy}		E^{ig3}	E^b	E^{mb3}		E^{ig4}
	Hyaloclastite		Ignimbrite		Hyaloclastite	Ignimbrite	Hyaloclastite	Ignimbrite	Hyaloclastite	Breccia	Tuff	Ig	
	KM 42	KM 30	KM 31	KM 32	KM 33	KM 34	KM 35	KM 36	KM 37	KM 38	KM 39	KM 40	KM 41
La	10.58	23.11	32.61	23.30	14.68	34.90	10.20	12.10	22.58	6.66	17.00	22.15	21.45
Ce	22.20	51.68	63.51	45.34	32.14	67.83	22.80	25.23	42.00	14.62	34.00	42.84	39.00
Nd	12.64	26.57	27.29	23.90	16.65	28.86	12.97	14.41	18.23	8.92	15.20	19.75	18.88
Sm	3.63	5.00	5.40	4.57	3.96	5.59	3.21	3.37	4.46	2.20	3.20	4.03	3.89
Eu	1.16	1.74	1.14	1.16	1.18	1.19	1.10	1.04	1.25	0.74	0.89	1.06	1.06
Gd	3.34	5.49	4.53	4.76	4.41	4.93	3.78	3.61	4.65	2.45	3.95	3.90	4.52
Dy	3.45	3.52	4.86	4.12	4.19	5.36	3.78	4.80	4.46	2.59	3.82	3.99	4.25
Er	2.10	1.85	3.19	2.57	2.51	2.93	2.21	2.74	2.70	1.50	2.49	2.39	2.70
Yb	2.30	1.67	3.42	2.52	2.43	3.09	2.12	2.74	2.65	1.47	2.68	2.53	2.59

Table 3.5. Trace element concentrations of the volcanic rocks in the study area, obtained at SGS (ICM90A Method).

Analytical method detection level	Middle Eocene				Late Eocene							
					Four alternating sequences of hyaloclastite & ignimbrite							
					Sequence 1							
	E ^v E st				E ^{ab}				E ^{ig1}			
	Hyaloclastite				Hyaloclastite				Ignimbrite			
	KM 42	*KM 42	KM 44	KM 43	KM 30	*KM 30	KM 48	KM 47	KM 46	KM 31	KM 32	
0.01%	Al	10.00	8.45	8.14	7.49	8.51	8.56	8.49	6.68	7.03	6.86	6.21
	Ca	8.10	8.03	7.63	4.77	6.61	6.72	5.27	2.63	3.45	0.70	2.25
	Fe	6.28	6.17	8.45	3.89	6.04	6.11	7.20	1.31	1.46	1.99	1.39
	K	1.53	1.38	1.84	1.50	1.18	1.19	0.68	4.68	2.93	4.55	1.60
	Mg	0.82	0.84	1.06	0.63	1.22	1.24	2.40	0.19	0.22	0.39	0.18
	P	0.13	0.12	0.13	0.15	0.26	0.29	0.19	0.03	0.03	0.05	0.03
	Ti	0.54	0.54	0.60	0.37	0.69	0.69	0.75	0.22	0.24	0.30	0.17
0.05 ppm	Dy	4.31	4.36	5.01	4.97	4.22	4.53	3.93	5.20	4.56	4.96	3.23
	Er	2.46	2.70	3.17	2.82	2.25	2.39	2.07	3.16	2.88	3.14	2.29
	Eu	1.14	1.23	1.32	1.40	1.93	2.05	1.58	1.21	1.08	1.24	0.67
	Gd	4.11	4.33	4.66	4.87	5.49	5.95	4.78	5.69	5.26	5.56	3.55
	Ho	0.88	0.87	1.04	1.06	0.78	0.86	0.74	1.02	0.98	1.06	0.68
	Lu	0.39	0.35	0.51	0.47	0.29	0.33	0.27	0.51	0.49	0.64	0.49
	Tb	0.67	0.73	0.78	0.87	0.80	0.89	0.71	0.95	0.82	0.86	0.57
	Pr	3.04	3.24	3.71	4.46	7.96	8.35	5.47	11.00	7.98	7.52	6.36
	Tm	0.35	0.38	0.48	0.45	0.31	0.33	0.28	0.47	0.45	0.49	0.36
	U	0.36	0.47	0.65	0.74	0.91	1.00	0.47	2.57	3.75	2.73	2.27
0.1 ppm	Ce	22.80	24.20	28.90	34.40	62.80	66.60	41.90	72.40	68.30	65.50	61.70
	Nd	13.80	14.50	15.70	18.50	31.50	34.00	22.60	30.20	28.10	28.10	21.30
	La	11.00	11.60	13.90	16.90	27.80	30.00	19.10	38.70	36.30	33.80	35.30
	Yb	2.50	2.60	3.20	2.90	1.90	2.10	1.80	3.30	3.10	3.50	2.50
	Th	2.20	1.60	3.20	3.20	5.00	5.10	3.30	12.50	12.00	11.20	12.30
	Sb	0.20	0.50	0.70	0.10	0.10	<0.1	0.20	1.00	2.00	1.60	1.20
	Sm	3.70	4.00	4.20	4.50	6.10	6.60	4.60	6.10	5.50	5.60	4.00
	Cs	0.80	0.90	0.90	0.50	1.50	1.50	1.40	3.00	2.80	3.10	2.40
Sr	461.00	393.00	315.00	317.00	589.00	593.00	515.00	122.00	150.00	128.00	146.00	

* is replicate

Table 3.6 continued.

Analytical method detection levele	Late Eocene											
	Sequence 2				Sequence 3			Sequence 4				
	E ^a		E ^t	E ^{ig2}	E ^{hy}		E ^{ig3}	E ^b	E ^{mb3}		E ^{ig4}	
	Hy			Ig	Hy		Ig	Hy	Breccia	Tuff	Ig	
	KM 33	KM 50	KM49	KM 32	KM 35	KM 36	KM 37	KM 38	KM 39	KM 40	KM 41	
0.01%	Al	8.10	8.17	9.80	6.21	10.60	8.11	7.50	8.38	6.36	6.81	7.22
	Ca	6.24	3.88	7.64	2.25	8.42	6.43	3.36	7.15	6.03	0.55	4.65
	Fe	6.18	4.45	0.96	1.39	7.12	7.31	5.48	7.54	2.59	2.91	3.85
	K	1.10	1.12	0.96	1.60	0.23	0.86	2.03	0.55	0.10	0.18	2.89
	Mg	1.34	1.00	1.33	0.18	1.37	3.17	0.80	2.81	0.72	0.09	0.39
	P	0.10	0.14	0.09	0.03	0.11	0.08	0.13	0.07	0.04	0.04	0.06
	Ti	0.46	0.36	0.48	0.17	0.50	0.46	0.43	0.47	0.20	0.23	0.32
0.05 ppm	Dy	4.14	5.71	3.46	3.23	3.86	3.57	5.93	3.34	3.96	4.75	3.56
	Er	2.57	3.39	2.11	2.29	2.15	2.15	3.65	1.88	2.60	3.26	2.35
	Eu	1.23	1.47	1.04	0.67	1.02	1.06	1.66	0.91	0.94	1.06	1.03
	Gd	4.48	5.79	3.58	3.55	3.93	3.99	6.34	3.29	4.03	5.31	4.13
	Ho	0.84	1.17	0.74	0.68	0.78	0.74	1.21	0.68	0.85	1.08	0.75
	Lu	0.50	0.55	0.31	0.49	0.33	0.35	0.58	0.29	0.48	0.60	0.34
	Tb	0.73	0.97	1.20	0.57	0.65	0.56	1.00	0.52	0.66	0.83	0.62
	Pr	3.96	6.03	2.77	6.36	3.05	3.32	6.10	6.10	4.29	6.34	5.00
	Tm	0.38	0.52	0.30	0.36	0.31	0.32	0.51	0.28	0.42	0.51	0.34
U	0.53	1.27	0.10	2.27	0.09	0.21	1.27	0.23	1.45	1.53	2.26	
0.1 ppm	Ce	31.00	47.90	20.10	61.70	22.60	26.40	49.10	18.90	35.30	50.40	42.30
	Nd	16.70	24.40	12.20	21.30	13.40	14.10	24.90	11.30	16.50	23.40	18.10
	La	15.00	23.50	9.40	35.30	10.60	13.00	24.50	8.80	17.50	26.70	22.20
	Yb	23.30	3.40	2.00	2.50	2.00	2.10	3.50	1.90	2.70	3.30	2.40
	Th	1.90	4.30	1.20	12.30	1.60	0.70	4.00	0.80	4.30	6.00	7.10
	Sb	0.20	0.20	<0.1	1.20	<0.1	0.20	0.50	0.10	0.70	0.90	0.60
	Sm	3.80	5.90	3.10	4.00	3.40	3.40	5.60	2.70	3.80	5.00	3.90
	Cs	0.80	6.40	1.10	2.40	0.40	0.50	0.80	0.20	0.30	1.80	4.00
	Sr	451.00	597.00	517.00	146.00	539.00	435.00	365.00	444.00	93.30	110.00	366.00

Table 3.6 continued.

Analytical method detection level	Middle Eocene						Late Eocene						
	Four alternating sequences of hyaloclastite & ignimbrite												
	Sequence 1												
	E ^a E ^g			E ^b				E ^{g1}					
	Hyaloclastite			Hyaloclastite				Ignimbrite					
	KM 42	KM 42	KM 44	KM 43	KM 30	KM 30	KM 48	KM 45	KM 47	KM 46	KM 31	KM 32	
0.05 ppm	Gd	4.11	4.33	4.66	4.87	5.49	5.95	4.78	4.25	5.69	5.26	5.56	3.55
	Ho	0.88	0.87	1.04	1.06	0.78	0.86	0.74	0.72	1.02	0.98	1.06	0.68
	Lu	0.39	0.35	0.51	0.47	0.29	0.33	0.27	0.31	0.51	0.49	0.64	0.49
	Tb	0.67	0.73	0.78	0.87	0.29	0.89	0.71	0.64	0.95	0.82	0.86	0.57
	Pr	3.04	3.24	19.00	4.46	7.96	8.35	5.47	5.47	8.45	7.98	7.52	6.36
	Tm	0.35	0.38	0.48	0.45	0.31	0.33	0.28	0.31	0.47	0.45	0.49	0.36
	U	0.36	0.47	0.65	0.74	0.91	1.00	0.47	2.98	2.57	3.75	2.73	2.27
0.2 ppm	Rb	32.90	36.00	48.20	37.80	30.50	31.80	22.40	49.80	165.00	102.00	156.00	58.60
0.5 ppm	Ba	405.00	388.00	342.00	498.00	547.00	554.00	335.00	716.00	737.00	727.00	838.00	317.00
	Co	21.30	25.40	36.30	10.30	22.70	24.10	28.30	17.90	2.00	3.00	3.10	3.40
	Zr	49.60	61.40	79.10	76.80	93.00	94.60	71.10	147.00	240.00	246.00	263.00	204.00
	Y	21.90	23.10	26.10	26.60	20.20	21.60	19.60	19.70	28.60	27.10	1.00	2.00
5 ppm	V	271.00	262.00	275.00	66.00	160.00	172.00	211.00	147.00	15.00	18.00	30.00	21.00
	Zn	184.00	196.00	254.00	352.00	87.00	77.00	84.00	85.00	53.00	45.00	65.00	65.00
	Cu	21.00	20.00	26.00	29.00	12.00	14.00	14.00	64.00	<5	5.00	<5	8.00
	Ni	33.00	8.00	31.00	23.00	26.00	27.00	33.00	37.00	16.00	20.00	<5	7.00
	Se	29.00	26.00	32.00	19.00	15.00	16.00	20.00	17.00	6.00	5.00	5.00	<5
	Pb	14.00	14.00	19.00	12.00	29.00	25.00	11.00	33.00	11.00	8.00	16.00	14.00
1 ppm	Ge	1.00	1.00	2.00	2.00	1.00	2.00	1.00	<1	1.00	1.00	2.00	2.00
	Hf	2.00	2.00	3.00	3.00	4.00	3.00	2.00	4.00	7.00	7.00	7.00	5.00
	Nb	3.00	4.00	5.00	5.00	12.00	12.00	8.00	12.00	17.00	16.00	19.00	16.00
	Ga	19.00	22.00	22.00	18.00	21.00	21.00	19.00	15.00	15.00	14.00	5.56	3.55
10 ppm	Cr	20.00	20.00	30.00	20.00	20.00	20.00	20.00	50.00	<10	20.00	20.00	20.00
	Li	20.00	20.00	10.00	10.00	20.00	20.00	30.00	20.00	20.00	40.00	20.00	40.00
	Mn	1360.00	1270.00	2030.00	1890.00	1250.00	1270.00	1480.00	750.00	1010.00	1530.00	370.00	540.00

Table 3.6 continued.

Analytical method detection level	Late Eocene											
	Sequence 2				Sequence 3				Sequence 4			
	E ^a		E st	E ^{ig2}	E ^{hy}		E ^{ig3}	E ^b	E ^{mb3}		E ^{ig4}	
	*Hy			*Ig	*Hy		*Ig	*Hy	Breccia	Tuff	*Ig	
	KM 33	KM 50	KM48	KM 32	KM 35	KM 36	KM 37	KM 38	KM 39	KM 40	KM 41	
0.05 ppm	Gd	4.48	5.79	3.58	3.55	3.93	3.99	6.34	3.29	4.03	5.31	4.13
	Ho	0.84	1.17	0.74	0.68	0.78	0.74	1.21	0.68	0.85	1.08	0.75
	Lu	0.50	0.55	0.31	0.49	0.33	0.35	0.58	0.29	0.48	0.60	0.34
	Th	0.73	0.97	2.00	0.57	0.29	0.56	1.00	0.52	0.66	0.83	0.62
	Pr	3.96	6.03	2.77	6.36	3.05	3.32	6.10	6.10	4.29	6.34	5.00
	Tm	0.38	0.52	0.30	0.36	0.31	0.32	0.51	0.28	0.42	0.51	0.34
	U	0.53	1.27	0.10	2.27	0.09	0.21	1.27	0.23	1.45	1.53	2.26
0.2 ppm	Rb	28.20	27.40	21.80	58.60	1.60	15.30	59.60	7.40	2.40	8.00	112.00
0.5 ppm	Ba	409.00	710.00	404.00	317.00	213.00	387.00	650.00	239.00	442.00	74.10	624.00
	Co	23.90	12.10	24.90	3.40	24.80	39.80	14.90	37.00	9.60	2.50	16.00
	Zr	59.60	142.00	44.10	204.00	36.60	64.60	129.00	39.20	137.00	150.00	128.00
	Y	<1	32.50	19.30	2.00	2.00	2.10	3.50	1.90	2.70	3.30	2.40
5 ppm	V	176.00	57.00	76.00	21.00	267.00	238.00	78.00	292.00	77.00	69.00	13.00
	Zn	87.00	80.00	74.00	65.00	111.00	107.00	129.00	103.00	200.00	41.00	130.00
	Cu	67.00	34.00	22.00	8.00	21.00	100.00	53.00	204.00	21.00	20.00	31.00
	Ni	<5	38.00	25.00	7.00	38.00	29.00	5.00	17.00	6.00	5.00	24.00
	Sc	20.00	19.00	8.00	<5	29.00	24.00	18.00	27.00	11.00	10.00	13.00
	Pb	19.00	15.00	5.00	14.00	11.00	10.00	24.00	16.00	29.00	28.00	24.00
1 ppm	Ge	2.00	1.00	1.00	2.00	1.00	1.00	2.00	2.00	2.00	3.00	2.00
	Hf	2.00	4.00	1.00	5.00	1.00	2.00	4.00	1.00	4.00	4.00	4.00
	Nb	6.00	9.00	3.00	16.00	2.00	6.00	10.00	3.00	8.00	11.00	10.00
	Ga	4.48	20.00	20.00	3.55	18.00	19.00	20.00	19.00	14.00	17.00	16.00
10 ppm	Cr	20.00	40.00	10.00	20.00	20.00	40.00	20.00	50.00	20.00	20.00	50.00
	Li	20.00	20.00	<10	40.00	<10	<10	10.00	<10	50.00	80.00	<10
	Mn	800.00	1250.00	1160.00	540.00	1280.00	1300.00	960.00	1240.00	820.00	450.00	965.00

*Hyaloclastite *Ignimbrite

CHAPTER 4

DISCUSSION

Field Relationships

It is difficult to discuss the structural features of the Bijgerd-Kuh e Kharchin study area without considering the structural features northwest of Saveh. As was mentioned before in Chapter 1, the remnants of Paleozoic metamorphic rocks such as phyllite and slate, attributed to the Sanandaj-Sirjan zone, are tectonically juxtaposed with the Eocene volcanic rocks south of the Bijgerd-Kuh e Kharchin area.

The Bijgerd fault (Figure 3.2 b) is the most important structural feature in the Bijgerd-Kuh e Kharchin area. This fault is one of the subsidiary faults of the main, NW-SE striking Kushk Nosrat fault which extends from west of Hoz e Sultan, west of Saveh, to northwest of Saveh, and which connects to the Avaj fault, northwest of the area, around Hamedan. The Bijgerd fault is apparently a thrust fault with a left-lateral strike-slip component, and its minimum age may be post-Eocene.

The Bijgerd fault is cut by smaller left- and right-lateral strike-slip faults, which, given that these faults cut the Qom limestone, must be post Oligo-Miocene, although in places, the age of some of the faults could be as young as Quaternary. However, the latest movements along these faults are not documented yet.

The general trend of the geological units in this area is NW-SE, which is parallel to the fold axes, although this trend is changed around the Bijgerd fault, probably indicating rotation by the fault.

Field investigation suggests a change in the nature of volcanic eruption and deposition of volcanic-sedimentary rocks during Eocene. For example, in some places of the Uromieh-Dokhtar zone acidic volcanic rocks and ignimbrites (e.g. E^{ig} units) are more extensive than basic and intermediate lava.

An interesting note about the eruption of the E^v unit is the occurrence of hyaloclastic tuff and breccia at its base, and existence of hydrated volcanic fragments in it, which may indicate formation under water. The presence of a sequence of shallow and intermediate depth marine sedimentary microfossils, such as Nummulite and radiolaria in the E^{gt} unit, suggests that the depositional environment, in which the E^{gt} unit was formed, was a marine basin.

In places, in the E^v, E^{ab}, E^a, E^{hy}, and E^b units, the basic and intermediate lavas probably cooled in this marine environment, forming hyaloclastites. As the lavas were erupted in this aqueous environment, the vesicles at their base were filled with calcium carbonate and a variety of green minerals. Eruptions of lava, especially acidic ones, brought glass shard and lithic fragments in contact with water, growing green minerals such as chlorite and epidote, and forming green tuff which is so common in the Uromieh-Dokhtar zone.

The green tuff, dominated by volcanic grains (Winter, 2001), were ejected as glass shards (now devitrified) and other fragments into a marine environment due to the explosive nature of acidic eruptions, forming the green minerals and various clay minerals.

Perhaps for this reason, the E^{gt} unit, dominated by green tuff, is a good prospect for clay mineral exploration in the Uromieh-Dokhtar zone. Higher in the E^v unit, the density of the vesicles reduces, and lavas resemble flows that form on land.

After the deposition of the autoclastic breccia, which apparently form on land (Fairbridge, 1987), a variety of tuff and green breccia, with hydrated volcanic clasts, were deposited on the autoclastic breccia, again indicating formation under water. In some places (e.g. E^h unit), lavas were probably laid down in shallow marine environment, and for this reason, they form few cm- to mm-wide blobs (lumps) in a highly hydrated, oxidized, and altered volcanic matrix.

In many cases, the exterior of the margins of these blobs is made of volcanic glass or oxidized material, while the interior parts are more intact, and have preserved original volcanic texture and structure. Therefore, the change in the nature of the volcanic eruption during Middle Eocene in the Bijgerd-Kuh e Kharchin area, and for that matter in the Uromieh-Dokhtar zone, may be explained by hypothesizing (Meckel et al., 2007) a subsidence in the depositional basin, from land to a shallow marine environment.

Because the E^{st1} and E^{st2} units are laid down on acidic-ignimbritic units (E^{ig1a}, E^{ig1b}), some of which are pyroclastic and explosive, it is probable that the volcanic-sedimentary rocks in these two units are formed as a result of the deposition of volcanic ash, while the pyroclastic and explosive components formed the ignimbrites of the E^{ig1a}, E^{ig1b} units (Figure 3.13).

The E^{st1} and E^{st2} units probably formed by the deposition of the volcanic ash related to the same acidic-ignimbritic volcanic activity, probably in the subsiding marine environment mentioned above.

Since barite (BaSO₄) is commonly deposited in epithermal environments (Ganeshram et al., 2003), the outcrops of barite in the E^a unit, exposed along the road north of the Baramoon village, may represent the hydrothermal phases related to the andesitic lava.

The olivine basaltic lava at the middle and hyaloclastic breccia at higher stratigraphic levels in the E^{hy} unit, indicates explosive volcanic/volcaniclastic activity under water, probably in the Middle Eocene shallow marine basin. However, the products of the explosive Late Eocene volcanic/volcaniclastic activity at the base of the E^{hy} unit, made of basalt and porphyritic, andesitic lava, probably formed in a dry land environment. The onland formation of the volcanic and volcano-sedimentary rocks, followed by a subaqueous deposition can be due a subsidence in the Late Eocene depositional basin. The relatively more differentiated porphyritic andesitic lava at the base of the E^{hy} unit is covered by less differentiated olivine basalt lava.

The question is how the more differentiated andesitic magma was erupted before the less differentiated olivine basaltic magma. Perhaps, due to the magmatic differentiation and floatation, plagioclase phenocrysts accumulated at the top of the magma chamber, producing andesite from the more differentiated part, followed by olivine basalt in the E^{hy} unit. Thus, geology of the E^{hy} unit indicates that magmatic differentiation has played a role in the magmatic evolution of the Bijgerd-Kharchin area.

Mafic clasts (inclusions), in a felsic groundmass, contain plagioclase phenocrysts probably indicating mingling of the differentiating basic-intermediate magma with rhyolitic magma (Nelson et al., 1995; Browne et al., 2006). Thus, the mafic inclusions can be evidence for magma mingling in the ignimbrites, and explain inclusions' compositional variation from rhyolite to trachy-andesite.

Existence of hybrid breccia, with felsic and mafic clasts, with oxidized acidic, rhyolitic, and basic-intermediate clasts (Figure 3.6) in at least three volcano-stratigraphic levels (E^{mb1}, E^{mb2}, E^{mb3}) may be a good field evidence of magma mingling.

According to Meffre et al., (2004), the crenulated (wavy) edges of the mafic-intermediate clasts (Figure 3.7) may suggest chilling of hot clasts (inclusions) in the host rocks. The crenulated contacts suggest that the two mafic and intermediate magmas were plastic and hot during magma mingling (Whalen et al., 1984).

Based on mineralogy, mafic rocks (e.g., basalt) are dominated entirely by dark, fine grained silicate minerals such as pyroxene, olivine, and plagioclase (Hyndman, 1995). Therefore, the presence of the porphyritic mafic clasts, in the hyaloclastic rocks, may indicate mingling of a differentiating, or already differentiated basic-intermediate magma with a rhyolitic magma. In places, felsic clasts occur in the mafic clasts (E^{mb3} unit). Based on this textural and compositional evidence, it can be said that the upper levels of the E^{mb3} unit may indicate a progression of the magma mingling process toward homogenization and magma mixing. The red crystal- and lithic-tuffs are covered by trachyandesite in which the magma mingling and mixing are probably represented by a mixture of basic and acidic glass shards.

Although the laboratory analyses of the tuff and breccia of the study area have been difficult, the analytical results (e.g., spider diagrams) lie intermediate between those of rhyolite and basalt, providing another possible evidence for magma mingling. While hotter basic magma inserts into a viscous rhyolitic magma and directly generates a violent eruption, mixing occurs (Hildyard et al., 2000).

Extensive ignimbrites-fiammes (E^{ig1} , E^{ig2} , and E^{ig3} units), including pseudo-fiammes filled with intermediate lava, which in some cases contains plagioclase phenocrysts, further suggesting mingling of the ignimbrite with mafic-intermediate magma. These filling of the pseudo-flames are parallel with the flow in the fiammes, further suggesting mingling of the ignimbrite with mafic-intermediate magma.

The presence of fine and microscopic fiamme and vermicular pseudo-fiamme in the ignimbrite levels, which in some cases are filled with quartzo-feldspathic minerals, probably provides other important evidence for magma mingling. In this case, light colored felsic clasts, which probably were originally pumice during eruption, represent formation from the rhyolitic magma (Figure 3.16). It seems that the vesicles inside the pumice were obliterated or modified due to diagenesis or pressure of the overlying rocks.

The longest dimension of the elongated vesicles, like that of the basic-intermediate inclusions in the ignimbrite, aligns with the direction of the ignimbrite flow. Commonly, field evidence for magma mingling are given by the presence of mafic-intermediate enclaves in the ignimbrite, hybrid breccias with felsic and mafic clasts, felsic pseudo-flames filled with intermediate lava, and heterogeneity in the ignimbrite texture, all present in the study area.

Bimodal basalt- and rhyolite-dominated distribution of volcanic rock is commonly formed as a result of rhyolite/granite eruptions in an area (Winter, 2001). So, other significant aspect of the Bijgerd-Kuh e Kharchin area, may be the bimodal nature of the Eocene volcanism, which is manifest in the eruption of four levels of mafic –intermediate (E^{ab} , E^a , E^{hy} , E^b) and three levels of felsic lava ($E^{ig1a,b}$, E^{ig2} , and E^{ig4}) (Figure 3.2b).

Petrography

Determination of modal mineralogy indicates that volcanic rocks in the study area are mostly micro-phenocryst-rich porphyritic mafic-intermediate volcanic and volcanoclastic rocks. The rock samples could be classified into the following groups: basalt (KM 30, 33, 35, 36, 38, 42, 44, 50), andesite (KM 50), trachyandesite (KM 37, 41), and dacite (KM 31, 32).

K-spar found occurs in dacite, and the only feldspar that occurs in andesite is plagioclase. However, the high-K andesite could be distinguished by the presence of sanidine (Gill, 1981). Therefore, the presence of sporadic K-feldspars in some rocks suggests that samples KM 31 and 32 are dacite and sample KM 37 and 41 are trachyandesite (see major element discussion in Chapter 4.3).

Geochemically, the rock samples KM 32 and 47 are classified as trachydacite and KM 43 and 45 are trachyandesite due to their high alkali content (see major element section). However, since these rocks are highly altered this classification, based on the major oxide geochemistry, may not be valid.

The data of the felsic volcanoclastic rock samples and those of samples KM 44, 45, 30, and 40 may not represent magmatic processes due to the high degree of alteration.

Generally, all samples are dominated by plagioclase, which occurs as anhedral, euhedral and altered grains.

Variations in the mineralogy reflect the silica content, as grains of quartz and alkali feldspar occur in only few samples. Alteration, twinning, and compositional zoning within plagioclases are clearly detected under microscope (Figures 3.24-3.25). Samples are altered in different degrees. Although some samples contain broken or rounded grains, others contain sharply euhedral crystals.

The distinct preferred orientation displayed by the plagioclase laths in the matrix of some samples suggests that the matrix was liquid and moving around the phenocrysts. The modified outlines of the phenocrysts, which are partly or completely replaced by opaque and other minerals, suggest that the rocks have undergone either late-stage or post-magmatic alteration (Cox, 1979).

The presence of sericite in plagioclase (Figures 3.25-3.27), and iddingsite in olivine formed probably due to saussuritization and opacitization, respectively, suggest hydrothermal reactions in an aqueous environment (Foster and Rubenach 2006; Vernon, 2004; Shelley, 1993). Therefore, it is most likely that volcanic rocks in the study area have experienced an oxidizing condition in an aqueous environment, which is consistent with the field observation discussed in section 4.1.

Microscopic fragments in the blobby and splintered andesitic lava (e.g., KM 43, 51, and 45) probably attesting to eruption and cooling under water, have margins that are hydrated and contain a variety of green minerals such as chlorite and epidote.

Calcite, as a secondary mineral, is commonly formed due to hydrothermal alteration following substitution (Ganeshram et al., 2003). So, the presence of calcite in the volcanoclastic samples may represent the hydrothermal phases related to the andesitic lava. Reaction with limestone (abundant within the volcano-stratigraphic sequence of the study area) during substitution could be the source of the carbonate.

The plagioclase, orthopyroxene, and clinopyroxene surround inclusions of common accessory minerals like apatite. Corroded and fairly resorbed cores of the plagioclase crystals, in the studied volcanic rocks (KM, 47 and 51), representing sieve texture (Figure 3.24), could suggest magma mixing (Shelley, 1993).

In addition to magma mixing, sieve texture may form through magmatic decompression (Pearce et al., 1987; Nelson, 1992; Shelley, 1993). A plagioclase crystal embedded in disequilibrium magma, during magma mixing, would get corroded or injected by the mixing magma. In this case, the melt is diffused into the crystal structure. New plagioclase crystals, with different compositions, grow as rim on the corroded core (Nelson, 1992; Shelley, 1993).

In other words, a sieve texture develops when the An% of the plagioclase in the disequilibrium magma is more than the plagioclase crystal. In this case, the corroded surface of the plagioclase crystal becomes irregular and riddled, and fills with magma, resulting in a calcium-rich plagioclase. Sodium-rich plagioclase dissolves in the acidic magma as basic and acidic magmas mix and becomes more calcic, producing a sieve texture. However, a plagioclase crystal normally grows to develop a more sodium-rich composition (Nelson, 1992; Shelley, 1993). Therefore, calcium-rich rims of the plagioclase phenocryst are normally indicative of a sieve texture (Shelley, 1993).

Magma decompression can also produce the sieve texture when volatiles escape due to the reduction of the confining pressure as magma ascends (Nelson, 1992; Shelley, 1993). In the case of decompression, there is no sequential and systematic variation in the composition of the zonings of the plagioclase crystals (Pearce et al., 1987; Nelson, 1992; Shelley, 1993). High percentages of anorthite, determined by microprobe analysis, are naturally rare.

However, An₉₀-An₁₀₀, similar to some of the studied samples (KM 38, 42), is found as phenocrysts in basic lava and crystal ejecta in subduction zone calcalkaline rocks. Cases of high anorthite content have also been reported in volcanic rocks of Monte Somma (pre-Vesuvius), Italy due the introduction of limestone blocks into magma (Angel et al., 1998), and in Miyakajima, Japan (Scasso et al., 1998) as glassy phenocrysts with basalt skins (Scasso et al., 1998). Although it is hard to have anorthite this high crystallizing from a terrestrial magma, it could suggest formation by multiple injections of magma or formation of an extraordinary magma. Given the field evidence, discussed in section 4.1 for magma mingling, and petrographic analyses, the sieve textures in the studied thin sections could probably form as a result of either magma mixing or magma decompression.

Temperature changes during magma mixing, and variation in water pressure through decompressional crystallization, produce the normal zoning which is followed by a reverse zoning or oscillatory zoning (Ustunisik and Kilinc 2007; Shelley, 1993).

In summary, the volcanic and volcanoclastic rocks of the Middle and Late Eocene are petrographically almost similar in each sequence. The rock samples are altered to varying degrees, higher in the oldest sequence compared to younger ones.

Variation in the silica content, due to the presence of veinlets of quartz, and presence of calcite and alkali feldspar grains that occur in only few samples reflect some variations in mineralogy. The differences among samples can be explained by their generation under different circumstances, such as the presence or absence of external water. It is also possible that they originated in different zones of the magma chamber or as result of multiple injections of magma.

Major Element Analysis

Geochemical classification of the rock samples based on their major element concentrations is commonly efficient if rocks are not altered. Analyses of the major elements (Figure 3.32) show that the igneous rocks of the study area have silica compositions that range from 47 wt% to 74 wt%; and the combined alkali ($\text{Na}_2\text{O} + \text{K}_2\text{O}$) that ranges from 2.3 wt% to 7.7 wt%. They also show a broad range in the loss on ignition (1.9-11.4 % LOI, Table 3.3) which typically indicate alteration.

The studied rock samples are divided into basalt, andesite/trachyandesite, and dacite/trachydacite fields based on their position on the common Total Alkali-Silica (TAS) diagram (Figure 3.31). However, this classification may not be valid due to the high level of alteration in these rocks.

Therefore, field rock names are preferred over those determined using the TAS diagram. The rock samples are classified into these three groups as follows: basalt (KM 30, 33, 35, 36, 38, 42, 44, 48, 49, 51), andesite (KM 50), trachyandesite (KM 45, 37, 43, 41), dacite (KM 31, 32, 39, 46), and trachydacite (KM 34, 47). Based on field observation, sample (KM 40) is defined as andesitic tuff, and (KM 39) is identified as breccias. Thin sections of the dacite samples contain quartz and alkali feldspar phenocrysts, consistent with the higher Si, Na, and K concentrations for these samples seen in the geochemical analysis.

The samples that fall within the basalt and andesite field of the TAS diagram do not contain these alkali feldspar phenocrysts. However, as mentioned before, based on the major element data combined with petrographic study, the majority of rock samples, mainly those with the ignimbritic composition, are altered to varying degrees.

Therefore, this classification may not be valid and provided with the ensure accuracy. As shown in Figure 3.32, the rocks are dominantly medium-K to high-K calc-alkaline volcanic rocks. High-K calc-alkaline rocks, such as these, are typically associated with subduction zones (Gill, 1981), although the exploration of the tectonic setting is out of the scope of this investigation. It is also possible that the distribution of the samples on the TAS diagram in the alkaline field is due to alteration. High scatter in the K_2O contents in ignimbritic rocks are possibly due to potassium metasomatism (hydrothermal alteration) (Kochhar, 1977) or post-magmatic processes.

Since the K_2O (8 wt%) obtained in the ignimbrites is greater than the average K_2O (~ 4.5 %), the high potassium content is not probably due to crustal contamination. Potassium could be added while sodium and calcium are removed from volcanic rocks through hydrothermal activities like groundwater leaching (Kochhar, 1977).

Therefore, the high potassium content and low sodium and calcium content in the felsic rocks (Figures 3.32- 3.34) can be explained by hydrothermal alteration. The variation diagrams (Figure 3.35) reveal some clues as to the geochemical characteristics and petrogenetic trends of the Kharchin-Bijgerd area.

The hyaloclastic rock samples with possible basaltic composition show a minor scatter, defining a cluster on the left side of the Harker diagrams. The ignimbritic rock samples, mostly of dacite-rhyolite and trachydacite composition, lie compositionally on the right side of the diagrams. The andesitic to trachyandesitic rock samples lie in the middle, between mafic and felsic rocks.

There are open spaces between the hyaloclastite, intermediate, and ignimbrite clusters suggesting that they do not make a continuum, probably because of either alteration or diverse sources.

The spatial heterogeneity in the composition of each sequence can again be explained by alteration. No temporal (i.e., stratigraphic) variation of the major oxides in the hyaloclastic rocks is observed in any sequence, except for the olivine andesite basalt E^{hy} unit in the third sequence which has a high MgO content (Figure 3.35).

Thin sections of the third sequence (KM 35, 36, and 51) contain olivine and pyroxene phenocrysts, consistent with the higher Fe and Mg concentrations for these samples seen in the geochemical analysis.

Trendlines for most of the major oxides plotted against SiO₂ concentration (Figure 3.34) show a negative correlation. The TiO₂, Fe₂O₃, MgO, CaO, MnO, Al₂O₃ in the hyaloclastite and ignimbritic rocks decrease in abundance with an increase in the SiO₂ content.

Since the concentration of TiO_2 decreases with decreasing temperature and increasing SiO_2 , as a result of the progressive breakdown of Ti-bearing phases (biotite and ilmenite) (Frost et.al., 1999), the decrease of TiO_2 with increasing SiO_2 in the plotted diagrams (Figure 3.34) may suggest fractional crystallization.

In each sequence, Fe_2O_3 , MgO , CaO , and Al_2O_3 decrease temporally and spatially with increasing SiO_2 . These features suggest that formation of hyaloclastites from the melt through fractional crystallization (Rodriguez et al, 2007; Blight et al, 2008).

Felsic rocks are commonly expected to have higher Si, Na, and K concentrations than mafic or intermediate rocks (Rollinsin, 1993; Winter, 2001).

Therefore, large ion lithophile elements (LILE) oxides such as Na_2O , K_2O correlate positively with increasing SiO_2 . However, some exceptions are observed in the Harker diagrams in this investigation.

The Na_2O vs. SiO_2 plot (Figure 3.34) displays an unusual trend. It first increases from mafic to the intermediate rocks and then decreases to the felsic rocks. This trend could be as a consequence of alteration. The low sodium content of these felsic rocks could be explained by cooling and devitrification of these rocks by hydrothermal fluids when sodium is removed from volcanic rocks through hydrothermal activities. Although the K_2O values show significant scatter in trachydacite and rhyolite due to high alteration, a positive correlation between K_2O and SiO_2 (Figure 3.34) is expected because K is an incompatible element, and K_2O usually varies linearly and positively with increasing SiO_2 (Gill, 1997). Note, in plots of the major oxides against MgO wt% (Figure 3.35) and Mg number (Figure 3.36), only the hyaloclastites and intermediate rock samples are considered.

In this investigation, disregarding alteration effects, the large variation in some major oxides values (e.g. MgO), can be explained by fractional crystallization. The MgO in the basic-intermediate samples ranges from 1.08 wt% (KM 46, E^v unit) to 5.2 wt% (KM 38, E^b unit). Mafic rocks are expected to have higher FeO* (total iron) and lower Al₂O₃ with decreasing MgO due to the crystallization of olivine and plagioclase through abundance of oxides crystal fractionation. Therefore, both FeO* and MgO concentrations link negatively with silica (Gill, 1997). The spatial scatter in the distribution of the major element oxides of the mafic rocks suggests that alteration created the chemical and compositional variation in the basic to intermediate units (Utsunomiya et al., 2004).

As shown in Figure 3.35 and 3.36, the major element patterns in the hyaloclastic to intermediate rock samples are compatible with crystal fractionation. For instance, segregation of a phenocrystic mineral (e.g. olivine in basalt) increases the FeO/MgO ratio in the rock; conversely, the removal of calcium plagioclase from the melt decreases Al₂O₃ and CaO concentrations. Besides the alteration effects, the large variation in the mafic rocks especially in the E^{hy} unit (Figure 3.34) is probably related to the breakdown of magnesium phases during partial melting or their removal during fractional crystallization (Rollinson, 1993; Winter, 2001).

As evolutionary indexes, silica, magnesium oxide, and the Mg number all display the same trend in the studied samples. Most of the mafic-intermediate rocks are compositionally evolved, with Mg# for the basalts ranging from 23-63.

Although there are some problems with the validity, accuracy, and adequacy of geochemical data interpretation of samples that have experienced alteration, the results of the major element analyses and petrographic study, coupled with field observations suggest that the rock samples have a complex petrogenetic history.

The significant scatter in the distribution of some major oxides such as K_2O and Na_2O , and the presence of a broad range in the LOI of the analyzed samples are probably due to a high degree of alteration that occurred either during eruption (e.g., under water) or later due to hydrothermal activity. It is considered less likely that the alteration is a recent phenomenon (e.g., weathering).

It seems that alteration occurred more intensely in older sequences (e.g. Middle Eocene, sequence 1 and 2) than the younger sequence 3 and 4. Therefore, trace elements should be more useful to identify the magmatic processes.

Trace Elements Analysis

The geochemical analyses, based on the rare earth and other trace element concentrations data, involved both comparing the spatial and temporal (stratigraphic) variation of the compositions of different samples taken in the Middle Eocene units and the four Late Eocene sequences.

The patterns of the REE distributions in the analyzed samples are assumed to reflect partial melting, crystal fractionation, and compositional variation of the source rock, as well as secondary alteration. As shown in Figure 3.38, except for sample KM 38, the REE patterns of all hyaloclastites display a negative Eu anomaly.

Although the LREE, MREE, and HREE may distribute differently under different geochemical processes, or presence of different mineral phases, adjacent elements in the REE series are predicted to behave similarly to one another, producing a smooth curve. Therefore, the obvious drop in the Eu concentration is an anomalous REE pattern.

Distinguishing characteristics of the europium (e.g. being divalent and trivalent) make it a more practical element for describing and comparing the rock samples. As stated before, in an igneous system, europium (Eu) has a valence of 2^+ instead of a 3^+ . Since Eu and its trivalent neighbors, samarium (Sm) and gadolinium (Gd), behave similarly, a minor variable pattern of abundances would suggest that Eu occurred mainly as a 3^+ cation, whereas a large negative anomaly of Eu concentrations (observed in this study), would suggest the presence of Eu in the 2^+ oxidation state. The magnitude of the europium anomaly is represented by the $\text{Eu}/\text{Eu}^* = \text{Eu}_N / (\text{Sm}_N * \text{Gd}_N)^{0.5}$ ratio, which gives the relationship between the measured normalized europium (Eu) and the expected normalized europium (Eu^*).

The REE predominantly occupy the structural position of Ca in minerals such as plagioclase, apatite, sphene (which is not still known), epidote, calcic garnet, and clinopyroxene.

In this case, Eu^{3+} changes to Eu^{2+} because of its similarity in size to Ca^{2+} . Substitution of Eu^{3+} or other trivalent REE for Ca^{2+} can, in the above mentioned minerals, be accompanied by equivalent substitution of Na^+ for Ca^{2+} , Si^{4+} for P^{5+} , or Al^{3+} for Si^{4+} in the REE-bearing rock forming minerals (Lepland et al., 2002).

Apatite, a phosphate mineral in the crust, distinctively and abundantly partitions the REE. The MREE are partitioned more than HREE and LREE in apatite (Hanson, 1980; Best and Christiansen, 2001; Prowatke and Klemme, 2004). The common substitution for Ca^{2+} in apatite is LREE^{3+} , Na^+ , Sr^{2+} , Ba^{2+} , Mg^{2+} , Eu^{2+} , Pb^{2+} , Mn^{2+} , Fe^{2+} , Fe^{3+} , Eu^{3+} , Y^{3+} (Ingrid, 1998).

Amphiboles (e.g., hornblende) have a tendency for partitioning the middle REE (Hanson, 1980), with distribution coefficients (K_d) greater than one (compatible) for gadolinium (Gd), and yttrium (Y) (Rollinson, 1993).

The distribution coefficient (K_d) for amphiboles and clinopyroxenes generally increases from light to heavy REE with a negative Eu anomaly in their trends (Rollinson, 1993).

The selective MREE substitution can provide a positive europium anomaly when calcium in plagioclase is accumulated (Hanson, 1980) (seen in the rock samples KM 30, 48, 43, and 44), or may contribute to a negative Eu anomaly (e.g., KM 31, 32, 46, 47, 34, 41, and 42) when calcium plagioclase is removed from the melt during crystal fractionation (Winter, 2001).

The accumulation and fractionation of plagioclase of the plagioclase phenocrysts, which respectively contributed to a positive and negative Eu anomaly, suggest essential conditions in the formation of these rocks. For instance, the accumulation of plagioclase phenocrysts in rocks samples KM 30 and 48 of the first Late Eocene sequence show similar positive anomalies, suggesting similar partitioning of Eu and analogous behavior that may be the result of a same source and conditions of formation. Moreover, it also could suggest that in these rocks, the Eu preferentially partitions into the plagioclase minerals over the melt compared to its neighbors (Sm^{3+} and Gd^{3+}).

The negative Eu anomaly in the REE patterns results by the substitution of Eu^{2+} for Ca^{+2} in plagioclase. Partitioning of Eu^{2+} into plagioclase, if followed by the subsequent removal of plagioclase crystals, which carry away the europium through fractional crystallization, would lead to a negative Eu anomaly.

The negative Eu anomaly typically occurs when Eu is present in the divalent (2^+) oxidation state, in which case plagioclase is removed through both fractional crystallization and partial melt fractionation (Rollinson, 1993). If Eu existed in its trivalent (3^+) form, a smooth and identical behavior (e.g. slight variation and predictable compatibility with increasing atomic weight) by the three trivalent REE neighbors, Sm, Eu, and Gd, would be expected.

The abrupt and distinct change in Eu concentration would therefore provide clues as to the composition of the fluid (or magma).

The valence of europium is an indication of the oxygen activity. Eu commonly occurs in the +2 valence state under low oxygen activity conditions compared to the +3 valence state which occurs under higher oxygen activity (Hanson, 1980).

In the low oxygen activity conditions, Eu^{+3} is reduced to Eu^{+2} . In this case, the effective ionic radius of Eu is increased, providing common substitution in Eu-bearing phases which are mainly plagioclase. Therefore, the negative anomaly of europium, which is seen in the REE patterns of ignimbrites and intermediate rock samples (Figures 3.38-3.44), suggests that Eu was abundantly present in the divalent oxidation state. The anomaly also suggests that the rock samples in this investigation have experienced a low oxygen activity condition such as that which prevails in the mantle, lower crust, and hydrothermal fluids of the upper crust.

The almost identical REE patterns for the Middle Eocene rock samples (Figures 3.38-3.44), show spatial homogeneity in this succession, suggesting origination of their parent magma from the same source which was melted and erupted in Middle Eocene. All Middle Eocene rock samples have negative Eu-anomalies due to Ca-plagioclase fractionation.

The REE pattern of sample KM 44 suggests accumulation of hornblende or clinopyroxene in this rock since it shows a higher concentration of the HREE in its pattern compared to that of samples KM 42 and 43. The hyaloclastites in the first (lowest) (samples KM 30, KM 48) and the fourth Late Eocene sequence (sample KM 38) (Figures 3.37-3.44) do not show a negative Eu anomaly in their REE pattern, probably indicating no plagioclase fractionation in the source magma.

Except for two samples (KM 30 and 48) in the first Late Eocene sequence, which are not plotted in Figure 3.38, similar REE patterns of hyaloclastic rock, taken from different stratigraphic levels, also reveal temporal homogeneity in both successions, suggesting eruption of a single magma at different times.

Except KM 30, 48, all hyaloclastites may have gone through plagioclase and/or clinopyroxene fractionation since as is suggested by their negative Eu-anomaly. Moreover, besides the almost identical and distinct parallel REE patterns with the Eu anomalies of the hyaloclastic rock samples of the study area, large variation in the incompatible element distributions among them (Figure 3.38), provides further evidence for fractional crystallization of plagioclase or clinopyroxene, and further evidence of their origination from the same source.

Despite the difference in the relative crystallization ages (indicated by the stratigraphic position), the two Upper Eocene ignimbrite sequences (KM 31, 32, 46, 47, and 34) have similar REE concentrations and distribution patterns (Figures 3.38-3.44), suggesting origination of their parent magma from the same source by fractional crystallization of plagioclase that erupted at two different times during Late Eocene.

In contrast, the REE patterns of ignimbrites samples (KM 37 and 41) taken from the third and fourth Late Eocene sequences (E^{ig3} and E^{ig4}) are dissimilar from the rest of Late Eocene sequences, which may indicate that they were not derived from similar sources (Figures 3.39-3.45). Sample KM 37 (third sequence) may have resulted from hornblende or clinopyroxene accumulation from a magma with a REE distribution like that of sample KM 41 (fourth sequence) (Figures 3.39-3.45).

The dissimilar REE patterns of different samples taken from the first sequence show spatial heterogeneity, suggesting formation from magmas originated from different sources (Figure 3.41).

The REE patterns for samples KM 30 and 48, with mafic composition, are almost identical. These two rock samples show higher concentrations of LREE than the other hyaloclastic rock samples that follow the same pattern of abundances (Figure 3.42).

This different behavior could be created as a result of varying geochemical evolutionary processes and involvement of specific mineral phases. These two rock samples are also dissimilar from the other mafic rock sample (KM 45), and felsic rock samples (KM 31, 32, 47, and 48) which reveal spatial heterogeneity in the first sequence, suggesting they were not derived from similar sources (Figures 3.38-3.44).

As shown in Figure 3.44, samples KM 30 and 48 may have resulted from calcium plagioclase accumulation while KM 45, 31, 32, 46, and 47 may represent calcium plagioclase or clinopyroxene fractionation.

In the second sequence, the identical REE patterns for samples KM 33 and 50 provide further evidence for a same source. Sample KM 50 could have formed as a result of plagioclase fractionation from parent magma with a REE pattern like that of KM 33. However, the REE pattern of KM 32 suggests that it cannot be related to a parent magma that formed KM 33 or 50 (Figures 3.42-3.45).

The identical REE patterns of three rock samples (KM 35, 36, and 51), taken from the third Upper Eocene sequence, suggest they were derived from similar sources during the Late Eocene (Figures 3.43-3.45). No variation in the compatible elements (HREE) likely indicates that these rocks formed through partial melting (Honsen, 1990).

The higher values of Gd_N (15.4) for both KM 35, 36, which compare to that of KM 51 ($Gd_N=12.5$), is probably a result of interference of either praseodymium oxide or lanthanum oxide with gadolinium.

The REE patterns of KM 37 is probably influenced by crystal fractionation as is revealed by the presence of the negative Eu-anomaly as well as the parallel shift of individual REE patterns to higher (i.e., enriched) values.

The REE pattern of sample KM 38 from the youngest (fourth) Late Eocene sequence is different (sub-parallel and slightly downshifted) from the other hyaloclastite units. This young sequence displays a generally smoother pattern in its chondrite-normalized REE element distribution with lower REE concentrations (Figures 3.37-3.44-3.45).

This fact points out that the younger basic source in the study area is actually more depleted than the older source. Moreover, since sample KM 38 contains quartz phenocrysts, visible in hand sample and thin section, the sub-parallel and downshifted pattern of this rock sample can be described by the dilution effect of quartz due to its very low REE content (Tripathi and Rajamani, 2007).

In the fourth sequence, sample KM 38, unit E^b and sample KM 41, E^{ig4} unit have the lowest REE concentrations compare to the older units. The low REE concentrations in these two samples of the youngest sequence show that they are not produced by differentiation of the same magma that produced the old units. However, as shown in figures 3.43-3.44, the dissimilar REE patterns of KM 38 and 41 may suggest that they may not be related to similar/one parent magma by fractional crystallization of plagioclase. The majority of the data from the trace elements reveals the compositional variation in each sequence among different types of rocks.

The scatter that exists between volcanic rocks could be suggestive of some evolution (e.g., through magmatic differentiation) of the magma.

Besides the alteration effects, the slight compositional variation in each sequence also may be due to the highly porphyritic nature of the rocks, and their spatial or compositional heterogeneity.

Due to the excellent resistance of Zr and Ti during hydrothermal alterations (Muchangos, 2006), they can be used in correlating the hyaloclastic units and in tracing their sources (Figure 3.45). There should be a positive correlation in the TiO_2 vs. Zr diagram (Figure 3.45). The negative correlation suggests that the ignimbrites are not differentiated from the hyaloclastic rocks (i.e., they have different sources).

The compositional variation can be created by either partial melting or fractional crystallization (Wilson, 1989).

Through partial melting, the incompatible elements (e.g., La, Rb, Zr,) are rapidly and dramatically mobilized into the early melts while the compatible elements (e.g., Ni, Cr, Yb, and Y) remain in the solid minerals. Therefore, the incompatible elements concentrations are significantly increased in the melt during partial melting.

Consequently, a depletion of compatible elements in the melt would be expected during the process of fractional crystallization, which takes away elements from the melt. However, the change in the compatible element concentrations through fractional crystallization is less than the depletion of incompatible elements during partial melting (Hanson, 1980). Therefore, the chemical trends of identical series of rocks may be explained by either fractional crystallization or partial melting.

The phenocrysts in most volcanic rocks are typically formed at high levels, under low pressure and near-surface conditions through the fractional crystallization process. Therefore, achieving high temperatures required for partial melting, along with the near-surface conditions, would be difficult (Cox et al., 1979). The occurrence of any compositional evolution is probably a result of fractional crystallization. However, the extensive variation in incompatible element abundances, along with the near-surface conditions, suggests that partial melting was the final fractionation process.

During eruption or intrusive injection, as minerals are crystallized and removed from the magma chamber, the composition of the remaining magma would be changed. Nickel (Ni) is considered to be a compatible element, commonly substituting for Fe^{2+} and Mg^{2+} in olivine (Jordan, 2007), and the compatible element, chromium Cr, substitutes for Fe^{+3} in clinopyroxene or Al^{+3} in hornblende during fractional crystallization. Therefore, the low concentrations of Ni, ~17-55 ppm, and Cr, ~ 10-30 ppm in the studied mafic rock samples compared to the average values in mafic rocks of 250-300 ppm for Ni and 500-600 ppm for Cr (Best, 2001), would likely indicate olivine and pyroxene fractionation.

Rubidium (Rb) and barium (Ba) both may partition for potassium (K) in micas and potassium feldspars. A range of 1.6-165 ppm for Rb and 317-839 ppm for Ba is obtained for the studied rock samples. In basaltic and andesitic magmas, barium is slightly more compatible than Rb in micas and feldspars, and may also occur in amphiboles (Hanson, 1980).

Strontium (Sr) is present in high concentrations (~610 ppm) in the plagioclase-rich rock samples. In this study, the felsic rocks are rich in elements that are incompatible with ferromagnesian minerals, such as Th (11-13 ppm), Zr (204-296 ppm), and the LREE like La (33-41 ppm), Ce (68-72 ppm).

In contrast, elements compatible with feldspar, such as Sr (122-148 ppm), Eu (0.67-1.27 ppm), Ti (0.17-0.3 ppm), and P (0.03-0.05 ppm) are comparatively depleted. Unlike the felsic rocks, the studied mafic rocks show a smooth pattern with relative depletions of the HFSE, such as Nb (3-8 ppm), Zr (44.1-64.6 ppm), Ti (0.42- 0.75 ppm), and enrichment of the LILE, like Ba (316-775 ppm), and Sr (215-610 ppm). However, due to the high degree of alteration, the concentrations of the mobile trace elements (e.g., Rb, Sr, Cr, Ni, etc) may not be magmatic. Therefore, to ensure accuracy only some immobile trace elements are selected for plotting and discussion.

The compositional variations of the incompatible elements (Rb, Zr, La, etc) and compatible elements (Sr, Yb, Ce, and Ni) are reliable evidence for fractional crystallization (Hanson, 1980).

The compatible elements reduce in concentration with increasing SiO₂, while the concentration of the incompatible elements increases. As shown in Figure 3.46, Zr shows a positive correlation with increasing SiO₂. Moreover, since Zr, La, Nb, and Ce are identically incompatible, they may be expected to behave alike (Figure 3.47). Moreover, Ce, Nd, and Sm are respectively plotted versus La in Figure 3.50, showing a positive correlation from mafic to felsic rock.

As shown in Figures 3.47-3.49, some variations in trace element concentrations were observed from the mafic group to the felsic group in each of the Late Eocene sequences, suggesting different origins for the mafic and felsic groups or differentiation of a single magma. The felsic magmatism could be either the latest product of fractionation or additional assimilation of former mafic magma with crustal components (Depaolo, 1981; Dungan and Davidson, 2004).

Geochemically, like the REE, Th and U similarity behave and dominate in some minerals such as apatite, zircon and monazite. Therefore, the evaluation of geochemical behavior of U and Th can be useful to discriminate between fractionation processes and heterogeneity in composition of the source region (Stern and Hanson, 1991; Taylor and McLennan, 1985).

As shown in Figure 3.49, the open space between the Hyaloclastites, and felsic rocks suggest that they do not make a continuum, probably because of diverse sources. For comparison, the averages of upper and lower continental crust have been added in Figures 3.48-3.50. The majority of the hyaloclastic rocks would be comparable with those of the average of lower crust while the felsic rocks mostly show an upper crustal origin. Some rock samples follow the pattern between the lower and upper crust (Figures 3.48-3.50). This fact could suggest magma mixing or mingling (Wilson, 1989) by the intrusion of a hot basaltic magma into the continental lithosphere.

The process may have led to the contamination of the magma by crustal rocks through mingling, subsequent fractionation to form the felsic magma, and explosion. In Figure 3.51 La has been plotted against Yb for the Middle and all Late Eocene sequences. Some variations can be seen in concentrations of the incompatible La, while little variation is seen in the compatible Yb concentrations plotted in Figure 3.51. This fact may suggest that both partial melting and fractional crystallization dominate the processes that led to the compositional variations.

CHAPTER 5

CONCLUSIONS

Composition and texture of the Middle and Late Eocene volcanic, volcanoclastic, and volcanic-sedimentary rocks in the Bijgerd-Kuh e Kharchin area, northwest of Saveh, provide significant geochemical and geological clues for the magmatic evolution of the Uromieh-Dokhtar volcanic-plutonic zone of Iran.

The Middle Eocene volcanic rocks have an intermediate composition and include green tuff and tuffaceous sandstone with intercalated sandstone, sandy tuff, and shale. The shale has lenses of Nummulite-bearing limestone with a Middle Eocene detrital age.

The Late Eocene samples represent bimodal volcanism, characterized by four alternating phases (sequences) of eruption of hyaloclastite lava and ignimbrite. Based on field work the Middle Eocene volcanic and volcanic-sedimentary rocks were divided into two units (E^{gt} , E^v). The Late Eocene volcanic rocks are divided into the following four sequences, each including several units: sequence 1 (E^{ab} , E^{mbr1} , E^{ig1a} , E^{ig1b} , E^{mbr2}), sequence 2 (E^a , E^{st1} , E^{st2} , E^{ig2}), sequence 3 (E^{hy} , E^{ig3}), and sequence 4 (E^b , E^{mbr3} , and E^{ig4}).

The occurrence of hyaloclastic tuff and breccia at the base of the E^v unit, the existence of hydrated volcanic fragments in it, and the presence of a sequence of shallow and intermediate-depth marine sedimentary microfossils in the E^{gt} unit, all suggest that the Middle Eocene units were erupted in a marine basin.

The nature of the magmatic differentiation (e.g., crystal fractionation, partial melting) and other processes (e.g., magma mingling) responsible for the evolution of the Eocene volcanic succession, are supported by a variety of field evidence, trace element geochemical data, and petrographic and microprobe observations. These data reveal the complexity of the magmatic system that evolved the Middle and Late Eocene volcanic rocks of the Bijgerd-Kuh e Kharchin area through multiple eruptions from one or more sources.

The summary of the main evidence for the type of magmatic processes, and source of the magma, in which the volcanic-volcaniclastic sequence were formed are listed below.

The REE patterns of the studied rock samples show spatial and temporal (i.e., stratigraphic) homogeneity (with the exception of the E^{ab} unit) in the sampled hyaloclastites of the Bijgerd-Kuh e Kharchin volcanic succession, suggesting origination from a single source at different times. However, the REE patterns show spatial homogeneity and temporal heterogeneity between hyaloclastite and ignimbrite in each Late Eocene sequence, suggesting origination of magma from varying sources that erupted at different times. A pronounced compositional gap between the hyaloclastites and ignimbrites and the lack of discernable trendline between them, on the trace diagrams, suggest the existence of at least two sources of magma for the volcanic-volcaniclastic rocks.

The proposed multi-source hypothesis is supported by the significant variation in the trace element concentrations between hyaloclastites and ignimbrites and their dissimilar REE patterns.

Moreover, the fact that the volume of the ignimbrites far exceeds that of the hyaloclastites probably argues against the idea that the latter is the product of differentiation of the magma that formed the former.

Since the trace element distributions of the hyaloclastites and ignimbrites are compatible with those evolved through fractional crystallization of the lower and upper continental crust, respectively, the source for the ignimbrite lavas could be the upper crust of the Euroasian (Iranian) continental plate while the hyaloclastic rock samples might be originated in the lower continental crust.

The distinct negative Eu anomaly in the REE patterns of the hyaloclastite and ignimbrite samples, in addition to reflecting plagioclase fractionation, suggests that these rocks formed under a low oxygen activity condition such as that which may exist in the mantle or lower or upper crust.

Evidence for magma mingling/mixing in the Eocene volcanic rocks include: the presence of mafic-intermediate enclaves in the ignimbrites and felsic pseudo-flames filled with intermediate lava in at least three levels (E^{ig1} , E^{ig2} , and E^{ig4}), hybrid breccias with felsic and mafic clasts (E^{mb1} , E^{mb2} , and E^{mb3}), variation of the composition of the ignimbrite from rhyolite (E^{ig1}) to trachy-dacite (E^{ig1} and E^{ig2}) to trachy-andesite (E^{ig3} and E^{ig4}), heterogeneity in the ignimbrite matrix, and the sieve texture in the plagioclase.

The REE patterns and other trace element distributions suggest that both crystal fractionation and partial melting dominated the magmatic processes.

The significant scatter in the distribution of some major oxides such as K_2O and Na_2O , the presence of a broad range in the LOI of the analyzed samples, and the deformed shapes of the phenocryst, which partly or completely are replaced by opaque minerals, suggest that the rocks have undergone either late-stage or post-magmatic alteration and/or crustal contamination through magmatic or hydrothermal processes.

The presence of sericite, formed due to saussuritization in plagioclase, and iddingsite, formed through opacitization in amphiboles, and veinlets of iron oxide (e.g., hematite) and calcite in hyaloclastites, suggests that the hydrothermal reactions occurred in a subaqueous environment.

REFERENCES

- Aghanabati, SA, 2006, *Geology of Iran*, Geological Survey of Iran, 582p.
- Amidi, S.M., Emami, M.H., and Michel, R., 1984, Alkaline character of Eocene volcanism in the middle part of central Iran and its geodynamic situation: *Geologische Rundschau*, v. 73, p. 917-932.
- Amidi, S.M. and Michel, R., 1985, Cenozoic magmatism of the Surk area (central Iran) stratigraphy, petrography, geochemistry and their geodynamic implications: *Geologie Alpine*, v.61, p. 1-16.
- Angel, R. J., Hazen, R. M., McCormic, T. C., 1988, Comparative Compressibility of End Member Feldspars," *Phys. Chem. Minerals* **15**, 313–318.
- Awwiller, D.N., 1994, Geochronology and mass transfer in Gulf Coast mudrocks (southcentral Texas, U.S.A.): Rb-Sr, Sm-Nd, and REE systematics. *Chemical Geology*, 116: 61-84.
- Babaie, H.A., Ghazi, A.M., Babaei, A., La Tour, T.E., and Hassanipak, A.A., 2001, Geochemistry of arc volcanic rocks of the Zagros Crush Zone, Neyriz, Iran. *J. Asian Earth Sci.*, 19, 61-76.
- Baker, J., Waight, T., and Ulfbeck, D., 2002, Rapid and highly reproducible analysis of rare earth elements by multiple collector inductively coupled plasma mass spectrometry. *Geochimica et Cosmochimica Acta*, 66: 3635-3646.
- Berberian, M., and King, G.C.P., 1981, Towards a paleogeography and tectonic evolution of Iran: *Canadian Journal of Earth Sciences*, v. 18, 210-265p.
- Bierlein, F.P., 1995. Rare-earth element geochemistry of elastic and chemical metasedimentary rocks associated with hydrothermal sulphide mineralisation in the Olary Block, South Australia. *Chemical Geology*, 122: 77-98.
- Best, M.G., and Christiansen, E.H., 2001, *Igneous Petrology*: Oxford, England, Blackwell science, inc., 457p.
- Bolourchi, S., 1979., "On Finite-Element Analysis of General Shell Structures," PhD Dissertation, Massachusetts Institute of Technology, Cambridge.
- Bowen, H. J. M., 1976, *Trace Elements in Biochemistry*. Academic Press, 2nd edition, 384p.
- Calliat, C., Dehlavi, Rasool, Marcel, Jantin, B., 1978, *Geologie de la Region de Saveh (Iran). Contribution a l'etude de volcanism et de plutonism Tertiares de la zone de 1 etude d'Iran Central. These 3emm cycles*, Grenoble, 253p.
- Browne, B.L., Eichelberger, J.C., Patino, L.C., Vogel, T.A., Uto, K., Hoshizumi, H., Dehn, J., 2006, The generation of porphyritic and equigranular enclaves during magma recharge events at Unzen volcano. *Japan. J. Petrol.* 47, 301–328.
- Cox, K.G., 1979, *The interpretation of igneous rocks*: United Kingdom, George Allen & Unwin: London, United Kingdom.

- Deer, W.A., Howie, R.A., and Zussman, J., 1992, An introduction to the rock-forming minerals: New York, Wiley, 696p.
- DePaolo, D.J. 1981, Trace element and isotopic effects of combined wallrock assimilation and fractional crystallization, *Earth and Planetary Science Letters* 53, p.189–202.
- Dewey, J.F., Pitman, W.C., III, Kyan, W.B.F., and Bonnin, J., 1973, Plate tectonics and the evolution of the Alpine system: *Geological Society of America Bulletin*, v. 84, p.3137-3180.
- Dungan, M.A., Davidson, J.P., 2004, Partial assimilative recycling of the mafic plutonic roots of arc volcanoes: an example from the Chilean Andes, *Geology* 32 (9) p.773–776.
- Eftekharnjad, J., 1981. Tectonic division of Iran with respect to sedimentary basins. *Journal of Iranian Petroleum Society*, 82, 19–28, (in Persian).
- Emami, M.H., 1991, Explanatory text of the Qom quadrangle map, Geological Quadrangle No. E6, Geological Survey of Iran.
- Fairbridge R. W., 1978, Breccia, sedimentary. In *The Encyclopedia of Sedimentology* (eds. R. W. and Fairbridge J. Bourgeois),. 84–86p. Dowden, Hutchinson & Ross.
- Feldman V.I., 2001, OPACITIZATION OR SHOCK-THERMAL, Geological Moscow, 119899, Russia; *Lunar and Planetary Science XXXII*, 1164.pdf.
- Foster DA, Rubenach MJ, 2006, Isograd pattern and regional low-pressure, high-temperature metamorphism of pelitic, mafic and calc-silicate rocks along an east-west section through the Mt Isa Inlier. *Aust J Earth Sci* 53:167–186.
- Forster, H., Fesefeldt, K., and Kursten, M., 1972, Magmatic and orogenic evolution of the central Iranian volcanic belt: 24th International Geologic Congress, p.198-210.
- Ganeshram, R.S., François, R., Commeau, J., Brown-Leger, S.L., 2003, An experimental investigation of barite formation in seawater, *Geochimica et Cosmochimica Acta*, 67, 2599-2605.
- Geostandards, 1984, USGS Reference Samples: *Geostandards Newsletter Special Issue*, v. VIII.
- Gill, J.B., 1981, *Orogenic andesites and plate tectonics*: Berlin ; New York, Springer- Verlag, 390 p.
- Gill, R., 1997, *Modern Analytical Geochemistry: an introduction to quantitative chemical analysis techniques for earth, environmental and materials scientists*: Essex, Addison Wesley Longman limited, 329 p.
- Hanson, G.N., 1976, *Rare earth element analysis by isotope dilution*: National Bureau of Standards Special Publication, 937p.
- , 1980, Rare earth elements in petrogenetic studies of igneous systems: *Annual Review of Earth and Planetary Sciences*, v. 8, p. 371.

- , 1989, An approach to trace element modeling using a simple igneous system as an example: *Reviews in Mineralogy*, v. 21, p. 79.
- Hanson, G.N., and Langmuir, C.H., 1978, Modeling of major elements in mantle-melt systems using trace element approaches: *Geochimica et Cosmochimica Acta*, v. 42, p. 725.
- Hildyard, S., C., J. W. Cole, S. D. Weaver, 2000, Tikorangi Ignimbrite: a 0.89 Ma mixed andesite-rhyolite ignimbrite, Matahara Basin, Taupo Volcanic Zone, New Zealand. - *New Zealand J. of Geol. and Geophys.*, 43,p. 95-107.
- Hyndman, R.D., Wang, K., and Yamano, M., 1995, Thermal constraints on the seismogenic portion of the southwestern Japan subduction thrust. *J. Geophys. Res.*, 100:15373-15392.
- Ingamells, C.O., 1970, Lithium metaborate flux in silicate analysis. *Analytica Chimica Acta*, 52: 323-334.
- Jansen, W., Slaughter, M., 1982, Elemental mapping of minerals by electron microprobe. *American Mineralogist* 67 (5-6): 521–533.
http://www.minsocam.org/ammin/AM67/AM67_521.pdf.
- Jones, A.P., Wall, F., and Williams, C.T., 1996, Rare earth minerals: Chemistry, Origin and Ore Deposits, Mineralogical Society Series, v.7 London; New York, 327p.
- Jordan, J., 2007, The Arnes central volcano, Northwestern Iceland. 2007 Keck Geology Consortium Project Announcement, 1-4.
- Kazmin, V.G., Sbertshikov, I.M., Ricou, L-E., Zonenshain, L.P., Boulin, J., and Knipper, A.L., 1986, Volcanic belts as markers of the Mesozoic-Cenozoic active margin of Eurasia: *Tectonophysics*, v. 123, p. 123-152.
- Kerrick, D. M., Eminhizer, L.B. and Villaume, J.F., 1973, The role of carbon film thickness in electron microprobe analysis, *Am. Min.*, 58, 920-925.
- Khalatbari, M., 2000, Geological map of Nobaran, Geological Survey of Iran.
- Kidder, D., L., Krishnaswamy, R. and Mapes, R.H., 2003, Elemental mobility in phosphatic shales during concretion growth and implications for provenance analysis. *Chemical Geology*, 198: 335-353.
- Kochhar, N. 1977, Post-emplacement alkali modifications in rapidly cooled acid volcanic rocks. Department of Geology, Panjab University Chandigarh- I 600 14, India *American Mineralogist*, V.62, p. 33-335.
- Lauri, L.S., Karinen, T., Rasanen, J., 2003, The earliest Paleoproterozoic supracrustal rocks in Koillismaa, northern Finland – their petrographic and geochemical characteristics and lithostratigraphy. *Bull. Geol. Soc. Finland* 75(1–2), 29–50.
- Le Bas, M.J., Le Maitre, R.W., and Streckeisen, R., 1986, A chemical classification of volcanic rocks based on the total alkali-silica diagram: *Journal of Petrology*, v. 27, p.745-750.

- Le Maitre, R. W., 2002, *Igneous Rocks: A Classification and Glossary of Terms, Recommendations of the International Union of Geological Sciences, Subcommission of the Systematics of Igneous Rocks.*, Cambridge, University Press, ISBN 0-521-66215-X.
- Meckel, T.A., ten Brink, U.S., and Williams, S.J., 2007, Sediment compaction rates and subsidence in deltaic plains: numerical constraints and stratigraphic influences: *Basin Research*, v. 19, p. 19-31.
- Masuda, A., Nakamura, N. and Tanaka, T., 1973, Fine structures of mutually normalized rare-earth patterns of chondrites. *Geochimica et Cosmochimica Acta*, 43: 1131-1140.
- McQuarrie, N., Stock, J.M., Verdel, C., and Wernicke, B.P., 2003, Cenozoic evolution of Neotethys and implications for the causes of plate motions: *Geophysical Research Letters*, v. 30, 2036.
- Meffer, S., D, Ireen, N. G., C., Rawford, A.J, Amenetsky, V, 2004, Mafic volcanic rocks on King Island, Tasmania: evidence for 579 Ma break-up in east Gondwana. *Precambrian Research* 135, 177-191.
- Muchangos, A.C., 2006, The mobility of rare-earth and other elements in the process of alteration of rhyolitic rocks to bentonite (Lebombo volcanic mountainous chain, Mozambique), *J. Geochem. Expl.* 88, p. 300–303.
- Nelson, S.A., Gonzalez-Caver, E., Kyser, T.K., 1995, Constraints on the origin of alkaline and calc-alkaline magmas from the Tuxtla Volcanic Field, Veracruz, Mexico: *Contributions to Mineralogy and Petrology*, 122 (1-2), 191-211.
- Nelson S.T., Montana. A, 1992, Sieve-textured plagioclase in volcanic rocks produced by rapid decompression. *Am Mineral* 77, p.1242–1249.
- Rankama, K. and Sahama, T.G., 1950, *Geochemistry*. University of Chicago Press, Chicago, IL, p.911.
- Reed, S.J.B., 1996. *Electron Microprobe Analysis and Scanning Electron Microscopy in Geology*. Cambridge University Press, 201p.
- Rollinson, H.R., 1993, *Using geochemical data; evaluation, presentation, interpretation*: United Kingdom, Longman Scientific & Technical: Harlow, United Kingdom.
- Philpotts, A.R., 1989, *Petrography of Igneous and Metamorphic Rocks*: Englewood Cliffs, New Jersey, Prentice .Hall, 107p.
- Prowatke, S., Klemme, S., 2004, Trace element partitioning between apatite and silicate melts, *Geochim. Cosmochim.* p.4513–4527.
- Sakuyama. M, 2007, Petrographic evidence of magma mixing in Shirouma-Oike volcano, Japan, *Bulletin of Volcanology*, v.41-4.

- Sepehr, M., Cosgrove, J.W., Moieni, M., 2006, The impact of cover rock rheology on the style of folding in the Zagros fold-thrust belt. *Tectonophysics*, 427, p.265-28.
- Sengor, A.M.C., Cin, A., Rowley, D.B., and Nie, S-Y., 1993, Space-time patterns of magmatism along the Tethysides: a preliminary study: *The Journal of Geology*, v. 101, 51-84p.
- Setudenia, A. 1972, Mesozoic sequence in southwest Iran and adjacent areas.
- Scasso RA, Corbella H, Tiberi P, 1994, Sedimentological analysis of the tephra from the 12–15 August 1991 eruption of Hudson volcano. *Bull Volcanol* 56:121–132.
- Shahabpour, J., 2007, Island-arc affinity of the central Iranian volcanic belt: *Journal of Asian Earth Sciences*, v. 30, 652-665 p.
- Stern, R.A. and Hanson, G.N., 1991. Archean High-Mg Granodiorite: A Derivative of Light Rare Earth Element-enriched Monzodiorite of Mantle Origin. *Journal of Petrology*, 32: 201-238.
- Stocklin, J., 1968, Structural history and tectonics of Iran: a review: *American Association of Petroleum Geologists Bulletin*, v. 52, 1229-1258p.
- Stocklin, J., and Setudehnia, A., 1977, Stratigraphic lexicon of Iran, Geological Survey of Iran, Report no. 18, second edition, 376 p.
- Shelley, D., 1993, *Igneous and Metamorphic Rocks Under the Microscope*: London, Chapman and Hall, 445 p.
- Tripathi, J.K., Rajamani, V., 2003, Geochemistry of Delhi quartzites: implications for the provenance and source area weathering, *J. Geol. Soc. Ind.* 62, p.215–226.
- Tomascak, P.B., Krogstad, E.J. and Walker, R.J., 1996. Nature of the crust in Maine, USA; evidence from the Sebago Batholith. *Contributions to Mineralogy and Petrology*, 125: 45-59.
- Ustunisik, G. K., Kilinc, A., 2007, A New Explanation For Oscillatory Zoning In Plagioclase Phenocrysts, American Geophysical Union, abstract #V33C-1521.
- Utsunomiya, S., Jensen, K., Keeler, G., Ewing, R., 2004, Direct identification of trace chemical species in fine and ultraparticle fine in the Detroit urban atmosphere. *Environmental Science & Technology*, 38, 2289–2297.
- Vaziri, M, 1998, Study On Petrography and Petrology Of Volcanic Rock, Tehran University, Iran, 408 p.
- Verdel, C., Wernicke, B.P., Ramezani, J., Hassanzadeh, J., Renne, P.R., and Spell, T.L., 2007, Geology and thermochronology of Tertiary Cordilleran-style metamorphic core complexes in the Saghand region of central Iran: *Geological Society of America Bulletin*, v. 119, p. 961-977.

- Vernon, R.H., 2004, A practical guide to rock microstructure Cambridge, U.K., New York, Cambridge University Press, 594p.
- Walsh, J.N., Gill, R., and Thirwall, M.F., 1997, Dissolution procedures for geological and environmental samples, Modern analytical geochemistry an introduction to quantitative chemical analysis for earth, environmental and materials scientists:Essex, Addison Wesley Longman limited, 329p.
- Whalen, J.B., Currie, K.L., Chappell, B.W., 1987, A-type granites, geochemic characteristics, discrimination and petrogenesis. Contribution to Mineralogy and Petrology, 95, 407-419.
- Wensink, H. and Varekamp, J.C., 1980, Paleomagnetism of basalts from Alborz: Iran part of Asia in the Cretaceous. Tectonophysics, 68, 113-129.
- Winter, J. D, 2001, An Introduction To Igneous And Metamorphic Petrology, Prentic-Hall Inc, New Jersey, 697p.
- White, W.M., 2007, Geochemistry: Cornell University.
- 1:250,000 Geological Map of Saveh (1981). Geological Survey of Iran.
- 1:100,000 Geological Map of Nobaran (2001). Geological Survey of Iran. National Geosciences Database of Iran.
<http://www.ngdir.ir/GeoportalInfo/PSubjectInfoDetail.asp?PID=18&index=1>
- National Geosciences Database of Iran
<http://www.ngdir.ir/GeoportalInfo/PSubjectInfoDetail.asp?PID=18&index=1>